A Heterojunction Bipolar Transistor with Stepwise Alloy-Graded Base: Analysis, Design, Fabrication, and Characterization

by

Konstantinos Konistis

Diploma, National Technical University of Athens (1996)
S.M., Massachusetts Institute of Technology (1998)

Submitted to the Department of Electrical Engineering and Computer Science in partial fulfillment of the requirements for the degree of

Doctor of Philosophy

at the

MASSACHUSETTS INSTITUTE OF TECHNOLOGY

August 2004

© Massachusetts Institute of Technology 2004. All rights reserved.

Author ....
Department of Electrical Engineering and Computer Science
August 24, 2004

Certified by ....
Qing Hu
Professor
Thesis Supervisor

Accepted by ....
Arthur C. Smith
Chairman, Department Committee on Graduate Students

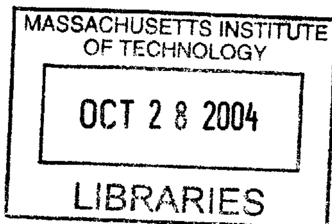

BARKER

A Heterojunction Bipolar Transistor with Stepwise Alloy-Graded Base: Analysis, Design, Fabrication, and Characterization

by

Konstantinos Konistis

Submitted to the Department of Electrical Engineering and Computer Science
on August 24, 2004, in partial fulfillment of the
requirements for the degree of
Doctor of Philosophy

Abstract

This thesis explores the potential benefits of a GaAs-based heterojunction bipolar transistor (HBT) with stepwise alloy-graded base. The step height is slightly greater than the longitidinal optical (LO) phonon energy $\hbar\omega_{LO}$ in order to facilitate LO-phonon-enhanced forward diffusion of minority carriers in the base. The intuitive theoretical approach of carrier transport in the base, as proposed by other workers for this type of alloy-grading, did not incorporate in detail the various mechanisms of transport. In this work, we solved the Botzmann transport equation (BTE) in one dimension across the base for arbitrary frequencies. Impurity and LO phonon scattering were considered as the dominant scattering mechanisms. The intrinsic and extrinsic elements were combined and a small-signal equivalent circuit was proposed for the evaluation of the high-frequency performance of the device. The unique feature of this HBT is that the base transport factor undergoes a moderate magnitude attenuation and phase delay. By choosing a suitable collector delay, a band-limited negative output resistance can emerge in the microwave/millimeter-wave regime. The main benefit of the device is its inherent property as a transit-time high-frequency oscillator. Using our device simulator, we selected the material parameters for epitaxial growth (MBE) of the device wafer and we investigated various device layouts. We implemented the complete microfabrication of 2 μm $\times$ 15 μm, self-aligned, emitter-up HBTs with micro-airbridges for device isolation purposes. We performed DC measurements of various devices and they provided us with feedback for modifications in the MBE design and growth conditions of the device wafer. We finally fabricated HBTs with favorable DC features but the device self-heating turned out to be crucial for the longevity of the base micro-airbridges. The short lifetime of the base micro-airbridges was prohibitive for the realization of high frequency measurements. This work serves as the foundation for the implementation of robust HBT transit-time oscillators with the incorporation of slight modifications in the fabrication process.

Thesis Supervisor: Qing Hu
Title: Professor

0.1 Acknowledgments

I would like to acknowledge my research advisor Prof. Qing Hu for his constant guidance and the financial support he provided to me throughout the years I spent at MIT. I would like to thank the members of my research group, Ben Williams, Sushil Kumar, Hans Callebaut, and Stephen Kohen, for their constructive feedback whenever I found myself in deadlock during my research. I am indebted to Henry Choy for all the epitaxial work needed for this project. I am very appreciative of his tireless efforts and his stimulating discussions. I would like to thank Wojciech Giziewicz for his useful tips during the DC measurements of my devices. The numerous suggestions and the constant encouragement from Prof. Sheila Prasad are deeply appreciated. I would like to express my gratitude to the MTL members, students and staff, who taught me the tricks of microfabrication. I am especially grateful to Dave Terry and Kurt Broderick for their enthusiasm, their patience with my questions and concerns, and their assistance beyond the boundaries of their professional duties.

During the years I spent at MIT, I was fortunate to be surrounded by people who reminded me of the non-academic aspects of life. I would like to thank Christoforos and Leonidas for being good friends without expecting anything in return. This work would not have been completed without the inspiration and support of Taina. She stood by me during difficult times and she shared with me times of joy and excitement. Her generosity and optimism gave me strength and reminded me of the genuine priorities in life. My parents and my brother back home have been a constant source of unconditional support and encouragement throughout my life. Without them, I wouldn't be able to start this long journey and explore new challenges in life. I am truly grateful to them.

Contents

0.1 Acknowledgments 3

1 Introduction **16**

1.1 Thesis Motivation 16

1.2 Thesis Overview 21

2 Theoretical Analysis **22**

2.1 HBT vs BJT 22

2.2 HBT in the Diffusive Transport Approximation 24

2.3 Formulation of BTE 26

2.4 Solution of BTE 29

2.5 Simulation Results of the Intrinsic Operation 34

2.6 Intrinsic HBT circuit 41

2.7 Extrinsic HBT circuit 42

2.8 Small Signal Parameter Formulation 45

2.9 Microwave/Millimeter Wave Figures of Merit 47

2.10 HBT Microwave/Millimeter Wave Performance 49

3 HBT Design and Fabrication **53**

3.1 MBE Design 53

3.2 Ohmic Contacts 58

3.3 Device Layout 59

3.4 Transmission Line Design 63

3.5 On-Wafer Calibration Structures 65

3.6 CPW Losses and Effective Dielectric Permittivity 68

3.7 Device Isolation 69

3.8 Fabrication Steps 73

3.8.1 Device Wafer Cleaving 75

3.8.2 Emitter Contact 77

3.8.3 Emitter Wet Etching, Si_3N_4 sidewall deposition, and Base Contact 78
3.8.4 Base and Collector Etching, Subcollector Contact, and Device Isolation . . . 82

4 Experimental Results **87**
4.1 Measurements of the Specific Contact Resistance 87
4.2 Device Profile and Failure Modes 92
4.3 DC Measurements 93
4.3.1 DC Characteristics of SM6000 97
4.3.2 DC Characteristics of LG7000, LG9000, and LG7000U 101
4.3.3 DC Characteristics of SM7000 and SM9000 105

5 Conlusions **110**

A Process Flow **113**

List of Figures

1-1 Schematic band diagram of an HBT with stepwise alloy-graded base. 18

1-2 Schematic band diagram of (a) a HBT with stepwise alloy-graded base and base thickness X_{B1}=$N \times X_{step1}$, (b) a HBT with uniform base and base thickness X_{B2}=X_{B1}, and (c) a HBT with uniform base and base thickness X_{B3}=X_{step1}. The base transit time, the magnitude attenuation and phase delay of the total base transport factor attain small values for (c), large values for (b), and intermediate values for (a). These features of (a) are favorable for the implementation of a transit-time oscillator. . . . 19

2-1 Band diagram of a HBT and a BJT. The dotted line corresponds to the valence band of the BJT in the emitter. The emitter-base junction of the HBT is smoothly alloy-graded. The electron and hole flow is $\vec{F_e}$ and $\vec{F_h}$ respectively. Electrons and holes recombine mainly in the space charge region and in the bulk of the base. The electrons that have not recombined are swept across the collector. The HBT exhibits limited hole injection from the base into the emitter due to the presence of ΔE_g in the valence band. 23

2-2 Band diagram of two base steps (a) before thermal equilibrium, and (b) after thermal equilibrium. Holes are transported from the base step of larger bandgap to the base step of smaller bandgap. The bandgap difference appears in the conduction band after a few Debye lengths from the base step edge. 27

2-3 Conduction band of the base structure and energy grid for the solution of the BTE. The energy level E_0 in the first base step, where $0 \leq E_0 \leq \hbar\omega_{LO}$, defines a unique energy grid throughout the base with energy separation $\hbar\omega_{LO}$. The BTE can be solved independently for this energy grid. 32

2-4 Solution scheme for the BTE in the base structure. The blue/red color indicates forward/backward recursion. During the forward/backward recursion, the values of $f_\nu^{(-)}/f_\nu^{(+)}$ at the endpoinds are known from the previous backward/forward recursion, and the values of $f_\nu^{(+)}/ f_\nu^{(-)}$ at the endpoints are being updated. In the first recursion, the guess $f_\nu^{(-)}=0$ at the endpoints is used. Convergence is achieved when the current converges at some monitor points. 33

2-5 (a) Polar graph of α_T for $N\times X_{step}$=1000 Å, l_{imp}=300 Å, and Δ=1.2 $\hbar\omega_{LO}$ (marker every 100 GHz, frequency range 0-1 THz). As the number of steps increases (N=1, 2, 5), $|\alpha_T|$ increases and $|\angle\alpha_T|$ decreases resulting in a higher frequency performance. (b) Polar graph of the base step transport factor for N=5, X_{step}=500 Å, l_{imp}=300 Å, and Δ=1.2 $\hbar\omega_{LO}$ (marker every 40 GHz, frequency range 0-300 GHz). The base step transport factors are grouped in three families of curves, the first $\{\alpha_1\}$, the middle $\{\alpha_2, \alpha_3, \alpha_4\}$, and the last $\{\alpha_5\}$. 36

2-6 Polar graph of α_T for (a) N=5, l_{imp}=300 Å, Δ=1.2 $\hbar\omega_{LO}$, and variable X_{step}, (b) N=5, X_{step}=400 Å, Δ=1.2 $\hbar\omega_{LO}$, and variable l_{imp}, and (c) N=5, X_{step}=500 Å, l_{imp}=300 Å, and variable Δ. In (a)-(c), the frequency range is 0-300 GHz and every marker corresponds to 40 GHz increment. 37

2-7 Magnitude of the normalized current density distribution $|\rho_J|$ for N=5, X_{step}=500 Å, l_{imp}=300 Å, and Δ=1.2 $\hbar\omega_{LO}$ (Frequency=100 GHz). In (a), (b), and (c), the 1st, 2nd, and 3rd base step is considered respectively. The distribution has a Maxwellian form in the first step. LO phonon scattering effects are clearly shown in the $|\rho_J| - E_k$ profile. The carriers are hotter for base steps closer to the collector side. 39

2-8 (a) Normalized minority carrier concentration n/n_e and (b) normalized forward velocity v^+/v_{th} and backward velocity v^-/v_{th} across the base for N=5, X_{step}=500 Å, l_{imp}=300 Å, and Δ=1.2 $\hbar\omega_{LO}$ (static case). The profiles of n/n_e, v^+/v_{th}, and v^-/v_{th} are nearly periodic in the middle steps. In (a), the effective diffusivity becomes larger near the collector side. In (b), v^+/v_{th} increases near the collector as the minority carriers become hotter. 40

2-9 (a) Schematic of an emitter-up HBT configuration, and (b) the equivalent circuit including intrinsic and extrinsic elements. The dashed lines in (a) and (b) indicate the intrinsic part of the device. The length of the device not shown in (a), is L_E. . . 43

2-10 Circuit evolution of the HBT for the calculation of small signal parameters. The common-base configurations (a) and (b) develop into more complex common-emitter configurations (c) and (d) with the addition of the extrinsic elements C_{jCx}, R_{Ex}, R_{Bx}, and R_{Cx}. 46

2-11 Unilateral power gain U (blue curves) and common emitter forward gain h_{21}^e (red curves) for a HBT with $N \times X_{step}$=1000 Å, X_C=4000 Å, device parameters of Table 2.2, and variable number of base steps (N=1, 2, 5). The introduction of base steps results in larger $|\alpha_T|$, improving both U and h_{21}^e. 50

2-12 (a) Unilateral power gain U (blue curves), common emitter forward gain h_{21}^e (red curves), and (b) output resistance for X_{step}=600 Å, X_C=6000 Å, device parameters of Table 2.2, and variable number of base steps (N=1, 2, 5). The inset in (b) is a magnification of the output resistance for the frequency range 50-120 GHz. As the number of base steps increases, peaks of resonance appear for the unilateral power gain. These shift to lower frequencies for increasing N and $U < 0$, $r_{22}^e < 0$ between the first two peaks. The maximum value of $|r_{22}^e|$ when $r_{22}^e < 0$ increases for increasing N. The larger base transport delay causes a shift of f_T to lower frequencies. 51

2-13 (a) Unilateral power gain U (blue curves), common emitter forward gain h_{21}^e (red curves), and (b) output resistance for N=5, X_{step}=600 Å, device parameters of Table 2.2, and variable collector thickness (X_{C1}=3000 Å, X_{C2}=6000 Å, X_{C3}=9000 Å). The inset in (b) is a magnification of the output resistance for the frequency range 40-120 GHz. As the collector thickness increases, the peaks of unilateral power gain resonance shift to lower frequencies, and f_T decreases due to the larger collector delay. The maximum value of $|r_{22}^e|$ when $r_{22}^e < 0$ increases and shifts to lower frequencies for increasing X_C. 52

3-1 Conduction band edge vs distance from the E-B junction for a family of V_{BE} values. The emitter is $Al_{0.35}Ga_{0.65}As$, the base is GaAs and the thickness of the linear alloy-grading layer is 200 Å. The base doping level is N_B=2×10^{19} cm^{-3}. The emitter doping level is N_E=1 × 10^{17} cm^{-3} in (a), and N_E=5 × 10^{17} cm^{-3} in (b). The superposition of the linear alloy-grading potential and the electrostatic potential creates a barrier for the transport of electrons in (a), and a slight peak in (b). 55

3-2 Illustration of the charge concentration ρ and the magnitude of the electric field $|E|$ in the collector for different values of the collector current density J_C and constant value of V_{CB}. The base, collector, and subcollector regions are designated by B, C, and SC, respectively. In (a), the collector is partially depleted and J_C is low. As J_C increases, the net positive charge in the collector decreases and the space-charge region in the collector increases. In (b), the collector is fully depleted and $J_C < qN_C v_{sat}$. In (c), ρ=0 in the collector and $|E|$ is constant. In (d), $\rho < 0$ in the collector and $|E|$ is low towards the base. In (e), high values of J_C result in vanishing $|E|$ at the B-C junction and base pushout occurs. 56

3-3 Schematic of emitter-up HBT configurations with a (a) B-E-C mesa, and (b) C-B-E-B-C mesa. The dashed rectangle in (a) and (b) indicate the intrinsic part of the device. The emitter-base masks of (a) and (b) are shown in (c) and (d), respectively. The emitter-base masks are designed for self-aligned HBTs. The S_{BE} separation between the emitter and the base is due to wet etching. 60

3-4 Detail of the device layout illustrating the various dimensions of importance. The coplanar waveguide connected to the HBT is not shown. 61

3-5 Cross section of a coplanar waveguide illustrating the various dimensions of importance. The direction of wave propagation is perpendicular to the illustrated cross section. 63

3-6 Top view of the coplanar waveguide and the HBT in a common-emitter configuration. The dashed rectangle includes the transition area between the coplanar waveguide and the HBT, and the various details are shown magnified. The ratio a/b is kept constant along most of the coplanar waveguide for a uniform Z_0. 64

3-7 Representation of the network analyzer systematic errors as a pair of two-port devices, A and B, at the input and output of the device under test. The TRL calibration resolves the scattering parameters of A and B and estimates the reflection coefficient of the Reflect standard and the propagation constant of the Line standard. 66

3-8 On-wafer coplanar waveguide structures for the TRL calibration: (a) open, (b) through, (c) short, and (d) line calibration standard. The length L_1 is chosen according to the frequency region of interest. Multiple line standards can be used for a broader frequency range. The TRL calibration brings the calibration planes at the beginning of the transition region. The open structure (e) is used for the de-embedding of the transition region. 67

3-9 Smith charts showing the measured S-parameters of the (a) OPEN, (b) SHORT, and (c) THROUGH on-wafer calibration standards for the frequency range 6-50 GHz. . . 69

3-10 Measured values of the CPW loss and the relative effective permittivity for the frequency range 10-40 GHz. The loss is higher than expected due to the presence of the doped layers under the signal line and the ground plane of the CPW. The relative effective permittivity is slightly lower than expected due to the non-zero height between the metal layer and the exposed semi-insulating substrate. 70

3-11 Cross sections of the HBT showing the different device isolation methods: (a) electrodes over the edge of the device mesa covered by a dielectric film, (b) electroplated electrodes contacting the device via openings of a dielectric layer, (c) planar electrodes for an active device defined by deep ion imlantation, and (d) micro-airbridges formed by deep wet etching. For (a)-(d), an emitter-up configuration is considered, the right electrode is for the emitter, the left electrode is for the base, and the substrate is semi-insulating. 71

3-12 Different micro-airbridge designs illustrating the device electrodes (yellow) and the photoresist (grey) prior to wet etching: a) the emitter and base micro-airbridges are parallel to [0 1 1], and the emitter is connected to the ground from only one side, b) the emitter and base micro-airbridges are parallel to [0 1 1] with no separation, and the emitter is connected to the ground from both sides, c) the emitter and base micro-airbridges are perpendicular to each other, the emitter micro-airbridge is parallel to [0 1 1], and the emitter is connected to the ground from both sides, d) the emitter and base micro-airbridges are parallel to [0 1 1] with a non-zero separation, and the emitter is connected to the ground from both sides. 72

3-13 SEM pictures of 2 μm× 8 μm test micro-airbridges. In (a) and (b), the solution 30 ml H_3PO_4 : 10 ml H_2O_2 : 500 ml H_2O was used. In (c) and (d), the solution 10 ml NH_4OH : 4 ml H_2O_2 : 500 ml H_2O was used. The micro-airbridge is parallel to [0 1 $\bar{1}$] in (a) and (c), and parallel to [0 1 1] in (b) and (d). The etched depth is about 2 μm. Device isolation can be achieved in (a) and (b) if the etched depth is much larger than 2 μm and the (c) choice does not appear suitable. Device isolation can be easily achieved in (d). 73

3-14 Steps of the HBT fabrication: (a) emitter metal deposition, (b)photoresist application on the emitter metal for the reduction of the galvanic effect, and wet etching, (c) ECR-CVD deposition of Si_3N_4 and directive RIE etching of Si_3N_4 for sidewall passivation, (d) photoresist application on the emitter metal for the reduction of the galvanic effect, and wet etching until the base is exposed, (e) base metal deposition, and RIE etching of the base and collector, (f) photoresist application on most of the device piece, and wet etching of the area where the subcollector metal will be deposited, (g) subcollector metal deposition, (h) photoresist application to define the active device area and reduce the galvanic effect, and deep wet etching. After the removal of the photoresist, the emitter and base micro-airbridges are revealed as shown in the dotted circles of (i), and the HBT fabrication is complete. The cross-sections A and B are utilized in Fig. 3-15 and Fig. 3-16. 74

3-15 Device profile during the HBT fabrication process (cross-section A of Fig. 3-14): (a) emitter metal evaporation, (b) isotropic and anisotropic wet etching for the formation of the emitter mesa, (c) sidewall deposition of Si_3N_4, (d) shallow wet etching for the removal of the damaged surface due to the RIE process, (e) base metal evaporation, (f) dry etching until the subcollector is exposed, (g) shallow wet etching for the removal of the damaged surface due to the RIE process, and (h) subcollector metal evaporation. The last step of the device isolation (after step (h)) does not affect the device profile of this cross-section. 75

3-16 Profile of the emitter and base micro-airbridges during the HBT fabrication process (cross-section B of Fig. 3-14): (a) emitter metal evaporation, (b) isotropic and anisotropic wet etching for the formation of the emitter mesa, (c) sidewall deposition of Si_3N_4, (d) shallow wet etching for the removal of the damaged surface due to the RIE process, (e) base metal evaporation, (f) dry etching until the subcollector is exposed, (g) device isolation by deep wet etching and formation of micro-airbridges. The shallow wet etching for the removal of the damaged surface due to BCl_3 etching and the subcollector metal evaporation (between step (f) and step (g)) do not affect the profile of the emitter and base micro-airbridges of this cross section. 76

3-17 Emitter contact detachment and formation of an emitter bow during the emitter wet etching. This is the result of the galvanic effect caused by large metallic surfaces in the wet etchant. 78

3-18 SEM pictures showing the different GaAs slopes after a wet etching process in a 10 ml NH_4OH : 4 ml H_2O_2 : 500 ml H_2O solution. In (a), the metal stripe is the $[0\ 1\ \bar{1}]$ direction and the slope is outward. In (b), the metal stripe is in the [0 1 1] direction and the slope is inward. This is the direction of the emitter contact, emitter micro-airbridge, base contact, and base micro-airbridge because it facilitates the separation of the base contact and the emitter mesa, and the device isolation. 80

3-19 SEM pictures of the emitter after the first wet etching of the emitter cap and the emitter. The emitter area is shown in (a) and (b), prior and after the Si_3N_4 sidewall deposition respectively. The wet etching process consists of a first non-selective etchant for the emitter cap removal and a second anisotropic etchant. The Si_3N_4 sidewall deposition takes place by an isotropic Si_3N_4 deposition and a directive RIE etching of the Si_3N_4 layer. 81

3-20 Etching profiles of a (a) GaAs layer and an (b) $Al_xGa_{1-x}As$ layer using the $CH_4/H_2/He$ recipe with a metal surface as a mask. Prolonged etching causes degradation of the metal surface. The Al etch products appear as spikes on the etched surface. 83

3-21 Almost vertical etching profiles of the intrinsic part (under the emiter contact) and the extrinsic part (under the base contact) of the HBT using the BCl_3/He recipe. . 84

3-22 SEM pictures of the emitter and base micro-airbridges. From one side of the HBT, (a) the emitter micro-airbridge is in parallel to the base micro-airbridge, and from the other side, (b) there is only the emitter micro-airbridge. The undercut from the deep wet-etching process is more pronounced along the micro-airbridges due to the galvanic effect. 84

3-23 SEM picture of the complete HBT device. The emitter and base micro-airbridges are revealed afer the final step of deep wet etching. 85

4-1 Cross section of a structure used for transmission line measurements. The length of every ohmic contact pad, not shown in the figure, is L. The separation distances of N ohmic contact pads are S_1, S_2,...,S_{N-1} and $S_1 < S_2 < ... < S_{N-1}$. 88

4-2 (a) Transmission line measurements of the emitter cap ohmic contacts (100 μm $\times$ 100 μm). The mesa includes the emitter cap and the emitter layers. The exposed surface away from the mesa is within the base layer. The evaporated metal layers are Ti(500 Å)/Pt(300 Å)/Au(2200 Å). The ohmic contact is non-alloyed. (b) Transmission line measurements of the subcollector ohmic contacts (100 μm $\times$ 100 μm). The mesa includes the subcollector layer. The exposed surface away from the mesa is within the semi-insulating GaAs wafer. The evaporated metal layers are Ni(50 Å)/Au (100 Å)/Ge(500 Å)/Au(900 Å)/Ni(300 Å)/Au(1200 Å). The ohmic contact is alloyed. For both (a) and (b), the measurements were taken for TLM structures of the same device piece. The measurement points with the same color represent a particular TLM structure. 89

4-3 Transmission line measurements of the base ohmic contacts (100 μm $\times$ 100 μm). The mesa includes the base and the collector layers. The exposed surface away from the mesa is within the subcollector layer. The thickness of the base layer that has not been etched is approximately 2300 Å for (a) and (c), and 1800 Å for (b). The evaporated metal layers in (a) and (b) are Pt(65 Å)/Ti(300 Å)/Pt(300 Å)/Au(900 Å) (non-alloyed ohmic contact), and in (c), Pt(80 Å)/Zn(500 Å)/Au(1000 Å) (alloyed ohmic contact). In (a), N_B=5 $\times$ 10^{19} cm^{-3}, whereas in (b) and (c), N_B=2 $\times$ 10^{19} cm^{-3}. For (a), (b), and (c), the measurements were taken for TLM structures of the same device piece. The measurement points with the same color represent a particular TLM structure. 91

4-4 Various device profiles of the self-aligned HBTs at the end of the fabrication process. The dashed lines are the interfaces of the emitter cap, the emitter, the base, and the subcollector. The metal, the semiconductor, and the sidewall passivation are respresented by the yellow, grey, and red areas, respectively. The ideal HBT device is illustrated in (a). In (b), BCl_3 etched away part of the exposed base and the intrinsic base cannot be contacted. In (c), the base metal created an electric short between the emitter and base contact. In (d), the RIE process of the Si_3N_4 layer etched away part of the sidewall passivation and the base metal contacts both the emitter and the base layer. 92
4-5 (a) Schematic illustrating a cross-section of the HBT and the various components constituting the flow of holes F_p in the base. The area between the dashed lines is the emitter-base space charge region. $F_{p,cont}$, $F_{p,surf}$, $F_{p,bulk}$, and $F_{p,scr}$ represent the recombination on the base contact, on the exposed base, in the bulk of the base, and in the emmitter-base space charge region, respectively. $F_{p,inj}$ represents the injected flow of holes from the base to the emitter. (b) Band diagram of the device along with the components of the electron and hole flow. The carrier flow components associated with the recombination in the extrinsic part of the device (base contact and exposed base) are not shown. 95
4-6 Measured DC characteristics of SM6000. In (a), I_C and I_B are plotted vs V_{BE} for a given V_{CB}. The dash-dotted lines originate from I_C and I_B curve fitting using suitable ideality factors. The inset illustrates I_C, I_B, and β vs V_{BE} in linear scale. In (b), I_C is plotted vs V_{CE} for a family of I_B values. In (c), β is plotted vs V_{BE} for a family of V_{CB} values. 98
4-7 Measured DC characteristics of LG7000. In (a), I_C and I_B are plotted vs V_{BE} for a given V_{CB}. The dash-dotted lines originate from I_C and I_B curve fitting using suitable ideality factors. The inset illustrates I_C, I_B, and β vs V_{BE} in linear scale. In (b), I_C is plotted vs V_{CE} for a family of I_B values. In (c), β is plotted vs V_{BE} for a family of V_{CB} values. 100
4-8 Measured DC characteristics of LG9000. In (a), I_C and I_B are plotted vs V_{BE} for a given V_{CB}. The dash-dotted lines originate from I_C and I_B curve fitting using suitable ideality factors. The inset illustrates I_C, I_B, and β vs V_{BE} in linear scale. In (b), I_C is plotted vs V_{CE} for a family of I_B values. In (c), β is plotted vs V_{BE} for a family of V_{CB} values. 102

4-9 Measured DC characteristics of LG7000U. In (a), I_C and I_B are plotted vs V_{BE} for a given V_{CB}. The dash-dotted lines originate from I_C and I_B curve fitting using suitable ideality factors. The inset illustrates I_C, I_B, and β vs V_{BE} in linear scale. In (b), I_C is plotted vs V_{CE} for a family of I_B values. In (c), β is plotted vs V_{BE} for a family of V_{CB} values. 104

4-10 SEM pictures of the HBT focusing on the emitter and base micro-airbridges. In (a), no DC bias had been applied at the device terminals and the micro-airbridges remain intact. In (b), DC bias had been applied at the device terminals. The elevated temperature of the base micro-airbridge caused metal deformation and eventually, the base micro-airbridge broke. 106

4-11 Measured DC characteristics of SM7000. In (a), I_C and I_B are plotted vs V_{BE} for a given V_{CB}. The dash-dotted lines originate from I_C and I_B curve fitting using suitable ideality factors. The inset illustrates I_C, I_B, and β vs V_{BE} in linear scale. In (b), I_C is plotted vs V_{CE} for a family of I_B values. 108

4-12 Measured DC characteristics of SM9000. In (a), I_C and I_B are plotted vs V_{BE} for a given V_{CB}. The dash-dotted lines originate from I_C and I_B curve fitting using suitable ideality factors. The inset illustrates I_C, I_B, and β vs V_{BE} in linear scale. In (b), I_C is plotted vs V_{CE} for a family of I_B values. 109

5-1 Profile of a HBT that allows the evaporation of a thick base ohmic contact. This is expected to increase the tolerance against self-heating without increasing the risk of an electric short between the emitter and the base. The emitter mesa is formed by dry etching and a Si_3N_4 layer is deposited on the mesa sidewalls. 111

List of Tables

2.1 Comparison of base transport factor for isotropic and anisotropic model. The structure has N=2, X_{step}=500 Å, l_{imp}=200 Å, Δ =1.2 $\hbar\omega_{LO}$. 35

2.2 Parameters used for the HBT evaluation 49

3.1 Design sheet for the MBE growth of the device. The device consists of the emitter cap, the emitter, the spacer, the base, the collector, and the subcollector. The collector thickness varies depending on the frequency range of interest for transit-time oscillations. 54

4.1 Differences in the layout and MBE design of the HBT devices under test. 94

Chapter 1

Introduction

1.1 Thesis Motivation

The research towards high-bandwidth heterojunction bipolar transistors (HBTs) has been motivated by a number of applications. Optical fiber communications, analog-to-digital and digital-to-analog converters, direct digital synthesizers, monolithic millimeter-wave integrated circuits and millimeter-wave sources rely heavily on the advances of HBTs [1]. The high-frequency designers exploit the potential of HBTs as essential components in digital, analog, and mixed-signal circuits.

Research labs have implemented high tansmission rate optical fiber communication networks ($\geq$ 40 Gb/s) [2, 3, 4]. These networks include digital circuits (multiplexers, demultiplexers, clock and data extraction circuits) and analog circuits (modulator drivers, low-noise preamplifiers, high-gain preamplifiers). They benefit significantly from high-bandwidth HBTs that function as switches and amplifiers. Analog-to-digital converters that trade off high sampling speed for higher resolution in amplitude have been realized with Δ-Σ modulators utilizing HBTs [5, 6]. They are key components for broad-band direct sampling receivers where the implemented oversampling techniques require bandwidths $10^2 : 1 - 10^4 : 1$ larger than the signal frequencies [1]. HBTs find applications in the development of direct digital frequency synthesizers. They offer high frequency resolution and fast frequency hopping capabilities in radar, elecronic warfare, and communication systems [7, 8].

The available bandwidth of RF/microwave communications is being heavily used. The demand for continuously higher transmission rates leads inevitably to the exploitation of the millimeter-wave regime (30-300 GHz). The atmospheric attenuation of millimeter waves is low in the bands 60-80 GHz, 120-160 GHz, and 220-300 GHz. Thus, monolithic millimeter-wave integrated circuits operating in these bands are attractive for earth-based millimeter-wave communications. The limitations posed by the absorption lines in the atmosphere are lifted in space-based millimeter-wave imaging arrays and communication systems. Furtermore, next-generation lightwave systems will operate at

data rates of 80-100 Gb/s or higher. They require high-speed digital circuits with clock sources in the millimeter-wave range. For all of the aforementioned applications, millimeter-wave local oscillators and amplification stages are essential components and HBTs are attractive candidates.

Both two-terminal and three-terminal devices have been used as millimeter-wave oscillators. The most prominent two-terminal sources are the IMPATT diodes, the TUNNET diodes, the Gunn-effect devices, and the resonant tunneling diodes (RTD). The IMPATT diodes exhibit excellent frequency performance and high power levels but the generated noise is high since they utilize the mechanism of impact ionization. The TUNNET diodes are characterized by low noise and intermediate frequency and power generation capability since they employ the mechanism of tunneling. GUNN effect devices are medium power devices with high frequency performance and low noise levels whereas RTDs generate low power level in the millimeter and submillimeter wave region. Two-terminal oscillators are usually fabricated and packaged seperately. Bonding wires or ribbons are utilized leading to high circuit losses and parasitics. On the conrary, three-terminal millimeter-wave oscillators can be monolithically integrated with other transmitter/receiver circuits. Furthermore, injection-locked oscillators are facilitated by three-terminal devices since there are separate ports for the input and output signal and circulators are not needed. The most notable three-terminal oscillators are based on high electron mobility transistors (HEMT) and HBTs. HEMT oscillators exhibit excellent frequency and power performance [9]. However, they demonstrate intermediate phase noise. The phase noise is associated with the $1/f$ noise. The source of this type of noise has been attributed to the heterointerface traps between the channel and the buffer [10]. The horizontal flow of carriers facilitates further this noise mechanism. On the other hand, HBT oscillators are characterized by lower $1/f$ noise. This type of noise is related to the extrinsic base region. Fluctuations in the occupancy of surface traps result in fluctuations of the surface recombination velocity [11]. Good passivation can significantly reduce the $1/f$ noise. In addition, HBT sources offer competitive frequency and power performance [12, 13, 14, 15, 16]. Both HEMT and HBT oscillators show negative resistance as a result of a feedback circuit that connects two terminals.

HBTs have been established as the technology of choice for amplifiers in handsets. Some advantages that HBTs offer compared to HEMTs for these applications are the power linearity and the battery power savings. Power linearity refers to the non-linear character of a device that is responsible for the generation of high harmonics. More specifically, if the input signal of a device is $v_i = v_1 \cos(\omega_1 t) + v_2 \cos(\omega_2 t)$, where $\omega_1 \approx \omega_2$, then the non-linearity of the device can produce signals with angular frequencies $2\omega_1 - \omega_2$ and $2\omega_2 - \omega_1$. Unfortunately, these signals are close in frequency with the desired output signals and they cannot be easily filtered out. HBTs offer exceptional power linearity despite the exponential form of the generated currents. This has been attributed to a cancellation of distortion components generated in the resistive and capacitive components of the HBT [17, 18]. HBTs have a very low leakage current in the off-state. On the other hand, HEMTs

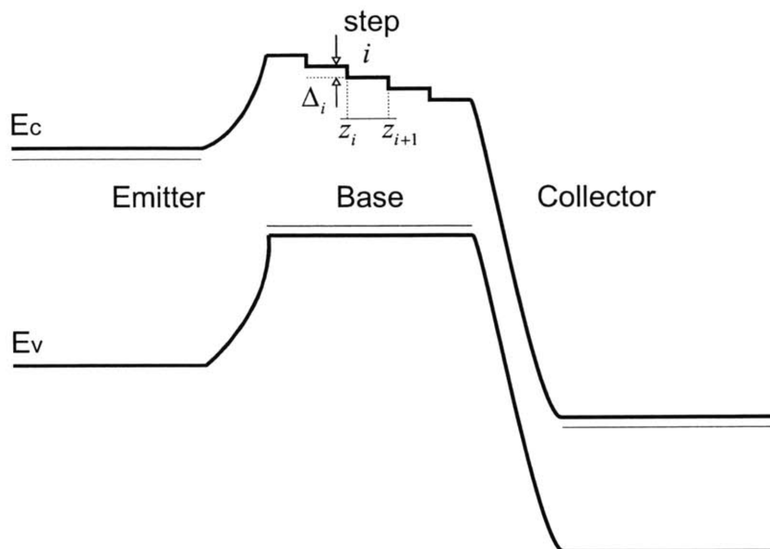

Figure 1-1: Schematic band diagram of an HBT with stepwise alloy-graded base.

have an appreciable leakage current and require a negative voltage supply to reduce this current. Enhancement-mode HEMTs (E-HEMTs) are competing HBTs since they are characterized by very low leakage currents and they do not require a negative supply. The turn-on voltage of the HBTs is determined by the material bandgap. On the contrary, the turn-on voltage of HEMTs is affected significantly by the epilayer thickness variation. In power applications, HBTs compete well with HEMTs since they offer higher breakdown voltage and exponential rather than power-law transfer characteristics [19].

The design of a high-bandwidth HBT focuses on both the extrinsic and the intrinsic part of the device. The extrinsic parasitic capacitances and the extrinsic resistances can deteriorate significantly the intrinsic limits of the device. Proton implantation [20], lateral etched undercut [21], and substrate transfer process [1] have been proven successful in reducing the base-collector parasitic capacitance. Advances in ohmic contacts and selective regrowth techniques contribute in lowering the base contact resistance. The base and collector structures affect drastically the transit time of carriers and determine the intrinsic device performance. Elaborate doping profiles in the collector can taylor the electric field in the depleted collector for low transit time and moderate collector capacitance [22, 23]. A short base favors the unit current gain frequency f_T due to the fast quasi-ballistic transport but worsens the unit power gain frequency f_{max} as a result of the elevated transverse base resistance. Band gap engineering resolves this problem by introducing a linearly alloy-graded base of moderate thickness fabricated in a molecular beam epitaxy (MBE) process. Both f_T and f_{max} are enhanced as the built-in field assists the carrier transport and the base transverse resistance is relatively low.

This work explores a novel base structure proposed by Luryi and Grinberg in [24]. As shown in

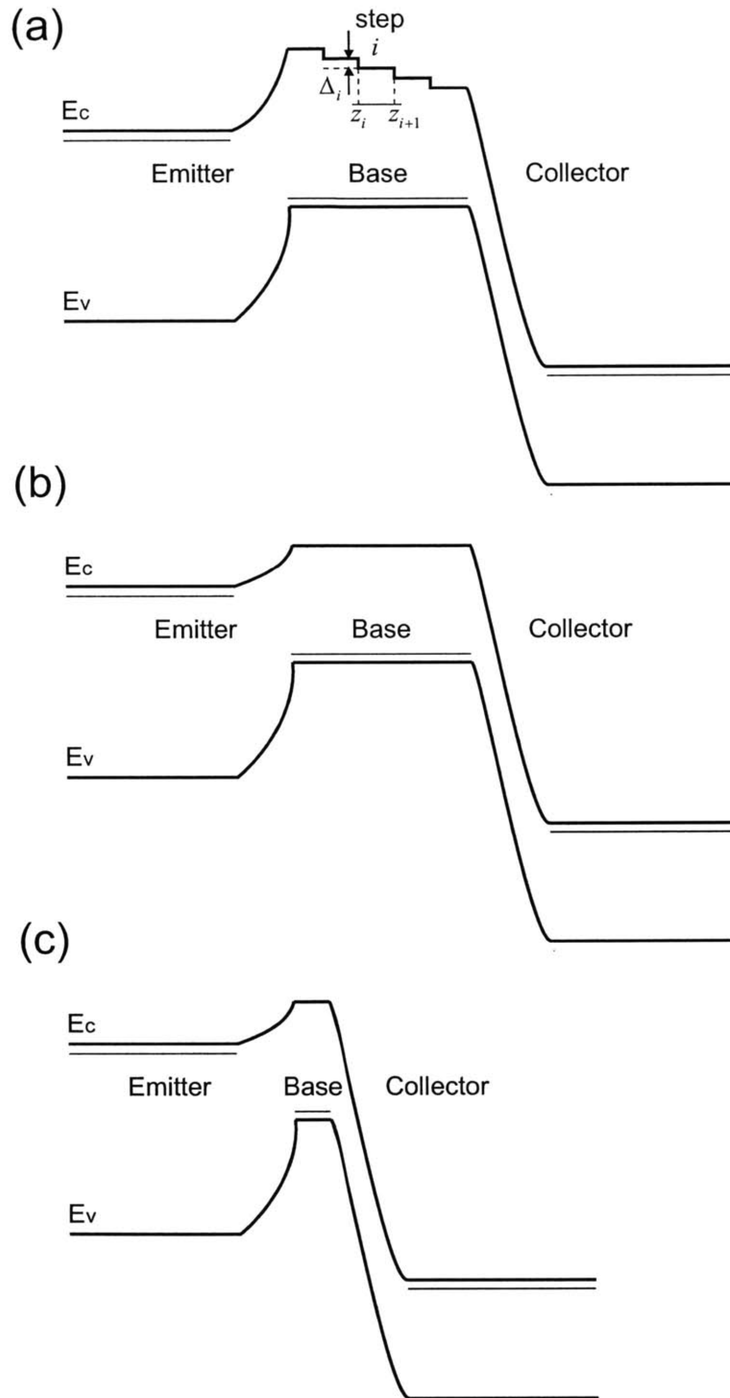

Figure 1-2: Schematic band diagram of (a) a HBT with stepwise alloy-graded base and base thickness $X_{B1}=N \times X_{step1}$, (b) a HBT with uniform base and base thickness $X_{B2}=X_{B1}$, and (c) a HBT with uniform base and base thickness $X_{B3}=X_{step1}$. The base transit time, the magnitude attenuation and phase delay of the total base transport factor attain small values for (c), large values for (b), and intermediate values for (a). These features of (a) are favorable for the implementation of a transit-time oscillator.

Fig. 1-1, the base is stepwise alloy-graded and the band gap discontinuity between successive steps is chosen to be greater than the longitudinal optical (LO) phonon energy $\hbar\omega_{LO}$. At the edge of each base step, the minority carriers undergo fast LO phonon scattering. The LO phonon scattering can be viewed as a resetting mechanism of the diffusive transport and mimics to some extent the perfect sink mechanism of a collector. The forward diffusion is favored and the backward diffusion is limited. Thus, the diffusion velocity in each base step is high since it is determined by the short base step thickness X_{step}. It can be expressed to a first approximation as $v_{diff} = D_n/(2X_{step})$, where D_n is the diffusion constant of minority carriers in the base. The total transit time in a base of N base steps is $\tau_{base} = N \times \tau_{step} = 2{X_B}^2/(N \times D_n)$. Compared to a base with the same base thickness X_B and no base steps (Fig. 1-2(b)), the transit time is N times shorter and the transverse base resistance is the same. Thus, both f_T and f_{max} improve. Compared to a short base with total base thickness equal to X_{step} (Fig. 1-2(c)), the device offers the reverse tradeoff between f_T and f_{max}. The transit time is N times longer but the transverse base resistance is N times smaller. Consequently, f_T shifts to lower frequencies but the power gain frequency performance improves. This is advantageous in millimeter-wave power applications. In addition, a thick base relaxes the emitter etching process and reduces the risk of base metal diffusion into the collector region during an alloying process. According to [24], both linear and stepwise alloy grading can achieve approximately the same base transport for the same X_B if the energy gap difference of the linear alloy grading $\Delta E_{c,linear}$ and the number of steps N of the stepwise alloy grading are related by $\Delta E_{c,linear} \approx (N-1) \times (3k_BT)$. The energy gap difference required by the stepwise alloy-graded base is $\Delta E_{c,stepwise} \approx (N-1) \times \hbar\omega_{LO}$. Given that $k_BT = 25$ meV at T=300 K, $\hbar\omega_{LO} \approx 36$ meV for an $\mathrm{Al_xGa_{1-x}As}$ base, we conclude that $\Delta E_{c,stepwise} < \Delta E_{c,linear}$. Thus, stepwise alloy grading allows more energy gap difference between the emitter and base for the suppression of hole injection from the base to the emitter.

An important transport parameter is the small-signal base transport factor α_T defined as the ratio of small-signal current exiting the base over the small-signal current entering the base. Following the approximate treatment of [24], a stepwise alloy-graded base with N steps is characterized by $\alpha_{T,\mathrm{stepwise}}(\omega) \approx \exp\left(-N\varphi^2/3\right) \times \exp\left(-jN\varphi\right)$, where $\varphi \equiv \omega {X_{step}}^2/(2D_n)$, whereas a uniform base of thickness X_B is characterized by $\alpha_{T,\mathrm{uniform}}(\omega) \approx \exp\left(-\theta^2/3\right) \times \exp\left(-j\theta\right)$, where $\theta \equiv \omega {X_B}^2/(2D_n)$. It is enlightening to consider the following three cases: (1) a HBT with a stepwise alloy graded base with N steps of base step thickness X_{step1} (Fig. 1-2(a)), (b) a HBT with a long uniform base of thickness $X_{B2} = N \times X_{step1}$ (Fig. 1-2(b)), and (c) a HBT with a short uniform base of thickness $X_{B3} = X_{step1}$ (Fig. 1-2(c)). Therefore, the base transport factors are for the stepwise alloy graded base (1) $\alpha_{T1}(\omega) \approx \exp\left(-N\varphi_1^2/3\right) \times \exp\left(-jN\varphi_1\right)$, for the long base (2) $\alpha_{T2}(\omega) \approx \exp\left(-N^4\varphi_1^2/3\right) \times \exp\left(-jN^2\varphi_1\right)$, and for the short base (3) $\alpha_{T3}(\omega) \approx \exp\left(-\varphi_1^2/3\right) \times \exp\left(-j\varphi_1\right)$, where $\varphi_1 \equiv \omega {X_{step1}}^2/(2D_n)$. Device (2) shows large phase delay and magnitude attenuation, device (3) undergoes small phase delay and magnitude attenuation, and device (1) demonstrates

intermediate phase delay and magnitude attenuation.

This work focuses on the potential of the device as a transit-time oscillator. A high-bandwidth HBT design calls for minimum transport delays of carriers. On the contrary, transit-time oscillators take advantage of these transport delays that, and if properly selected, can lead to millimeter-wave oscillations. These devices consist of an injector and a drift region [25]. The most important features of the injector are the current magnitude attenuation and the current phase delay acquired during the transport of carriers across the injector. If the magnitude attenuation is limited and the phase delay is sufficient, the current exiting and the voltage applied across the drift region can differ in phase by π radians creating a negative resistance. It should be emphasized that the emergence of negative resistance is an intrinsic device property and not the result of a feedback circuit which is commonly used for three-terminal oscillators. In this work, the emitter-base region is the injector, the depleted collector is the drift region and the injection mechanism is diffusion enchanced by LO phonon scattering. The base transport factor incorporates the magnitude attenuation and phase delay of the injector. Following the previous descussion, the HBT with the stepwise alloy-graded base is suitable for transit-time oscillations since the base transport factor undergoes intermediate phase delay and magnitude attenuation. On the contrary, a HBT with a long or short uniform base is characterized by large magnitude attenuation or small phase delay, respectively, and millimeter-wave oscillations are difficult to achieve. Furthermore, the intermediate magnitude attenuation of the device of interest leads to more tolerance to parasitics compared to an HBT of long base.

1.2 Thesis Overview

The scope of this work is the theoretical analysis of carrier trasport, the design, fabrication, and characterization of a HBT with a stepwise alloy-graded base. The theoretical framework for the HBT of this work is laid in Chapter 2. The Boltzmann transport equation is solved numerically in one dimension across the device and at arbitrary frequencies. A small-signal equivalent circuit is devised where both the intrinsic and the extrinsic HBT are incorporated. Simulation results and high frequency figures of merit cast light on the potential of the device as a transit-time oscillator. The details of the design and fabrication process are presented in Chapter 3. The MBE design and the device layout reflect the aim for transit-time oscillations within the limitations of the fabrication capabilities of our clean room and the demand for ease of fabrication and reduced cost. The choices of the ohmic contacts, the transmission line design, the on-wafer calibration structures, and the device isolation scheme will be discussed. In addition, Appendix A describes in detail all the steps of the process flow. The experimental results are presented an analyzed in Chapter 4. These include the development of the HBT ohmic contacts and DC measurements of HBTs with different device layouts and MBE designs. We summarize the conclusions of this work in Chapter 5.

Chapter 2

Theoretical Analysis

2.1 HBT vs BJT

The HBT differs from the bipolar junction transistor (BJT) in the band structure. For the latter, the same semiconductor is used for the emitter, base, and collector. Thus, the band gap is uniform across the device. The selection of the emitter and base semiconductors for the former is such that the emitter band gap is larger than the base band gap. This subtle difference leads to dramatic consequencies in the design and performance of HBTs [26].

During the forward operation of a npn BJT shown in Fig. 2-1, the emitter-base junction is forward biased ($V_{BE} \geq 0$) and the base-collector junction is reverse biased ($V_{BC} \leq 0$). As the forward bias V_{BE} increases, more electrons are thermionically injected from the emitter into the base and they diffuse across the base. At the same time, thermionic injection of holes from the base into the emitter takes place. The electron flow $\vec{F}_e$ and the hole flow $\vec{F}_e$ are illustrated in Fig. 2-1, and $\vec{F}_e \equiv n\vec{v}_e$, $\vec{F}_h \equiv p\vec{v}_h$, where n, p is the electron and hole concentration, respectively, and $\vec{v}_e$, $\vec{v}_h$ is the electron and hole velocity, respectively. Some electrons and holes recombine in the space charge region of the emitter-base junction and in the bulk of the base. The base thickness is much smaller than the diffusion length L_n of electrons in the base so that a large number of electrons reach the base-collector junction and sweep across the depleted collector. The diffusion length is the length where the electron concentration would decrease by a factor of e^{-1} from its maximum value if the base thickness was very large, and it is given by $L_n \equiv \sqrt{D_n \tau_n}$, where D_n is the diffusion constant of electrons in the base and τ_n is the time constant for the generation and recombination processes in the base. The only available design tool is the selection of the doping level N and the thickness X of each region. An amplifier calls for high current gain $\beta \equiv I_c/I_b$. If $N_E > N_B$, the free electrons in the emitter region outnumber the free holes in the base region. Therefore, the electron current injected into the base is larger than the hole current injected into the emitter leading to high current

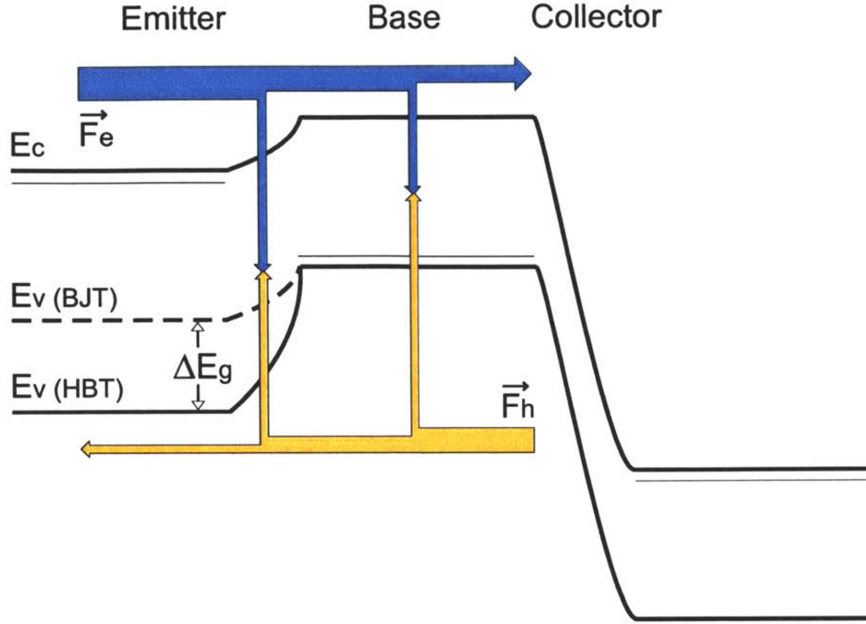

Figure 2-1: Band diagram of a HBT and a BJT. The dotted line corresponds to the valence band of the BJT in the emitter. The emitter-base junction of the HBT is smoothly alloy-graded. The electron and hole flow is $\vec{F_e}$ and $\vec{F_h}$ respectively. Electrons and holes recombine mainly in the space charge region and in the bulk of the base. The electrons that have not recombined are swept across the collector. The HBT exhibits limited hole injection from the base into the emitter due to the presence of ΔE_g in the valence band.

gain.

The HBT offers an additional feature. The emitter band gap is larger than the base band gap. For a smoothly alloy-graded emitter-base junction shown in Fig. 2-1, all the band gap difference between the emitter and base ΔE_g manifests in the valence band. The hole current injected into the emitter is severely limited due to the presence of the additional barrier ΔE_g. Therefore, the choice of the heterojunction alone can increase dramatically the current gain of the HBT and the design restrictions of the BJT in the selection of doping levels can be lifted. A heavily doped base is advantageous in lowering the base ohmic contact and the transverse base resistance. This is instrumental for the microwave/millimeter wave power capability of the HBT.

The above arguments can be clarified quantitatively. If we neglect the electron-hole recombination, the collector current is $I_C = Aq\left|\vec{F_e}\right|$, where A is the area of the intrinsic cross section. The law of the junction dictates that the electron concentration in the base is expressed as $n = \left(n_{i,B}^2/N_B\right) e^{(qV_{BE})/(k_BT)}$, where $n_{i,B}$ is the intrinsic carrier concentrations in the base. The electron diffusion velocity is $|\vec{v}_e| = D_n/X_B$, where X_B is the base thickness. Therefore, the collector current is $I_C = Aq\left(n_{i,B}^2/N_B\right) e^{(qV_{BE})/(k_BT)}\left(D_n/X_B\right)$. Similar arguments hold for the base current and $I_B = Aq\left(n_{i,E}^2/N_E\right) e^{(qV_{BE})/(k_BT)}\left(D_p/X_E\right)$, where $n_{i,E}$ is the intrinsic concentration in the

emitter, D_p is the diffusion contant of holes in the emitter, and X_E is the emitter thickness. Therefore, the static current gain can be expressed as $\beta = (D_n/D_p)(X_E/X_B)(N_E/N_B)(n_{i,B}^2/n_{i,E}^2)$. In general, the intrinsic carrier concentration in a semiconductor with band gap E_g is given by $n_i = \sqrt{N_C N_V} e^{-E_g/(2k_BT)}$, where N_C and N_V are the conduction and valence band density of states respectively. In a BJT, the band gap is uniform across the device and $n_{i,B}/n_{i,E} = 1$. Therefore, the static current gain is $\beta = (D_n/D_p)(X_E/X_B)(N_E/N_B)$ and the choice $N_E > N_B$ leads to high β. In a HBT, the band gap in non-uniform so $n_{i,B}/n_{i,E} = e^{\Delta E_g/(2k_BT)}$, assuming for simplicity that $N_{C,B}N_{V,B}/(N_{C,B}N_{V,B}) \approx 1$. Thus, the static current gain is $\beta = (D_n/D_p)(X_E/X_B)(N_E/N_B)e^{\Delta E_g/(k_BT)}$. The exponential factor alone leads to a substantially high β regardless of N_E and N_B.

2.2 HBT in the Diffusive Transport Approximation

We consider the case of a HBT with a base of uniform bandgap and doping. The emitter-base junction is at $z = 0$ and the base-collector junction is at $z = X_B$. The diffusion current approximation and the electron continuity in the base yield the diffusion equation

$$D_n \frac{\partial^2 n}{\partial z^2} - \frac{n - n_{B0}}{\tau_n} - \frac{\partial n}{\partial t} = 0, \tag{2.1}$$

where n is the electron concentration in the base and $n_{B0} \equiv n_{i,B}^2/N_B$. If the applied biases at the emitter-base and base-collector junction include a dc and ac part, then both the static and the high frequency operation of the device can be found by solving Eq. 2.1. For applied voltages $V_{be}(t) = \overline{V}_{BE} + \hat{v}_{be}\exp(j\omega t)$, and $V_{cb}(t) = \overline{V}_{CB} + \hat{v}_{cb}\exp(j\omega t)$, the electron concentration and the electron current can be expressed as $n(z,t) = \bar{n}(z) + \hat{n}(z)\exp(j\omega t)$, and $I_n(z,t) = \overline{I}_n(z) + \hat{i}_n(z)\exp(j\omega t)$, respectively. Therefore, the diffusion equations for the static and high frequency concetration, $\bar{n}$ and $\hat{n}$, respectively, can be readily derived from Eq. 2.1.

At $z = 0$, the injected carriers follow the Maxwell distribution whereas at $z = X_B$ the electron concentration vanishes due to the strong electric field in the depleted collector. For simplicity, we ignore the Early effect since the base width modulation due to $\hat{v}_{cb}$ is expected to be limited for a heavily doped base. Therefore, the boundary conditions of Eq. 2.1 are $n(0) = n_{B0}\exp[qV_{be}/(k_BT)]$, and $n(X_B) \approx 0$. The static and high frequency boundary conditions can be easily extracted from the expression of V_{be}. After a simple mathematical treatment, the solutions $\bar{n}$ and $\hat{n}$ of the diffusion equation are given by:

$$\bar{n}(z) = n_{B0}\left\{1 - \frac{\sinh(z/L_n)}{\sinh(X_B/L_n)} + \left[\exp\left(\frac{q\overline{V}_{BE}}{k_BT}\right) - 1\right]\frac{\sinh[(X_B - z)/L_n]}{\sinh(X_B/L_n)}\right\}, \tag{2.2}$$

$$\hat{n}(z) = n_{B0}\exp\left(\frac{q\overline{V}_{BE}}{k_BT}\right)\frac{q\hat{v}_{be}}{k_BT}\frac{\sinh[\zeta(X_B - z)]}{\sinh(\zeta X_B)}, \tag{2.3}$$

where $\zeta \equiv L_n^{-1}\sqrt{1+j\omega\tau_n}$ is the inverse of the ac diffusion length. From Eqs. 2.2-2.3, we obtain the diffusion currents $\bar{I}_n$, $\hat{i}_n$:

$$\bar{I}_n(z) = qD_nA_en_{B0}\left\{\frac{\cosh(z/L_n)}{L_n\sinh(X_B/L_n)} + \left[\exp\left(\frac{q\overline{V}_{BE}}{k_BT}\right) - 1\right]\frac{\cosh[(X_B - z)/L_n]}{L_n\sinh(X_B/L_n)}\right\}, \tag{2.4}$$

$$\hat{i}_n(z) = qD_nA_en_{B0}\exp\left(\frac{q\overline{V}_{BE}}{k_BT}\right)\frac{q\hat{v}_{be}}{k_BT}\zeta\frac{\cosh[\zeta(X_B - z)]}{\sinh(\zeta X_B)}, \tag{2.5}$$

where A_e is the cross-section of the intrinsic device. For a relatively large $\overline{V}_{BE}$, and $X_B \ll L_n$, the following approximations of Eqs. 2.4-2.5 are very common in literature:

$$\bar{I}_E \equiv \bar{I}_n(z=0) \approx qD_nA_e\left(n_i^2/N_B\right)\exp\left[q\overline{V}_{BE}/(k_BT)\right]X_B^{-1}, \tag{2.6}$$

$$\hat{i}_n(z) \approx \left[\bar{I}_E/V_{Th}\right]\zeta X_B\cosh[\zeta(X_B - z)]\sinh(\zeta X_B)^{-1}\hat{v}_{be}, \tag{2.7}$$

where $V_{Th} \equiv k_BT/q$. The small-signal base transport factor is defined as the ratio of the small-signal electron current exiting the base over the small-signal electron current entering the base, namely, $\alpha_T(\omega) \equiv \hat{i}_n(X_B)\big/\hat{i}_n(0)$. Therefore, the base transport factor of a HBT with uniform base in the diffusion approximation is

$$\alpha_T(\omega) = \cosh(\zeta X_B)^{-1}. \tag{2.8}$$

We now consider the HBT with a stepwise alloy-graded base. Luryi and Grinberg adopted in [24] an approximate approach. The transport of minority carriers in a base step is treated as diffusive. The LO phonon scattering is considered as a perfect resetting mechanism. The exchange of energy between the highly energetic minority carriers at the edge of the base step and the lattice is assumed to take place at a length much smaller than the base step. From this perspective, the minority carriers follow an ideal Maxwell distribution at almost the beginning of each base step. The boundary conditions are: (1) Maxwell distribution of carriers at the beginning of the first step, and (2) vanishing electron concentration at the base step end. Furthermore, the continuity of current between base steps is applied. For simplicity, we assume that the diffusion constant D_n and the intrinsic concentration n_i are the same throughout the base.

A simple device physics analysis similar to the one followed for the HBT of uniform base can be used for the HBT with a stepwise alloy-graded base. We simplify the dc analysis by keeping only the terms weighted by $\exp\left[q\overline{V}_{BE}/(k_BT)\right]$. For the first step, the solutions of Eqs. 2.2-2.5 apply with the minor modification $X_B \to X_{step}$. For the rest of the steps, the following recursive relations apply for the static case: $\bar{n}(z) = \alpha\bar{n}(z - X_{step})$, and $\bar{i}_n(z) = \alpha\bar{i}_n(z - X_{step})$, where $\alpha \equiv \cosh(X_{step}/L_n)^{-1}$ is the dc base step transport factor. For $X_{step} \ll L_n$, the dc transport factor is close to unity and the dc minority carrier concentration becomes almost periodic. Similarly, the following relations hold for the ac case: $\hat{n}(z) = \alpha_b\hat{n}(z - X_{step})$, and $\hat{i}_n(z) = \alpha_b\hat{i}_n(z - X_{step})$, where $\alpha_b \equiv \cosh(\zeta X_{step})^{-1}$ is the ac base step transport factor. The base step transport factor scales both the carrier concentration and the current. A direct consequence of this approximate approach is that

the total small-signal base transport factor can be expressed as a cascade of the base step transport factors, $\alpha_T = \alpha_b^N = \cosh\left(\zeta X_{step}\right)^{-N}$.

However, this simple analysis fails to incorporate the details of the LO phonon scattering. The edge of a base step can not be treated as a perfect sink mechanism. There is a finite distance that the carriers travel for an effective exchange of energy with the lattice. In addition, hot electrons diffuse forward and backward. All these non-idealities can be revealed by solving the Boltzmann transport equation (BTE) along the base structure. A numerical method was proposed in [27]-[28] where the BTE is solved in a field-free base. The BTE was analyzed in [29] for a stepwise graded potential energy. This method was used to analyze the dc transport of carriers in a Si region where a constant static field was applied. The elastic processes involved were the acoustic phonon and the impurity scattering, and nonpolar optical phonon scattering was the only the non-elastic process studied. The static case of a uniform GaAs base was considered in [30] where LO phonon scattering was incorporated. The work of [31] focused on the quasi-ballistic transport in a uniform base using the flux approach and the method of [27]-[28].

In this work, we analyze an AlGaAs/GaAs HBT with a stepwise alloy-graded base at arbitrary frequencies from the perspective of the BTE [32]. Our approach unifies the methods of [29] and [30]. The intrinsic operation of the device will be described from the BTE solutions. Subsequently, we will follow a circuit approach that incorporates the intrinsic and extrinsic elements. Important figures of merit will be extracted to emphasize the transit-time oscillation capability of this device.

2.3 Formulation of BTE

Let us assume that the base structure consists of N base steps. We investigate the transport of minority carriers in one dimension, along the base thickness. This is essential for the reduction of mathematical complexity and adequate for the description of the intrinsic device properties. The emitter-base and base-collector junctions are located at $z = 0$ and $z = X_B$ respectively. The base step ν extends from z_ν to $z_{\nu+1}$, so $z_1 = 0$ and $z_{N+1} = X_B$. The conduction band discontinuity at z_ν, is $\Delta_\nu \equiv E_C\left(z_\nu+\right) - E_C\left(z_\nu-\right)$. The base is heavily and uniformly p-doped. For a degenerate semiconductor, the Joyce-Dixon approximation holds:

$$E_V - E_f = k_B T \times \left[\ln r + A_1 r + A_2 r^2 + A_3 r^3 + A_4 r^4\right], \tag{2.9}$$

where $r \equiv N_B/N_V$, $N_V \equiv 2\left(2\pi k_B T m_{dh}/h^2\right)^{3/2}$ is the valence band density of states, m_{dh} is the effective hole mass, $A_1 \equiv 1/\sqrt{8}$, $A_2 \equiv -4.95009 \times 10^{-3}$, $A_3 \equiv 1.48386 \times 10^{-4}$, and $A_4 \equiv -4.42563 \times 10^{-6}$. If we ignore the effective hole mass variation, N_V is constant along the base. Therefore, since N_B is the same for all base steps, it follows from Eq. 2.9 that the energy difference $E_V - E_f$ is the same for all base steps. Consequently, the alignment of the Fermi level in the quasi-neutral base leads approximately to the alignment of the valence band. Thus, the conduction

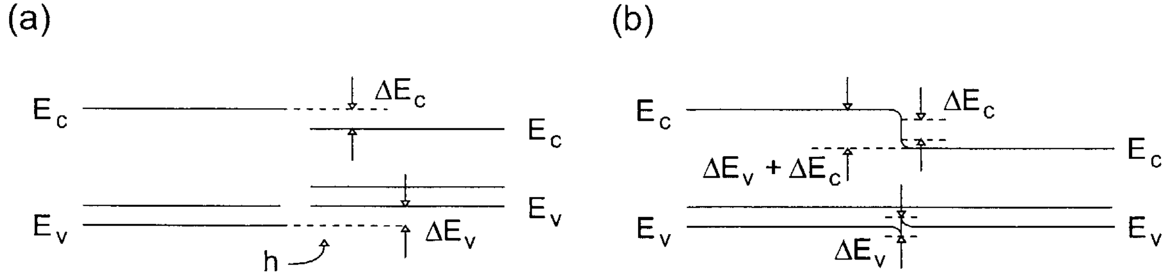

Figure 2-2: Band diagram of two base steps (a) before thermal equilibrium, and (b) after thermal equilibrium. Holes are transported from the base step of larger bandgap to the base step of smaller bandgap. The bandgap difference appears in the conduction band after a few Debye lengths from the base step edge.

band discontinuity is approximately equal to the band gap discontinuity, $\Delta_\nu \approx E_g(z_\nu+) - E_g(z_\nu-)$. These arguments can also be followed by the band diagram of Fig. 2-2. Holes are trasported from the base step of wider bandgap to the base step of smaller bandgap. The distance where the transport of holes takes place is a few Debye lengths, where the Debye length is $L_D \equiv \sqrt{\varepsilon k_B T/(q^2 N_B)}$. For $N_B = 2 \times 10^{19}$ cm^{-3}, $L_D \approx 10$ Å.

The BTE links the distribution function of minority carriers f_ν with the various scattering mechanisms. We consider the impurity and the polar optical phonon scattering as the dominant elastic and inelastic scattering processes, respectively, since the doping level in the base is high ($> 10^{19}$cm^{-3}) and $|\Delta_\nu| > \hbar\omega_{LO}$. The recombination in the base is not examined since it is expected to affect only the low frequency performance. In a field-free region, the time-dependent BTE assumes the form

$$\frac{\partial f_\nu(z,\boldsymbol{k},t)}{\partial t} = -\frac{\hbar k_z}{m^*}\frac{\partial f_\nu(z,\boldsymbol{k},t)}{\partial z} + \frac{\hbar k}{m^*}\left\{S_{in}\left[f_\nu(z,\boldsymbol{k},t)\right] - S_{out}\left[f_\nu(z,\boldsymbol{k},t)\right]\right\}, \tag{2.10}$$

where $\boldsymbol{k}$ is the particle wave vector, m^* is the effective mass of the minority carriers, S_{in} and S_{out} are associated with the scattering into and out of the state $\boldsymbol{k}$ respectively. The outgoing scattering term S_{out} can be replaced by the inverse of the total scattering length l_{tot}, and

$$l_{tot}^{-1} \equiv l_{imp}(E_{\nu,k})^{-1} + l_+(E_{\nu,k})^{-1} + l_-(E_{\nu,k})^{-1}, \tag{2.11}$$

where $E_{\nu,k}$ is the kinetic energy of the carriers in the ν base step, l_{imp} is the impurity scattering length, l_+, l_- are the polar optical phonon emission and absorption scattering lengths respectively. The energy-dependent expressions of these scattering lengths are

$$l_{imp}(E_{\nu,k})^{-1} = q^4 m^* N_{imp} L_D^2 / \left\{2\pi\varepsilon^2\hbar\left[4E_{\nu,k} + \hbar^2/(2m^* L_D^2)\right]\right\}, \tag{2.12}$$

$$l_\pm(E_{\nu,k})^{-1} = \theta\left(E_{\nu,k} - \hbar\omega_{LO}\frac{1\pm1}{2}\right)\frac{r_\varepsilon m^* q^2 \omega_{LO}}{4\pi\hbar E_{\nu,k}}\left(n_{op} + \frac{1\pm1}{2}\right)\sinh^{-1}\left(\sqrt{\frac{E_{\nu,k}}{\hbar\omega_{LO}} - \frac{1\pm1}{2}}\right), \tag{2.13}$$

where N_{imp} is the impurity concentration, $L_D \equiv \sqrt{\varepsilon k_B T/(q^2 N_{imp})}$ is the Debye length, θ is the unit step function, $n_{op} \equiv (\exp[\hbar\omega_{LO}/(k_B T)] - 1)^{-1}$, $r_\varepsilon \equiv \varepsilon_\infty^{-1} - \varepsilon^{-1}$, ε and ε_∞ are the low and high frequency permittivity of the material respectively. The unit step function is used to distinguish that LO phonon emission takes place only when $E_{\nu,k} > \hbar\omega_{LO}$. Since LO phonon scattering correlates the energy levels $E_{\nu,k}$ and $E_{\nu,k} \pm \hbar\omega_{LO}$, it is convenient to introduce the notation ${}^iE_{\nu,k} \equiv {}^0E_{\nu,k} \pm i\hbar\omega_{LO}$, where $i = -1, 0, 1$ and ${}^0E_{\nu,k}$ is a particular energy level.

Since $\boldsymbol{k} = \hat{z}k\cos\theta + \hat{\rho}k\sin\theta$, where $\cos\theta \equiv \boldsymbol{k}\cdot\hat{z}/k$, we could reperesent $\boldsymbol{k}$ in f_ν by $u_\nu \equiv \cos\theta$ and the magnitude k. In addition, the magnitude k can be represented by the total kinetic energy $E_{\nu,k}$. The substitution $f_\nu(z, E_{\nu,k}, u_\nu, t) = f_\nu(z, E_{\nu,k}, u_\nu)\exp(j\omega t)$ in Eq. 2.10 leads to the frequency-dependent BTE

$$u_\nu \frac{\partial f_\nu\left(z, {}^0E_{\nu,k}, u_\nu\right)}{\partial z} + \frac{f_\nu\left(z, {}^0E_{\nu,k}, u_\nu\right)}{{}^0l_{\nu,k}} = R_\nu\left(z, {}^0E_{\nu,k}, u_\nu\right), \tag{2.14}$$

where $R_\nu\left(z, {}^0E_{\nu,k}, u_\nu\right) \equiv S_{in}\left[f_\nu\left(z, {}^0E_{\nu,k}, u_\nu\right)\right]$ and ${}^il_{\nu,k}^{-1} \equiv l_{tot}\left({}^iE_{\nu,k}\right)^{-1} + j\omega\sqrt{m^*/(2\,{}^iE_{\nu,k})}$ for $i = -1, 0, 1$. Therefore, the frequency dependence appears explicitly in the imaginary part of ${}^il_{\nu,k}^{-1}$. The transport degradation in frequency takes place as $\left|{}^il_{\nu,k}\right|$ decreases and $\left|\angle\,{}^il_{\nu,k}\right|$ increases. The in-going scattering term $R_\nu\left(z, {}^0E_{\nu,k}, u_\nu\right)$ links the final state $f_\nu\left(z, {}^0E_{\nu,k}, u_\nu\right)$ with the initial states $f_\nu\left(z, {}^0E_{\nu,k}, u'_\nu\right)$, $f_\nu\left(z, {}^0E_{\nu,k} + \hbar\omega_{LO}, u'_\nu\right)$, and $f_\nu\left(z, {}^0E_{\nu,k} - \hbar\omega_{LO}, u'_\nu\right)$ via impurity, LO phonon emission, and LO phonon absorption scattering, respectively. Since these mechanisms are anisotropic, it is essential to link the angle $\angle\left(\hat{z}, \boldsymbol{k}'\right) = \cos^{-1}\left(u'_\nu\right)$ of the initial state with the angle $\angle\left(\hat{z}, \boldsymbol{k}\right) = \cos^{-1}\left(u_\nu\right)$ of the final state. This is accomplished by the appropriate scattering kernels that weight the initial states. Therefore, the in-going scattering term and the kernels can be expressed as

$$R_\nu\left(z, {}^0E_{\nu,k}, u_\nu\right) \equiv \sum_{i=-1}^{1}\int_{-1}^{1} f_\nu\left(z, {}^0E_{\nu,k}, u'_\nu\right) K_i\left({}^0E_{\nu,k}, u_\nu, u'_\nu\right) du'_\nu, \tag{2.15}$$

$$K_0\left({}^0E_{\nu,k}, u, u'\right) \equiv \frac{q^4 N_{imp}}{8\pi\varepsilon^2} \frac{\left[2\left(1-uu'\right){}^0E_{\nu,k} + \hbar^2/(2m^*L_D^2)\right]}{\left\{\left[2\left(1-uu'\right){}^0E_{\nu,k} + \hbar^2/(2m^*L_D^2)\right]^2 - 4\left(1-u^2\right)\left(1-u'^2\right){}^0E_{\nu,k}^2\right\}^{\frac{3}{2}}}, \tag{2.16}$$

$$K_{\pm1}\left({}^0E_{\nu,k}, u, u'\right) \equiv \frac{\theta\left({}^{\pm1}E_{\nu,k}\right)\left[q^2 m^*\omega_{LO} r_\varepsilon/(8\pi\hbar)\right]\left[n_{op} + \frac{1\pm1}{2}\right]\sqrt{\left({}^{\pm1}E_{\nu,k}/{}^0E_{\nu,k}\right)}}{2\left[\left({}^0E_{\nu,k} \pm 0.5\hbar\omega_{LO} - uu'\sqrt{{}^0E_{\nu,k}}\sqrt{{}^{\pm1}E_{\nu,k}}\right)^2 - {}^0E_{\nu,k}\,{}^{\pm1}E_{\nu,k}\left(1-u^2\right)\left(1-u'^2\right)\right]^{\frac{1}{2}}}, \tag{2.17}$$

where K_0, K_{-1}, K_{+1} are the kernels associated with impurity, LO phonon absorption, and LO phonon emission scattering respectively. The unit function θ signifies that LO phonon absorption is possible only if the energy ${}^0E_{\nu,k}$ of the final state is larger than $\hbar\omega_{LO}$.

Nonpolar optical phonon scattering has been treated by an approximate isotropic approach in [29]. The simplification $R_\nu\left(z, {}^0E_{\nu,k}, u_\nu\right) \approx R_\nu\left(z, {}^0E_{\nu,k}\right)$ reduces significantly the mathematical

complexity of the BTE solution. A similar approach can be adopted for the polar LO phonon scattering if we make use of the approximation

$$R_\nu\left(z, {}^0E_{\nu,k}\right) \approx \sum_{i=-1}^{1} \left[\int_{-1}^{1} K_i\left({}^0E_{\nu,k}, 0, u'_\nu\right) du'_\nu\right] \times \left[(1/2)\int_{-1}^{1} f_\nu\left(z, {}^0E_{\nu,k}, u'_\nu\right) du'_\nu\right]. \qquad (2.18)$$

The substitution of the kernels K_0, $K_{\pm}1$ in Eq. 2.18 leads to

$$R_\nu\left(z, {}^0E_{\nu,k}\right) \approx \sum_{i=-1}^{1} A_i\left({}^0E_{\nu,k}\right) f_\nu^{(0)}\left(z, {}^iE_{\nu,k}\right), \qquad (2.19)$$

$$A_0\left({}^0E_{\nu,k}\right) \equiv l_{imp}\left({}^0E_{\nu,k}\right)^{-1}, \qquad (2.20)$$

$$A_{\pm 1}\left({}^0E_{\nu,k}\right) \equiv \theta\left({}^{\pm 1}E_{\nu,k}\right) \frac{r_\varepsilon m q^2 \omega_{LO}}{4\pi\hbar^0 E_{\nu,k}} \left(n_{op} + \frac{1 \pm 1}{2}\right) \sinh^{-1}\left(\sqrt{\frac{{}^0E_{\nu,k}}{\hbar\omega_{LO}} - \frac{1 \mp 1}{2}}\right), \qquad (2.21)$$

where $f_\nu^{(0)}\left(z, {}^iE_{\nu,k}\right) \equiv (1/2)\int_{-1}^{1} f_\nu\left(z, {}^iE_{\nu,k}, u'_\nu\right) du'_\nu$ and A_0, A_{-1}, A_{+1} refer to impurity, LO phonon absorption, and LO phonon emission scattering respectively. From Eq. 2.19 it is evident that the final state is linked with the initial states $f_\nu{}^{(0)}\left(z, {}^0E_{\nu,k},\right)$, $f_\nu^{(0)}\left(z, {}^0E_{\nu,k} + \hbar\omega_{LO}\right)$, and $f_\nu^{(0)}\left(z, {}^0E_{\nu,k} - \hbar\omega_{LO}\right)$. Careful examination of A_{+1} reveals that the states with initial energy $\hbar\omega_{LO}$ are weighted more. Thus, LO phonon emission for the final state ${}^0E_{\nu,k} = 0$ is pronounced.

It is convenient to introduce the half-space distribution functions and collision terms. We define $f_\nu^{(\pm)}\left(z, {}^0E_{\nu,k}, u_\nu\right) \equiv f_\nu\left(z, {}^0E_{\nu,k}, \pm|u_\nu|\right)$ and $R_\nu^{(\pm)}\left(z, {}^0E_{\nu,k}, u_\nu\right) \equiv R_\nu\left(z, {}^0E_{\nu,k}, \pm|u_\nu|\right)$ for $0 \leq u_\nu \leq 1$. The superscripts $(+)$ and $(-)$ are used to imply forward and backward transport respectively. The solution of the frequency-dependent BTE consists of the homogeneous and special solution of Eq. 2.14. Therefore, the BTE solution for $z_\nu \leq z \leq z_{\nu+1}$ and $0 \leq u_\nu \leq 1$ can be expressed as

$$f_\nu^{(+)}\left(z, {}^iE_{\nu,k}, u_\nu\right) = f_\nu^{(+)}\left(z_\nu, {}^iE_{\nu,k}, u_\nu\right) \exp\left(\frac{z_\nu - z}{{}^il_{\nu,k}u_\nu}\right) + \frac{1}{u_\nu}\int_{z_\nu}^{z} R_\nu^{(+)}\left(z', {}^iE_{\nu,k}, u_\nu\right) \exp\left(\frac{z' - z}{{}^il_{\nu,k}u_\nu}\right) dz', \qquad (2.22)$$

$$f_\nu^{(-)}\left(z, {}^iE_{\nu,k}, u_\nu\right) = f_\nu^{(-)}\left(z_{\nu+1}, {}^iE_{\nu,k}, u_\nu\right) \exp\left(\frac{z - z_{\nu+1}}{{}^il_{\nu,k}u_\nu}\right) + \frac{1}{u_\nu}\int_{z}^{z_{\nu+1}} R_\nu^{(-)}\left(z', {}^iE_{\nu,k}, u_\nu\right) \exp\left(\frac{z - z'}{{}^il_{\nu,k}u_\nu}\right) dz'. \qquad (2.23)$$

2.4 Solution of BTE

A systematic method can be devised for the solution of the BTE along the base. According to the general expressions of $f_\nu^{(+)}$ and $f_\nu^{(-)}$ in Eqs. 2.22-2.23 for $z_\nu \leq z \leq z_{\nu+1}$, it is essential to know the values of $f_\nu^{(+)}$ at z_ν and $f_\nu^{(-)}$ at $z_{\nu+1}$. However, these are unknown. If we manage to express the boundary conditions by the values of $f_{\nu-1}^{(+)}$ at z_ν and $f_{\nu+1}^{(-)}$ at $z_{\nu+1}$, then the solution of the BTE at the base step ν will depend upon the solutions $f_{\nu-1}^{(+)}$ in the base step $\nu - 1$ and $f_{\nu+1}^{(-)}$ in the

base step $\nu+1$. Therefore, a recursive scheme can be implemented. The continuity of current, the conservation of energy and the conservation of the magnitude of lateral momentum will be applied at the base endpoints for the derivation of boundary conditions.

The differential forward and backward current density, $dJ_\nu^{(+)}$ and $dJ_\nu^{(-)}$, can be expressed in terms of $f_\nu^{(+)}$ and $f_\nu^{(-)}$ in the form

$$dJ_\nu^{(\pm)}\left(z,{}^iE_{\nu,k},u_\nu\right)=\left[2q\big/(2\pi)^3\right]\left(\hbar k_{z,\nu}/m^*\right)f_\nu^{(\pm)}\left(z,{}^iE_{\nu,k},u_\nu\right)dk_{\|,\nu}dk_{z,\nu} \tag{2.24}$$

The continuity of $dJ_\nu^{(+)}$ and $dJ_\nu^{(-)}$ at z_ν and $z_{\nu+1}$ respectively, and the conservation of the magnitude of lateral momentum leads to

$$f_{\nu-1}^{(+)}\left(z_\nu,{}^iE_{\nu-1,k},u_{\nu-1}\right)k_{\nu-1,z}dk_{\nu-1,z}=f_\nu^{(+)}\left(z_\nu,{}^iE_{\nu,k},u_\nu\right)k_{\nu,z}dk_{\nu,z}, \tag{2.25}$$

$$f_\nu^{(-)}\left(z_{\nu+1},{}^iE_{\nu,k},u_\nu\right)k_{\nu,z}dk_{\nu,z}=f_{\nu+1}^{(-)}\left(z_{\nu+1},{}^iE_{\nu+1,k},u_{\nu+1}\right)k_{\nu+1,z}dk_{\nu+1,z}. \tag{2.26}$$

Furthermore, the conservation of energy at z_ν and $z_{\nu+1}$ has some important consequencies. First, it follows that $k_{\nu-1,z}dk_{\nu-1,z}=k_{\nu,z}dk_{\nu,z}$ and $k_{\nu,z}dk_{\nu,z}=k_{\nu+1,z}dk_{\nu+1,z}$. Second, there exists a relation between the angles $u_{\nu-1}$ and u_ν of Eq. 2.25 and the angles u_ν and $u_{\nu+1}$ of Eq. 2.26. Specifically, it can be easily found that $u_{\nu-1}=\sqrt{({}^iE_{\nu,k}u_\nu^2+\Delta_\nu)/({}^iE_{\nu,k}+\Delta_\nu)}\equiv{}^i\gamma_{\nu,k}^-$ for ${}^iu_{\nu,k}^-\le u_\nu\le 1$, and $u_{\nu+1}=\sqrt{({}^iE_{\nu,k}u_\nu^2-\Delta_{\nu+1})/({}^iE_{\nu,k}-\Delta_{\nu+1})}\equiv{}^i\gamma_{\nu,k}^+$ for ${}^iu_{\nu,k}^+\le u_\nu\le 1$. In these relations, the angle boundaries are ${}^iu_{\nu,k}^-\equiv\theta(-\Delta_\nu)\times\min\left(1,\sqrt{-\Delta_\nu/{}^iE_{\nu,k}}\right)$, ${}^iu_{\nu,k}^+\equiv\theta(\Delta_{\nu+1})\times\min\left(1,\sqrt{\Delta_{\nu+1}/{}^iE_{\nu,k}}\right)$, and θ is the unit step function. The angle boundaries imply that the transport $f_{\nu-1}^{(+)}\to f_\nu^{(+)}$ is allowed if $\hbar^2k_{\nu,z}^2/(2m)\ge-\Delta_\nu$. Similarly, the condition for the transport $f_{\nu+1}^{(-)}\to f_\nu^{(-)}$ is $\hbar^2k_{\nu,z}^2/(2m)\ge\Delta_{\nu+1}$. Otherwise, reflection takes place. Therefore, the conservation of energy at z_ν and $z_{\nu+1}$ along with Eqs. 2.25-2.26 lead to the boundary conditions of the BTE,

$$f_\nu^{(+)}\left(z_\nu,{}^iE_{\nu,k},u_\nu\right)=\theta\left({}^i\xi_{\nu,k}^-\right)f_{\nu-1}^{(+)}\left(z_\nu,{}^iE_{\nu,k}+\Delta_\nu,{}^i\gamma_{\nu,k}^-\right)+\theta\left(-{}^i\xi_{\nu,k}^-\right)f_\nu^{(-)}\left(z_\nu,{}^iE_{\nu,k},u_\nu\right), \tag{2.27}$$

$$f_\nu^{(-)}\left(z_{\nu+1},{}^iE_{\nu,k},u_\nu\right)=\theta\left({}^i\xi_{\nu,k}^+\right)f_{\nu+1}^{(-)}\left(z_{\nu+1},{}^iE_{\nu,k}-\Delta_{\nu+1},{}^i\gamma_{\nu,k}^+\right)+\theta\left(-{}^i\xi_\nu^+\right)f_\nu^{(+)}\left(z_{\nu+1},{}^iE_{\nu,k},u_\nu\right), \tag{2.28}$$

where ${}^i\xi_{\nu,k}^-\equiv{}^iE_{\nu,k}u_\nu+\Delta_\nu$ and ${}^i\xi_{\nu,k}^+\equiv{}^iE_{\nu,k}u_\nu-\Delta_{\nu+1}$. The first and the last base step deserve special attention. The minority carriers are injected in the first step from the emitter whereas the last step can be viewed as a perfect sink of minority carriers for a sufficient reverse bias V_{CB}. Consequently,

$$f_0^{(+)}\left(z_1,{}^iE_{0,k},u_0\right)=(n_e/N_C)\exp\left[-{}^iE_{0,k}/(k_BT)\right], \tag{2.29}$$

$$f_{N+1}^{(-)}=0, \tag{2.30}$$

where $n_e\equiv n_{B0}\exp\left[q\bar{V}_{BE}/(k_BT)\right]\left[q\hat{v}_{be}/(k_BT)\right]$ is the small signal concentration of minority carriers at $z=0$, $\overline{V}_{BE}$ and $\widehat{v}_{be}$ are the dc and ac applied voltage between base and emitter, respectively, and $N_C\equiv(1/4)\left[2m^*k_BT/(\pi\hbar^2)\right]^{3/2}$ is the effective density of states in the conduction band.

If we apply repeatedly the boundary conditions of Eqs. 2.27-2.28 on Eqs. 2.22-2.23, the general solution of the BTE along the base can be found. It can be written compactly as

$$f_{\nu}^{(\mu_1)}\left(z,{}^{i}E_{\nu,k},u_{\nu}\right)=\frac{\zeta}{u_{\nu}}\int\limits_{z_{\nu+m}}^{z}R_{\nu}^{(\mu_1)}\left(z',{}^{i}E_{\nu,k},u_{\nu}\right)\exp\left(-\frac{|z-z'|}{{}^{i}l_{\nu,k}u_{\nu}}\right)dz'+\exp\left(-\frac{|z-z_{\nu+m}|}{{}^{i}l_{\nu,k}u_{\nu}}\right)\times\Bigg\{\theta({}^{i}\xi_{\nu,k}^{\mu_2})$$

$$\times f_{\nu+2m-1}^{(\mu_1)}\left(z_{\nu+m},{}^{i}E_{\nu,k}+\zeta\Delta_{\nu+m},{}^{i}\gamma_{\nu,k}^{\mu_2}\right)+\theta\left(-{}^{i}\xi_{\nu,k}^{\mu_2}\right)\theta\left({}^{i}\xi_{\nu,k}^{\mu_1}\right)\Bigg[\exp\left(\frac{z_{\nu}-z_{\nu+1}}{{}^{i}l_{\nu,k}u_{\nu}}\right)$$

$$\times f_{\nu-2m+1}^{(\mu_2)}\left(z_{\nu-m+1},{}^{i}E_{\nu,k}-\zeta\Delta_{\nu-m+1},{}^{i}\gamma_{\nu,k}^{\mu_1}\right)+\frac{1}{u_{\nu}}\int\limits_{z_{\nu}}^{z_{\nu+1}}R_{\nu}^{(\mu_2)}\left(z',{}^{i}E_{\nu,k},u_{\nu}\right)$$

$$\times\exp\left(-\frac{|z'-z_{\nu+m}|}{{}^{i}l_{\nu,k}u_{\nu}}\right)dz'\Bigg]+\frac{\theta\left(-{}^{i}\xi_{\nu,k}^{-}\right)\theta\left(-{}^{i}\xi_{\nu,k}^{+}\right)}{2u_{\nu}\sinh\left(\frac{z_{\nu+1}-z_{\nu}}{{}^{i}l_{\nu,k}u_{\nu}}\right)}\int\limits_{z_{\nu}}^{z_{\nu+1}}\Bigg[R_{\nu}^{(\mu_1)}\left(z',{}^{i}E_{\nu,k},u_{\nu}\right)$$

$$\times\exp\left(-\frac{|z_{\nu-m+1}-z'|}{{}^{i}l_{\nu,k}u_{\nu}}\right)+R_{\nu}^{(\mu_2)}\left(z',{}^{i}E_{\nu,k},u_{\nu}\right)\exp\left(\frac{|z_{\nu-m+1}-z'|}{{}^{i}l_{\nu,k}u_{\nu}}\right)\Bigg]dz'\Bigg\},\qquad(2.31)$$

where $\zeta\equiv\pm1$, $\mu_1\equiv\mathrm{sgn}(\zeta)$, $\mu_2\equiv\mathrm{sgn}(-\zeta)$, and $m\equiv\delta_{\zeta,-1}$. Furthermore, the use of the BTE solution in the definition of the in-going collision terms R_{ν}^{+} and R_{ν}^{-} leads to the general expression

$$R_{\nu}^{(\mu_3)}\left(z,{}^{0}E_{\nu,k},u_{\nu}\right)=\sum_{i=-1}^{1}\sum_{\zeta=+1,-1}\Bigg\{\int\limits_{{}^{i}u_{\nu,k}^{\mu_2}}^{1}f_{\nu+2m-1}^{(\mu_1)}\left(z_{\nu+m},{}^{i}E_{\nu,k}+\zeta\Delta_{\nu+m},{}^{i}\gamma_{\nu,k}^{\mu_2\,\prime}\right)$$

$$\times\Bigg[\exp\left(-\frac{|z-z_{\nu+m}|}{{}^{i}l_{\nu,k}u_{\nu}'}\right)K_i\left({}^{0}E_{\nu,k},\eta u_{\nu},\zeta u_{\nu}'\right)+\theta\left({}^{i}u_{\nu,k}^{\mu_1}-u_{\nu}'\right)$$

$$\times\exp\left(-\frac{|2z_{\nu+1-m}-z-z_{\nu+m}|}{{}^{i}l_{\nu,k}u_{\nu}'}\right)K_i\left({}^{0}E_{\nu,k},\eta u_{\nu},-\zeta u_{\nu}'\right)\Bigg]du_{\nu}'$$

$$+\int\limits_{0}^{1}\frac{\zeta}{u_{\nu}'}\int\limits_{z_{\nu+m}}^{z}\exp\left(-\frac{|z-z'|}{{}^{i}l_{\nu,k}u_{\nu}'}\right)R_{\nu}^{(\mu_1)}\left(z',{}^{i}E_{\nu,k},u_{\nu}'\right)K_i\left({}^{0}E_{\nu,k},\eta u_{\nu},\zeta u_{\nu}'\right)dz'du_{\nu}'$$

$$+\int\limits_{{}^{i}u_{\nu,k}^{\mu_2}}^{{}^{i}u_{\nu,k}^{\mu_1}}\frac{1}{u_{\nu}'}\int\limits_{z_{\nu}}^{z_{\nu+1}}\exp\left(-\frac{|2z_{\nu+1-m}-z-z'|}{{}^{i}l_{\nu,k}u_{\nu}'}\right)R_{\nu}^{(\mu_1)}\left(z',{}^{i}E_{\nu,k},u_{\nu}'\right)K_i\left({}^{0}E_{\nu,k},\eta u_{\nu},-\zeta u_{\nu}'\right)dz'du_{\nu}'$$

$$+\int\limits_{0}^{{}^{i}u_{\nu,k}^{\min}}\int\limits_{z_{\nu}}^{z_{\nu+1}}\left[2\sinh\left(\frac{z_{\nu+1}-z_{\nu}}{{}^{i}l_{\nu,k}u_{\nu}'}\right)u_{\nu}'\right]^{-1}\Bigg[R_{\nu}^{(\mu_1)}\left(z',{}^{i}E_{\nu,k},u_{\nu}'\right)\exp\left(\frac{z_{\nu}+\zeta(z'-z)-z_{\nu+1}}{{}^{i}l_{\nu,k}u_{\nu}'}\right)$$

$$+R_{\nu}^{(\mu_2)}\left(z',{}^{i}E_{\nu,k},u_{\nu}'\right)\exp\left(\zeta\frac{z_{\nu+1}+z_{\nu}-z-z'}{{}^{i}l_{\nu,k}u_{\nu}'}\right)\Bigg]K_i\left({}^{0}E_{\nu,k},\eta u_{\nu},\zeta u_{\nu}'\right)dz'du_{\nu}'\Bigg\},\qquad(2.32)$$

after some long but straightforward mathematical manipulation. Here, $\eta\equiv\pm1$, $\mu_3\equiv\mathrm{sgn}(\eta)$, ${}^{i}u_{\nu,k}^{\min}\equiv\min\left({}^{i}u_{\nu,k}^{+},{}^{i}u_{\nu,k}^{-}\right)$, and ζ, μ_1, μ_2, m have the same definitions as used in Eq. 2.31. For

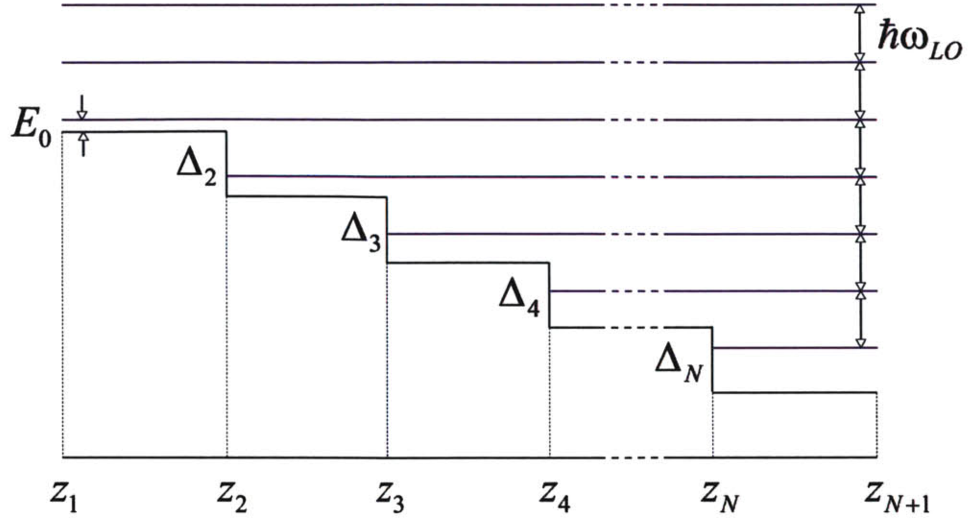

Figure 2-3: Conduction band of the base structure and energy grid for the solution of the BTE. The energy level E_0 in the first base step, where $0 \leq E_0 \leq \hbar\omega_{LO}$, defines a unique energy grid throughout the base with energy separation $\hbar\omega_{LO}$. The BTE can be solved independently for this energy grid.

the isotropic case where the approximations of Eq. 2.19 are used, Eqs. 2.31-2.32 are simplified. The substitutions $R_\nu^{(+)}\left(z, {}^0E_{\nu,k}, u_\nu\right) \rightarrow R_\nu\left(z, {}^0E_{\nu,k}\right)$, $R_\nu^{(-)}\left(z, {}^0E_{\nu,k}, u_\nu\right) \rightarrow R_\nu\left(z, {}^0E_{\nu,k}\right)$, and $K_i\left({}^0E_{\nu,k}, u_\nu, u'_\nu\right) \rightarrow A_i\left({}^0E_{\nu,k}\right)$ lead to Eqs. 3.14-3.15 of [29]. This is a good check for the validity of the general mathematical formalism.

The expressions of Eqs. 2.31-2.32 constitute the complete solution of the BTE. If $f_{\nu-1}^{(+)}$ at z_ν and $f_{\nu+1}^{(-)}$ at $z_{\nu+1}$ are known, the collision terms $R_\nu^{(\pm)}$ can be found from Eq. 2.32. The boundary conditions along with $R_\nu^{(\pm)}$ are sufficient to determine the distribution functions $f_\nu^{(\pm)}$ from Eq. 2.32. Consequently, solving for $R_\nu^{(\pm)}$ is the essential building block for the solution of the BTE. Close observation of the integral equation for $R_\nu^{(\pm)}$ reveals a specific coupling of energy levels across the base. Let us focus on the energy level E_0 of the first base step in Fig. 2-3, where $0 \leq E_0 \leq \hbar\omega_{LO}$. The conservation of total energy relates E_0 with the energy level $E_0 + \Delta_2 + ... + \Delta_\nu$ of the ν base step. In addition, each of these energy levels defines an energy grid in the base step ν with energy separation $\hbar\omega_{LO}$ due to LO phonon scattering. Therefore, if a finite number of phonon levels is chosen for the first base step, E_0 determines a finite set of energy levels throughout the base. For a given frequency and energy level E_0 of the first step, a fine grid of z and u_ν can transform Eq. 2.32 into a linear system of the form $\overline{\overline{A}}\boldsymbol{x} = \boldsymbol{b}$. In this linear system, $\boldsymbol{x}$ contains the unknown $R_\nu^{(\pm)}$, the boundary conditions are incorporated in $\boldsymbol{b}$, and $\overline{\overline{A}}$ includes the scattering kernels K_0, $K_{\pm 1}$. The solution $\boldsymbol{x} = \overline{\overline{A}}^{-1}\boldsymbol{b}$ is straightforward provided that $\overline{\overline{A}}$ is not prohibitively large.

The solution strategy is illustrated in Fig. 2-4. It consists of alternate forward and backward recursions across the base. The forward and backward recursions are depicted by the blue and red

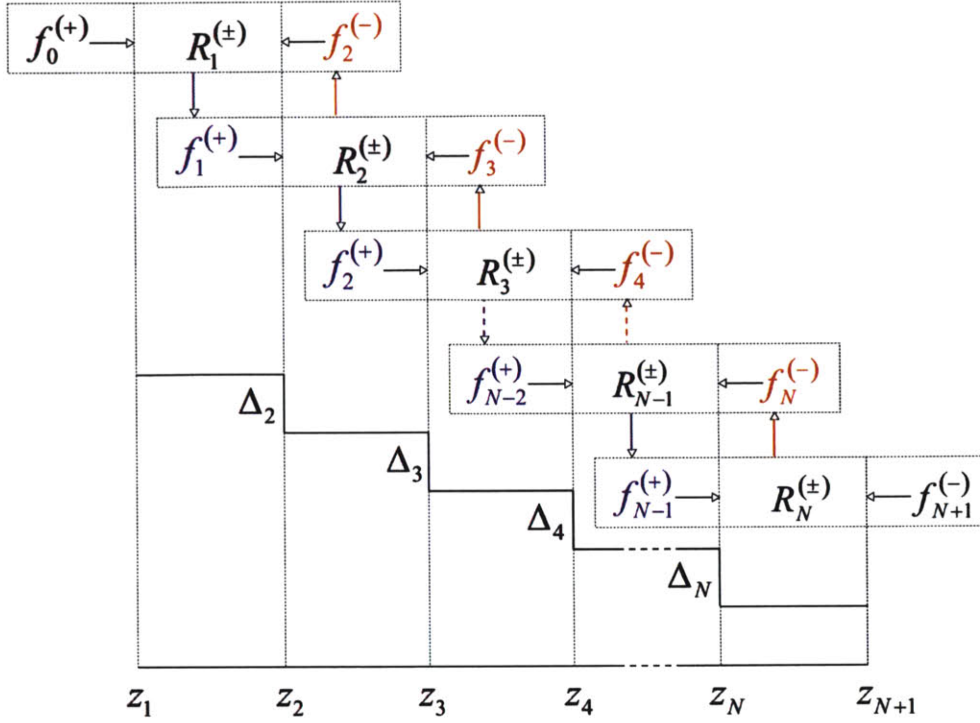

Figure 2-4: Solution scheme for the BTE in the base structure. The blue/red color indicates forward/backward recursion. During the forward/backward recursion, the values of $f_\nu^{(-)}/f_\nu^{(+)}$ at the endpoinds are known from the previous backward/forward recursion, and the values of $f_\nu^{(+)}/\ f_\nu^{(-)}$ at the endpoints are being updated. In the first recursion, the guess $f_\nu^{(-)} = 0$ at the endpoints is used. Convergence is achieved when the current converges at some monitor points.

arrows, respectively. In the first forward recursion, the guess $f_{\nu+1}^{(-)} = 0$ at $z_{\nu+1}$ for $\nu = 1, 2, ..., N-1$ is applied. It is a good estimate since a relatively large Δ allows limited back diffusion. The given $f_0^{(+)}$ at z_1 and the guess $f_2^{(-)}$ at z_2 are sufficient to determine $R_1^{(\pm)}$. Then, $f_1^{(+)}$ at z_2 is found from $R_1^{(\pm)}$. The forward recursion continues for all the base steps and estimates of $f_{\nu-1}^{(+)}$ at z_ν for $\nu = 2, 3, ..., N$ are calculated. After $R_N^{(\pm)}$ is found, a new estimate of $f_N^{(-)}$ is calculated. The backward recursion towards the first step takes place and the values of $f_{\nu+1}^{(-)}$ at $z_{\nu+1}$ for $\nu = 1, 2, ..., N-1$ are updated. The series of recursions ends when the computed current converges at some monitor points in the base. This process continues for a sufficient number of energy levels E_0 of the first base step, where $0 \leq E_0 \leq \hbar\omega_{LO}$. The convergence speed is enhanced significantly if the isotropic approach is adopted first. The resultant $R_\nu(z, E_\nu)$ and $f_{\nu+1}^{(-)}$ at $z_{\nu+1}$ for $\nu = 1, 2, ..., N$ serve as a first guess for the anisotropic case by making the substitution $R_\nu^{(+)} = R_\nu^{(-)} = R_\nu(z, E_\nu)$ on the right side of Eq. 2.32.

2.5 Simulation Results of the Intrinsic Operation

The intrinsic operation of the HBT can be fully described by the distribution functions $f_\nu^{(\pm)}$. The carrier concentration n_ν and the current density J_ν can be readily extracted. The former is the zero moment and the latter is the first moment of the distribution function in the base. More specifically, $n_\nu(z) = \left[2/(2\pi)^3\right] \int f_\nu(z, \boldsymbol{k})\, d\boldsymbol{k}$, and $J_\nu(z) = \left[2/(2\pi)^3\right] \int (\hbar k_z/m^*) f_\nu(z, \boldsymbol{k})\, d\boldsymbol{k}$. If the change of variables $\boldsymbol{k} \to (E_\nu, u_\nu)$ is applied for n_ν and J_ν, then the following expressions are derived:

$$n_\nu(z) = \frac{m^{*3/2}}{\sqrt{2}\pi^2\hbar^3} \int_0^\infty \sqrt{E_\nu} dE_\nu \int_0^1 \left[f_\nu^{(+)}(z, E_\nu, u_\nu) + f_\nu^{(-)}(z, E_\nu, u_\nu)\right] du_\nu, \tag{2.33}$$

$$J_\nu(z) = \frac{qm^*}{\pi^2\hbar^3} \int_0^\infty E_\nu dE_\nu \int_0^1 \left[f_\nu^{(+)}(z, E_\nu, u_\nu) - f_\nu^{(-)}(z, E_\nu, u_\nu)\right] u_\nu du_\nu. \tag{2.34}$$

The difference of signs in the distribution function arguments can be easily explained. The concentration is a scalar quantity and both $f_\nu^{(+)}$ and $f_\nu^{(-)}$ contribute additively. On the other hand, the current density is a vector quantity. Thus, the difference between forward and back diffusion contributes to the current density. The total base transport factor can be expressed as a current density ratio, namely, $\alpha_T \equiv J_N(z_{N+1})/J_1(z_1)$.

We implemented a MATLAB program according to the aforementioned BTE solution strategy. The base-emitter junction is considered smoothly alloy graded and the base-collector junction is a GaAs homojunction. The conduction band discontinuity Δ is the same for all the interior base step endpoints $z_2, z_3, ..., z_N$ and all the base steps have the same thickness X_{step}. A single effective mass was used across the base, namely $m^* = m^*(x_{av})$, where x_{av} is the average Al concentration in the base. Both the Maxwell distribution of the injected electrons at the first step and the Bose-Einstein distribution of phonons in the base are considered at T=300 K. The impurity scattering was treated isotropic. This is a satisfactory approximation for a heavily doped base ($N_B > 10^{19}$ cm^{-3}). Furthermore, we used for simplicity an energy independent impurity scattering length l_{imp}. The incorporation of complex scattering mechanisms due to heavy doping, such as electron-electron scattering and plasmon screening, would add significant complexity. The frequency points were taken in increments of 20 GHz. For the frequencies inbetween, we used cubic spline interpolation.

The solution of the collision terms $R_\nu^{(+)}$ and $R_\nu^{(-)}$ in Eq. 2.32 requires a fine grid of z, u_ν, and $E_{\nu,k}$. The angle variable u_ν stems from the anisotropic nature of LO phonon scattering. The convergence criterion is met after many forward and backward recursions and the BTE solutions call for significant computational time. A solution to accelerate the complex calculations is to adopt the isotropic approach of the LO phonon scattering. The u_ν-dependence of the collision terms is lifted and sizes of the matrices involved are reduced significantly. Such an approximation can not be followed if the accuracy is seriously compomised. We performed a comparison between the anisotropic and isotropic model on a base structure with N=2. The base tranport factors of these

Table 2.1: Comparison of base transport factor for isotropic and anisotropic model. The structure has N=2, X_{step}=500 Å, l_{imp}=200 Å, Δ =1.2 $\hbar\omega_{LO}$.

Frequency (GHz)	$\lvert\alpha_{T,isotr}\rvert$	$\angle\alpha_{T,isotr}$ (deg)	$\lvert\alpha_{T,anisotr}\rvert$	$\angle\alpha_{T,anisotr}$ (deg)
100	0.76	-58	0.78	-54
200	0.47	-95	0.50	-90
300	0.30	-120	0.33	-113

two cases are summarized in Table 2.1. The magnitude attenuation and the phase delay are larger in the isotropic model by less than 10%. The base transport factor polar traces of the two models almost coincide, with the only difference that the isotropic model predicts a lower frequency for approximately the same α_T. The static carrier concentrations of minority carriers of the two models are almost identical. Therefore, the isotropic model proved to be sufficiently accurate. This simple model was used for all the simulation results that follow. We will investigate the effect of N, X_{step}, l_{imp}, and Δ on the base transport factor. In this way, the design choices can be decided with confidence. The LO phonon scattering mechanism will be revealed by studying the distrubution of current density and the concentration/velocity profiles.

We studied the effect of variable number of steps for a constant total base thickness. The results for N=1, 2, 5 and $N \times X_{step}$=1000 Å are shown in Fig. 2-5(a). The magnitude attenuation and the phase delay of α_T decrease with the introduction of steps. The forward diffusion of carriers is enhanced. In addition, the negative real axis is crossed at higher frequencies and larger $|\alpha_T|$. This is instrumental for high frequency transit-time oscillations. For $N > 5$, the changes of the α_T loci become minimal. This is to be expected since the base step becomes less than the LO phonon scattering lenth l_{op}. The exchange of energy between the hot electrons and the lattice is not sufficient. A rough estimate of the LO scattering length can be calculated by $l_{op} \approx v_{op}\tau_{op} = \left(2\hbar\omega_{LO}/m^*\right)^{1/2}\tau_{op}$. In GaAs, $\hbar\omega_{LO} = 36.2$ meV, $m^* = 0.068m_0$, $\tau_{op} \approx 0.1$ ps, and $l_{op} \approx 430$ Å. The maximum available number of steps is determined by the maximum available energy gap in the base. The suppression of the base hole current holes requires a satisfactory energy gap difference between the emitter and the base. Let us assume that the Al concentration in the emitter and the first base step is x_E=0.35 and $x_{B,max}$=0.2, respectively. Then, $N_{\max} \approx 1 + \left[\Delta E_g\left(x_{B,\max}\right)/\Delta\right] \approx 7$ for $\Delta = 1.2\ \hbar\omega_{LO}$.

Let us define $\alpha_i \equiv J_i\left(z_{i+1}\right)/J_i\left(z_i\right)$ the transport factor of the i base step . The various simulated α_i are illustrated in Fig. 2-5(b) for N=5. We can clearly notice that α_i belongs to one of three families of curves, the first step, the last step, and the rest. The boundary conditions for z_1 and z_{N+1} differentiate α_1 and α_N from the rest. Furthermore, the back diffusion in the first step differs from the rest of the steps since there is no there is no energy gap discontinuty at z_1. The total base transport factor is given by $\alpha_T = \alpha_1\alpha_2\prod_{i=2}^{N-1}\alpha_i$. The base step transport factors of the inner steps appear similar. Therefore, the approximation $\prod_{i=2}^{N-1}\alpha_i \approx \alpha_m^{N-2}$, where $2 \leq m \leq N-1$, is

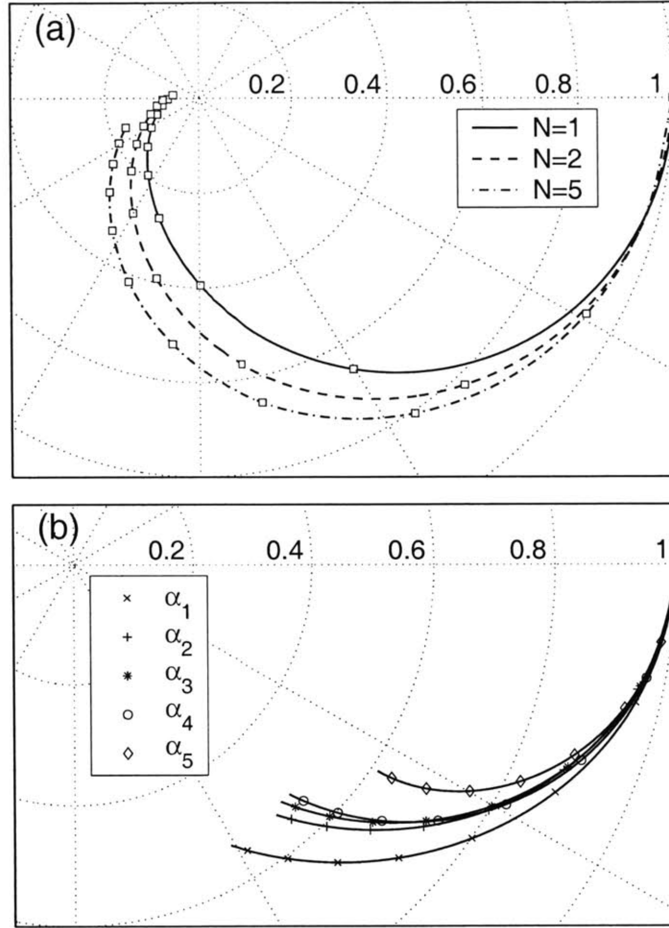

Figure 2-5: (a) Polar graph of α_T for $N \times X_{step}$=1000 Å, l_{imp}=300 Å, and Δ=1.2 $\hbar\omega_{LO}$ (marker every 100 GHz, frequency range 0-1 THz). As the number of steps increases (N=1, 2, 5), $|\alpha_T|$ increases and $|\angle\alpha_T|$ decreases resulting in a higher frequency performance. (b) Polar graph of the base step transport factor for N=5, X_{step}=500 Å, l_{imp}=300 Å, and Δ=1.2 $\hbar\omega_{LO}$ (marker every 40 GHz, frequency range 0-300 GHz). The base step transport factors are grouped in three families of curves, the first $\{\alpha_1\}$, the middle $\{\alpha_2, \alpha_3, \alpha_4\}$, and the last $\{\alpha_5\}$.

justified. This must be contrasted with the appoximate approach of [24] where $\alpha_T = \alpha_1^N$ is assumed. The simulations indicate that the idea of cascading the base step transport factor is valid only for the middle steps. Let us assume that we add r base steps to the existant base structure. The simulation results will be effectively the same with the addition of r base step transport factors in the middle family. Furthermore, α_T crosses the negative real axis at lower frequencies and larger $|\alpha_T|$ facilitating transit-time oscillations.

The case of variable X_{step} is studied in Fig. 2-6(a). As the base step thickness increases for the same N, α_T undergoes more magnitude attenuation and phase delay. In addition, α_T crosses the negative real axis at lower frequencies and larger $|\alpha_T|$ which is advantageous for transit-time oscillations. Let us examine two different base step thicknesses, $X_{step,1}$ and $X_{step,2}$. According to

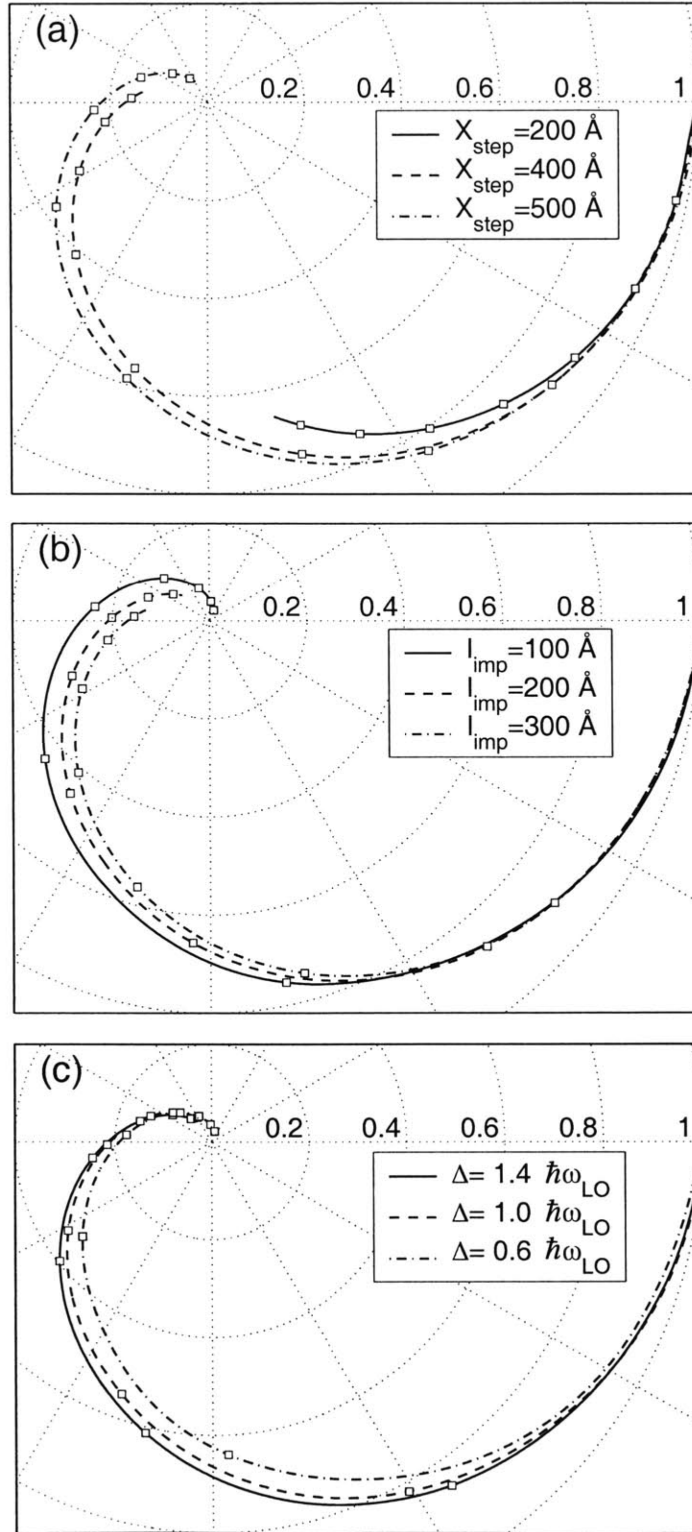

Figure 2-6: Polar graph of α_T for (a) N=5, l_{imp}=300 Å, Δ=1.2 $\hbar\omega_{LO}$, and variable X_{step}, (b) N=5, X_{step}=400 Å, Δ=1.2 $\hbar\omega_{LO}$, and variable l_{imp}, and (c) N=5, X_{step}=500 Å, l_{imp}=300 Å, and variable Δ. In (a)-(c), the frequency range is 0-300 GHz and every marker corresponds to 40 GHz increment.

the approximate approach of [24], $\alpha_{T,1}(\omega_1) \approx \alpha_{T,2}(\omega_2)$ when $\omega_1/\omega_2 \approx (X_{step,2}/X_{step,1})^2$. This can be approximately verified for the low frequency range.

The base of the HBT is usually heavily doped for low base resistance. As the doping level increases, l_{imp} decreases. As Fig. 2-6(b) suggests, a lower l_{imp} causes more magnitude attenuation and phase delay of α_T. This can be easily explained since the smaller/larger l_{imp} is compared to the base step, the more diffusive/ballistic the transport becomes. According to the qualitative approach of [24], the diffusion constant D_n decreases as l_{imp} decreases, resulting in larger magnitude attenuation and phase delay. Let us consider the case of two different impurity lengths, namely $l_{imp,1}$ and $l_{imp,2}$. According to the diffusion approach, the loci of $\alpha_{T,1}$ and $\alpha_{T,2}$ must coincide. This is verified in the low frequency range. From experimental data in [33] for p-type GaAs with $N_B \approx 10^{19}$ cm^{-3}, the mobility of minority carriers is measured to be $\mu_n \approx 1000$ cm^{2}V^{-1}s^{-1}. Then, from the Einstein relation $D_n/\mu_n = k_BT/q$, we estimate that $D_n \approx 26$ cm^{2}s^{-1}. In the diffusion limit, the diffusion constant D_n is associated with the scattering length l_{sc} by the relation $D_n = [8k_BT/(9\pi m^*)]^{1/2} l_{sc}$. For the given value of D_n, we estimate $l_{sc} \approx 190$ Å. Consequently, if we assume $l_{op} \approx 400$ Å, then from $l_{sc}^{-1} \approx l_{imp}^{-1} + l_{op}^{-1}$ we conclude that $l_{imp} \approx 360$ Å. However, these results are valid in the diffusion approximation and also $Al_xGa_{1-x}As$is expected to have lower mobility values. In addition, during the MBE growth there is always a margin of error for the doping level in the base. For all these reasons, we chose the range of values l_{imp}=100, 200, and 300 Å in Fig. 2-6(b).

We investigated the effect of Δ on the base transport factor. The simulations results in Fig. 2-6(c) show that as Δ increases, the magnitude attenuation and phase delay of α_T decrease. The polar traces do not change substantially for $\Delta > \hbar\omega_{LO}$. These results can be interpreted qualitatively. The discontinuity Δ in the conduction band acts as a barrier against back diffusion. At the same time, it is a launching pad for highly energetic electrons. Therefore, a high Δ favors the forward diffusion of minority carriers. LO phonon emission takes place when $\Delta \geq \hbar\omega_{LO}$. Consequently, for values of Δ higher than $\hbar\omega_{LO}$, the improvement of the base transport factor is minimal.

The normalized current density distribution ρ_J unveils the details of the scattering mechanisms affecting the transport of minority carriers in the base. It is defined from the relation $J_\nu(z)/J_{th} = \int_0^\infty \rho_J(E,z)\, E dE$, where $J_{th} \equiv n_e q v_{th}/2$, and $v_{th} \equiv \sqrt{2k_BT/(\pi m^*)}$ is the thermal velocity. From Eq. 2.34, it becomes evident that ρ_J reflects the net transport given by the difference $f_\nu^{(+)} - f_\nu^{(-)}$. We examined the case of a base structure with N=5. The simulated ρ_J of the first, second, and third step are illustrated in Fig. 2-7. The current density distribution in the first step follows a Maxwellian form as a result of the boundary condition at z_1. The current density distribution at the starting point of the second and third step is zero for $E < \Delta$. At points farther in the base step, LO phonon scattering cools down the nonequilibrium distribution by exchanging electron energy with the lattice. The elastic mechanism of impurity scattering randomizes the energy content of the

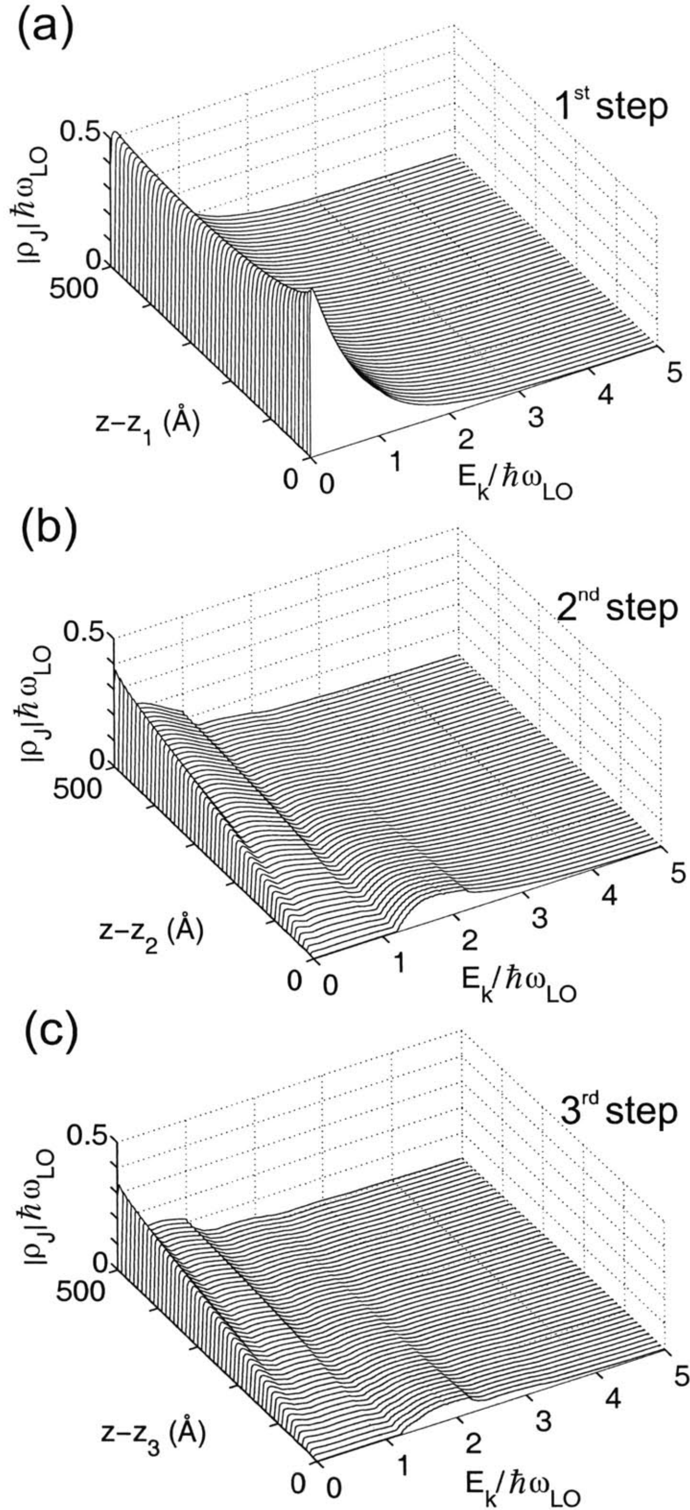

Figure 2-7: Magnitude of the normalized current density distribution $|\rho_J|$ for N=5, X_{step}=500 Å, l_{imp}=300 Å, and Δ=1.2 $\hbar\omega_{LO}$ (Frequency=100 GHz). In (a), (b), and (c), the 1st, 2nd, and 3rd base step is considered respectively. The distribution has a Maxwellian form in the first step. LO phonon scattering effects are clearly shown in the $|\rho_J| - E_k$ profile. The carriers are hotter for base steps closer to the collector side.

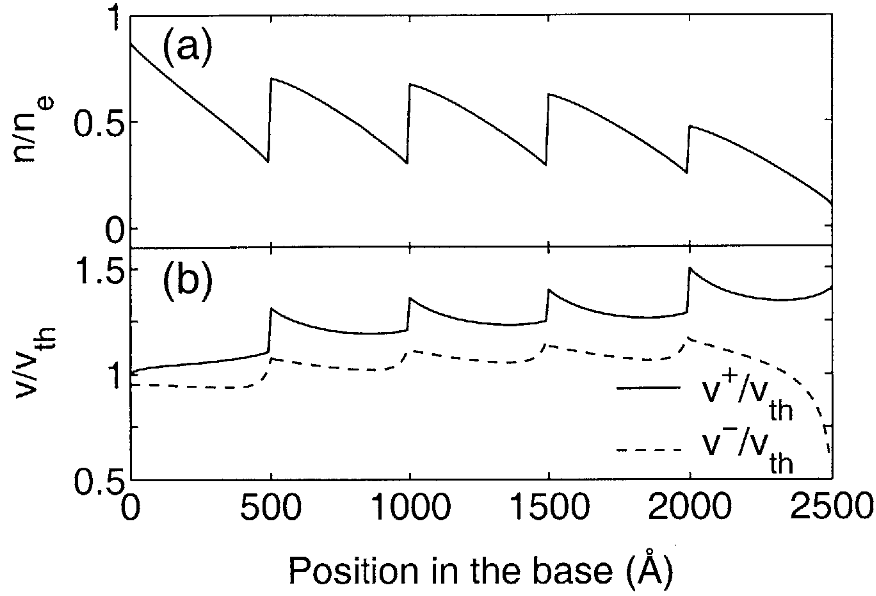

Figure 2-8: (a) Normalized minority carrier concentration n/n_e and (b) normalized forward velocity v^+/v_{th} and backward velocity v^-/v_{th} across the base for N=5, X_{step}=500 Å, l_{imp}=300 Å, and Δ=1.2 $\hbar\omega_{LO}$ (static case). The profiles of n/n_e, v^+/v_{th}, and v^-/v_{th} are nearly periodic in the middle steps. In (a), the effective diffusivity becomes larger near the collector side. In (b), v^+/v_{th} increases near the collector as the minority carriers become hotter.

minority carriers forming a Maxwell distribution of a temperature defined by the non-elastic process. In the third step, the current density distribution is wider in energy due to insufficient colling from the previous steps.

We studied the minority carrier concentration and the velocity profile for the static case of a base structure with N=5. The forward velocity and backward velocity, v^+ and v^-, respectively, are defined as $v^\pm \equiv J^\pm/(n^\pm q)$. The signs (+) and (−) of both the current density and the carrier concentration refer to the components containing the $f^{(+)}$ and $f^{(-)}$ distributions, respectively, in Eqs. 2.33-2.34. The carrier concentration in Fig. 2-8(a) is almost periodic for the middle steps and distinctly different for the first and last step. This can be easily explained from the perspective of the base step transport factors α_i in Fig. 2-5(b). In addition, the slope of n/n_e decreases towards the collector. This observation suggests that the minority carriers are more energetic as they approach the collector. Here, it is worthwhile to mention the results of [27], where the concentration of minority carriers appears more uniform across the base as the tranport becomes more ballistic. The forward valocity in Fig. 2-8(b) is equal to the thermal velocity at the beginning of the first step in accordance with [30]. This is the result of the imposed Maxwell distribution at z_1. The backward velocity is zero at the end of the last step as expected from the boundary condition of vanishing $f^{(-)}_{N+1}$ at z_{N+1}. We can also notice the periodicity of the middle steps. The velocity profile indicates

that the carriers become hotter as they move towards the collector as a result of the insufficient cooling of LO phonon scattering.

2.6 Intrinsic HBT circuit

The intrinsic part of the device is bounded vertically by the the beginning of the depletion region in the emitter and the end of the depletion region of the collector and horizontally by the emitter area. The intrinsic operation of the three-terminal device can be accurately described by the common-base y parameters. Both the electron current and the displacement current have to be included in the small signal representation. In what follows, the formalism of [34] is adopted.

Let $\hat{i}_{n,e'}$ denote the electron current exiting the space-charge region of the base-emitter junction. Then, $\hat{i}_{n,e'} = A_e J_1(z_1) \equiv g_e \hat{v}_{eb}$, where A_e is the intrinsic surface perpendicular to the carrier transport, and $J_1(z_1)$ can be computed from Eq. 2.34. The $\hat{v}_{eb}$-dependence of $J_1(z_1)$ is implicit in the expression of $f_0^{(+)}$ at z_1 since the factor n_e/N_C in Eq. 2.29 scales linearly the solution of the BTE. Let $\hat{i}_{n,c'}$ denote the electron current exiting the quasi-neutral base. From the definition of the base transport factor, it is clear that $\hat{i}_{n,c'} = -\alpha_T \hat{i}_{n,e'} = -\alpha_T g_e \hat{v}_{eb}$. The minus sign is used because we consider the direction of a terminal current as positive when it enters the terminal.

The continuity of current implies that the current collected at the collector terminal $\hat{i}_c$ is equal to the sum of the electron current $\hat{i}_{n,c}$ and the displacement current at any cross section of the depleted collector. Specifically, $\hat{i}_c = \hat{i}_{n,c}(z) + jA_e\omega\varepsilon\hat{E}(z)$, where $\hat{E}(z)$ is the small signal electric field in the space charge region. Both the electric field and the electron current are position-dependent whereas the total current is constant. If we assume that the electrons move with the saturation velocity v_s in the depleted collector, then the electron concentration is $\hat{n}(z) = \hat{n}(z_{N+1})\exp[-j\omega(z - z_{N+1})/v_s]$, or equivalently $\hat{i}_{n,c}(z) = \hat{i}_{n,c'}\exp[-j\omega(z - z_{N+1})/v_s]$. If we integrate across the thickness of the space charge region, we arrive at the complete expression of the collector current:

$$\hat{i}_c = -g_e \alpha_T \alpha_C \hat{v}_{eb} + j\omega C_{jCi}\hat{v}_{cb}, \tag{2.35}$$

where $\alpha_C \equiv \exp(-j\omega\tau_C/2)[\sin(j\omega\tau_C/2)/(\omega\tau_C/2)]$ is the collector transport factor, $\tau_C \equiv X_{dep,C}/v_s$ is the transit time in the collector, $X_{dep,C}$ is the thickness of the space charge region, and C_{jCi} is the intrinsic capacitance of the base-collector junction.

A similar analysis can be adopted for the total emitter current $\hat{i}_e$ entering the space charge region of the base-emitter junction. However, the emitter-base junction is forward biased and the transit time $\tau_E \equiv X_{dep,E}/v_s$, where $X_{dep,E}$ is the space charge region thickness, is expected to be very small. Therefore, $\exp(-j\omega\tau_E/2)[\sin(j\omega\tau_E/2)/(\omega\tau_E/2)] \to 1$, and the total emitter current is given by

$$\hat{i}_e = (g_e + j\omega C_{jE})\hat{v}_{eb}, \tag{2.36}$$

where C_{jE} is the intrinsic capacitance of the emitter-base junction.

From the definition of small signal y-parameters of a three-terminal device and Eqs. 2.35-2.36, it follows that the common-base y-parameters of the device can be written as

$$\begin{bmatrix} y_{11}^{b,i} & y_{12}^{b,i} \\ y_{21}^{b,i} & y_{22}^{b,i} \end{bmatrix} = \begin{bmatrix} g_e + j\omega C_{jE} & 0 \\ -g_e \alpha_T \alpha_C & j\omega C_{jCi} \end{bmatrix}, \tag{2.37}$$

where the subscripts 1 and 2 denote the emitter and collector terminal, respectively, and the superscripts b and i denote common-base configuration and intrinsic operation, respectively. In the derivation above, we have not taken into account the Early effect since we expect that the modulation of the base width induced by $\hat{v}_{cb}$ will be limited due to the heavy base doping.

It is enlightening to juxtapose the small signal parameters of our device with the small signal parameters of a HBT with uniform base in the diffusion approximation. If we follow the same steps and use the approximate expressions of the static and high frequency current of Eqs. 2.6-2.7, we obtain the common-base parameters of a HBT with uniform base:

$$\begin{bmatrix} y_{11}^{b,i} & y_{12}^{b,i} \\ y_{21}^{b,i} & y_{22}^{b,i} \end{bmatrix} = \begin{bmatrix} \left(\bar{I}_E/V_{th}\right) X_B \zeta \coth\left(\zeta X_B\right) + j\omega C_{jE} & 0 \\ -\left(\bar{I}_E/V_{th}\right) X_B \zeta \operatorname{csch}\left(\zeta X_B\right) \alpha_C & j\omega C_{jCi} \end{bmatrix}. \tag{2.38}$$

In the low frequency region, the approximations $\alpha_C \approx 1 - j\omega\tau_c/2$, $\zeta X_B \coth\left(\zeta X_B\right) \approx 1 + j\omega X_B^2/(3D_n)$, and $\zeta X_B \operatorname{csch}\left(\zeta X_B\right) \approx 1 - j\omega X_B^2/(6D_n)$ are accurate to some degree. Then, the approximate expressions of the common-base y-parameters become

$$\begin{bmatrix} y_{11}^{b,i} & y_{12}^{b,i} \\ y_{21}^{b,i} & y_{22}^{b,i} \end{bmatrix} \approx \begin{bmatrix} g_E + j\omega\left(C_D + C_{jE}\right) & 0 \\ -\left(g_E - j\omega C_D/2\right)\left(1 - j\omega\tau_C/2\right) & j\omega C_{jCi} \end{bmatrix}, \tag{2.39}$$

where $g_E \equiv \bar{I}_E/V_{Th}$ is the dc conductance, and $C_D \equiv g_E X_B^2/(3D_n)$ is the diffusion capacitance. Therefore, from Eqs. 2.37-2.39, the term g_e of our device corresponds, in the diffusion approximation, to the dc emitter conductance g_E in parallel with the diffusion capacitance C_D. The more complex form of g_e reflects the fact that the LO phonon mechanism is not a perfect sink and the more involved approach of the BTE is required. The same argument holds for the base transport factor of our device compared to the simple form of α_T in Eq. 2.8 for the case of a HBT with uniform base.

Another important intrinsic element of the HBT of this work is the intrinsic tranverse base resistance Z_{bi}. To a first approximation, we can assume that the intrinsic operation described so far, is not affected by Z_{bi}. The intrinsic transverse base resistance is simply connected to the intrinsic base terminal. Therefore, Z_{bi} can be treated as an extrinsic element although, strictly speaking, it is part of the intrinsic device.

2.7 Extrinsic HBT circuit

A HBT double mesa, emitter-up configuration is illustrated in Fig. 2-9(a). It consists of the emitter cap, the emitter, the base, the collector, and the subcollector. The emitter cap and the subcollector

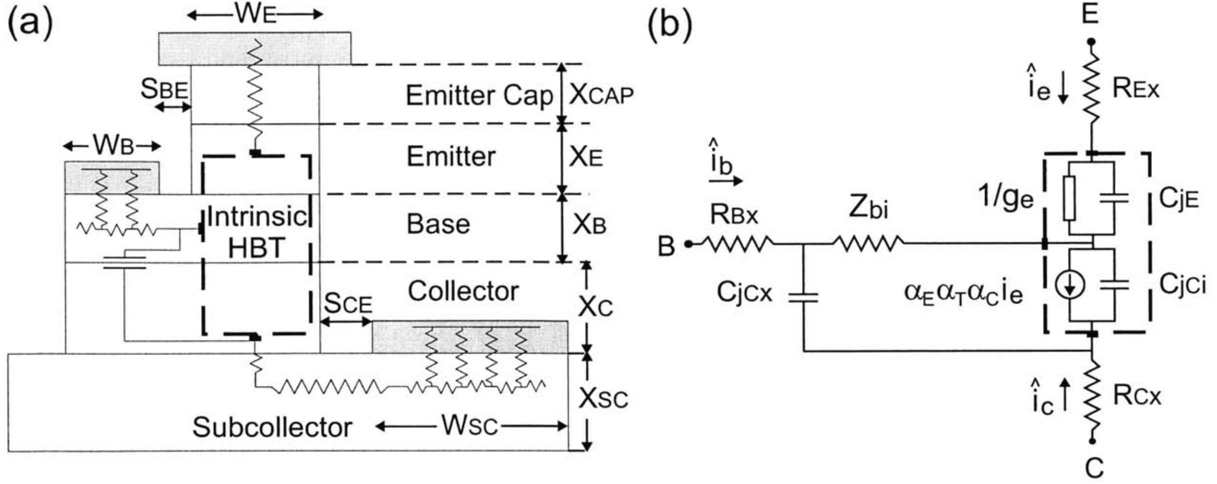

Figure 2-9: (a) Schematic of an emitter-up HBT configuration, and (b) the equivalent circuit including intrinsic and extrinsic elements. The dashed lines in (a) and (b) indicate the intrinsic part of the device. The length of the device not shown in (a), is L_E.

are heavily n-doped layers that facilitate the ohmic contacts on the lightly doped emitter and collector respectively. The intrinsic part of the device is included in the dashed rectangle. The rest of the device represents the extrinsic circuit.

The equivalent small signal circuit is shown in Fig. 2-9(b). The term α_E in the expression of the current controlled current source is the emitter transport factor, $\alpha_E \equiv g_e/(g_e + j\omega C_{jE})$. The extrinsic elements can be readily extracted [35]. Let ρ_{cap}, ρ_e, ρ_b, ρ_c, ρ_{sc} be the bulk resistivity $(\Omega \cdot \mathrm{cm})$ of the emitter cap, the emitter, the base, the collector, and subcollector respectively. Let also $\rho_{cap,c}$, $\rho_{b,c}$, $\rho_{sc,c}$ be the spesific contact resistance $(\Omega \cdot \mathrm{cm}^2)$ of the emitter cap, the base, and the subcollector respectively. The various vertical and horizontal dimensions are noted in Fig. 2-9(a) and the length of the HBT is L_E. The depleted emitter thickness is $X_{dep,E}$ and the depleted collector thickness is $X_{dep,C}$. The base and subcollector sheet resistance (Ω/sq) is defined as $R_{b,s} \equiv \rho_b/X_B$ and $R_{sc,s} \equiv \rho_{sc}/X_{SC}$, respectively.

The derivation of the intrinsic base resistance Z_{bi} stems from the distributive nature of the base current. According to [35], the small signal base current is given by

$$\hat{i}_b(x) = \hat{i}_b(0) \sinh\left[\varepsilon\left(W_E - x\right)\right] \sinh\left(\varepsilon W_E\right)^{-1}, \tag{2.40}$$

where $0 \leq x \leq W_E$, $\varepsilon \equiv \left[\rho_b \Sigma_y^{b,i}/(W_E L_E X_B)\right]^{1/2}$, and $\Sigma_y^{b,i} \equiv y_{11}^{b,i} + y_{12}^{b,i} + y_{21}^{b,i} + y_{22}^{b,i}$. The transverse base resistance is defined as the ratio of the average potential difference between the base and emitter over the base current. Simple mathematical treatment yields

$$Z_{bi} = \left(\frac{\rho_b W_E}{X_B L_E}\right) \frac{\coth\left(\varepsilon W_E\right)}{\varepsilon W_E} - \frac{1}{\Sigma_y^{b,i}}. \tag{2.41}$$

In the low frequency limit, Eq. 2.41 simplifies to $Z_{bi} \approx [\rho_b W_E/(X_B L_E)]/3$. This is one third of the value that we would expect if the base current was uniform.

The extrinsic resistance R_{Ex} accounts for the ohmic contact of the emitter and the resistance of the emitter cap and the undepleted emitter. It can be easily expressed as

$$R_{Ex} = \frac{\rho_{cap,c} + \rho_{cap} X_{cap} + \rho_e (X_E - X_{dep,E})}{W_E L_E}. \tag{2.42}$$

The extrinsic base resistance consists of the extrinsic transverse resistance along S_{BE} and the distributed resistance between the base ohmic contact and the base layer. The latter can be easily expressed as an open-ended lossy transmission line of length W_B. The differential resistance dR along W_B is $(R_{b,s}/L_E)\,dl$ and the differential conductance dG along X_B is $(L_E/\rho_{b,c})\,dl$, where dl is the differential length along W_B. We can compute this distributed resistance as the impedance seen from the edge of the base ohmic contact which is closer to the emitter. The characteristic impedance of a transmission line is given by $Z_0 \equiv \sqrt{(j\omega dL + dR)/(j\omega dC + dG)}$. The characteristic impedance of the transmission line along W_B for $dL = 0$ and $dC = 0$ is $Z_0 = \sqrt{dR/dG} = \sqrt{\rho_{b,c} R_{b,s}}/L_E$. The propagation constant of the lossy line is $\gamma = \sqrt{(dR/dl)\,(dG/dl)} = \sqrt{R_{b,s}/\rho_{b,c}}$. The reflection coefficient of the open-ended line seen from the base ohmic contact edge closer to the emitter is $\rho_L = \exp(-2\gamma W_B)$. Therefore, the distributed resistance we wish to calculate is given by $Z_{in} = Z_0(1-\rho_L)/(1+\rho_L)$. If we use the previously derived expressions of Z_0, ρ_L, and γ, we arrive at the result $Z_{in} = \left(\sqrt{\rho_{b,c} R_{b,s}}/L_E\right) \coth\left(W_B \sqrt{R_{b,s}/\rho_{b,c}}\right)$. Thus, the total extrinsic base resistance can be expressed as

$$R_{Bx} = \frac{\sqrt{\rho_{b,c} R_{b,s}}}{L_E} \coth\left(W_B \sqrt{R_{b,s}/\rho_{b,c}}\right) + \frac{R_{b,s} S_{BE}}{L_E}. \tag{2.43}$$

The quantity $L_{B,T} \equiv \sqrt{\rho_{b,c}/R_{b,s}}$ is often referred to as the base transfer length and usually $L_{B,T} << W_B$. Therefore, $\coth(W_B/L_{B,T}) \to 1$, and Eq. 2.43 can be simplified accordingly.

The subcollector resistance consists of the distributed resistance between the subcollector ohmic contact and the subcollector, the extrinsic transverse resistance along S_{CE}, the spreading resistance along W_E, and the resistance of the undepleted collector. The spreading resistance along S_{CE} is very similar to the transverse base resistance Z_{bi}. Modeling the undepleted collector as a resistor is justified for certain collector doping levels and thicknesses. The average scattering time τ_{sc} of majority carriers in the undepleted collector can be found from the relation $\tau_{sc} = \mu_e m^*/q$, and the mean free path can be estimated by $l_{sc} \approx v_{th}\tau_{sc}$, where $v_{th} \equiv \sqrt{8k_BT/(\pi m^*)}$ is the thermal velocity of electrons ($v_{th} \approx 4.1 \times 10^7$ cm/s in GaAs at T=300 K). For a doping level $N_C = 3 \times 10^{16}$ cm^{-3}, the electron mobility is $\mu_n \approx 5500$ cm^{2}V^{-1}s^{-1}. The mean free path is calculated to be $l_{sc} \approx 870$ Å. The electrons exit the space charge region with a saturated velocity $v_{sat} \approx 8 \times 10^6$ cm/s. The strong electric field that sustained the high velocity of electrons in the space charge region is no longer present in the quasi-neutral collector, and scattering effects will be present within a few l_{sc}. We can

model the undepleted collector as a resistor if the thickness $X_C - X_{dep,C}$ is a few l_{sc}. Otherwise, if $X_C - X_{dep,C} \approx l_{sc}$, the resistor approximation fails and quasi-ballistic arguments have to be applied. For our HBTs, X_C is in the 6000-9000 Å range. A small V_{CB} voltage leaves a few thousand Å of undepleted collector and the resistor approximation is satisfactory. As we shall see, transit-time oscillations require low values of C_{jCi}. This can be accomplished by a large $X_{dep,C}$. Therefore, the design rule $X_C = X_{dep,C}$ will be applied, and in this case there is no resistance associated with the collector region. The total extrinsic collector resistance can be expressed as

$$R_{Cx} = \frac{\sqrt{\rho_{sc,c} R_{sc,s}}}{L_E} \coth\left(W_{SC}\sqrt{R_{sc,s}/\rho_{sc,c}}\right) + \frac{R_{c,s} S_{CE}}{L_E} + \frac{1}{3}\frac{\rho_{sc} W_E}{X_{SC} L_E} + \frac{\rho_c \left(X_C - X_{dep,C}\right)}{W_E L_E}. \quad (2.44)$$

We define as $L_{SC,T} \equiv \sqrt{\rho_{sc,c}/R_{sc,s}}$ the subcollector transfer length. For $L_{SC,T} \ll W_{SC}$, Eq. 2.44 simplifies by incorporating the limit $\coth\left(W_{SC}/L_{SC,T}\right) \to 1$. Finally, the extrinsic base-collector overlap defines the extrinsic base-collector capacitance

$$C_{jCx} = \varepsilon_C \frac{W_B + S_{BE}}{X_{dep,C}}. \quad (2.45)$$

2.8 Small Signal Parameter Formulation

The intrisnic Z_{bi} and the extrinsic elements R_{Ex}, R_{Bx}, R_{Cx}, and C_{jCx} complicate slightly the derivation of the HBT small signal parameters. Following the approach of [36], the circuit evolves in four stages illustrated in Fig. 2-10. The circuit complexity is minimized if we alternate between the common-base parameters of Fig. 2-10(a),(b) and the common-emitter parameters of Fig. 2-10(c),(d). From basic circuit analysis, z-parameters are useful when an element is added in series with a port and y-parameters are preferred when an element is in parallel with two ports. The relation between a y-parameter matrix and a z-parameter matrix of the same two-port circuit is $\overline{\overline{Z}} = \overline{\overline{Y}}^{-1}$. In the derivation that follows, port (2) is always assumed as the collector terminal, superscripts b, e, and i refer to common base, common emitter, and intrinsic configuration. The common-base y-parameter matrix $\overline{\overline{Y}}^{b,i}$ of the intrinsic device excluding Z_{bi} has already been extracted from the detailed analysis of transport. After the transformation $\overline{\overline{Y}}^{b,i} \to \overline{\overline{Z}}^{b,i}$ and the application of Kirchoff's voltage law, the intrinsic resistance Z_{bi} can be readily incorporated into the two-port circuit of Fig. 2-10(b) and the resultant z-parameter matrix $\overline{\overline{Z}}^{b,i}(Z_{bi})$ can be expressed as

$$\overline{\overline{Z}}^{b,i}(Z_{bi}) = \overline{\overline{Z}}^{b,i} + \begin{bmatrix} Z_{bi} & Z_{bi} \\ Z_{bi} & Z_{bi} \end{bmatrix} \quad (2.46)$$

The addition of the extrinsic capacitance C_{jCx} in Fig. 2-10(c) requires the transformation $\overline{\overline{Z}}^{b,i}(Z_{bi}) \to \overline{\overline{Y}}^{e,i}(Z_{bi})$, where $\overline{\overline{Y}}^{e,i}(Z_{bi})$ is the common-emitter y-parameter matrix of Fig. 2-10(b). In general, the transformation $\overline{\overline{Z}}^{b} \to \overline{\overline{Y}}^{e}$ of a transistor can be easily performed by simple circuit arguments

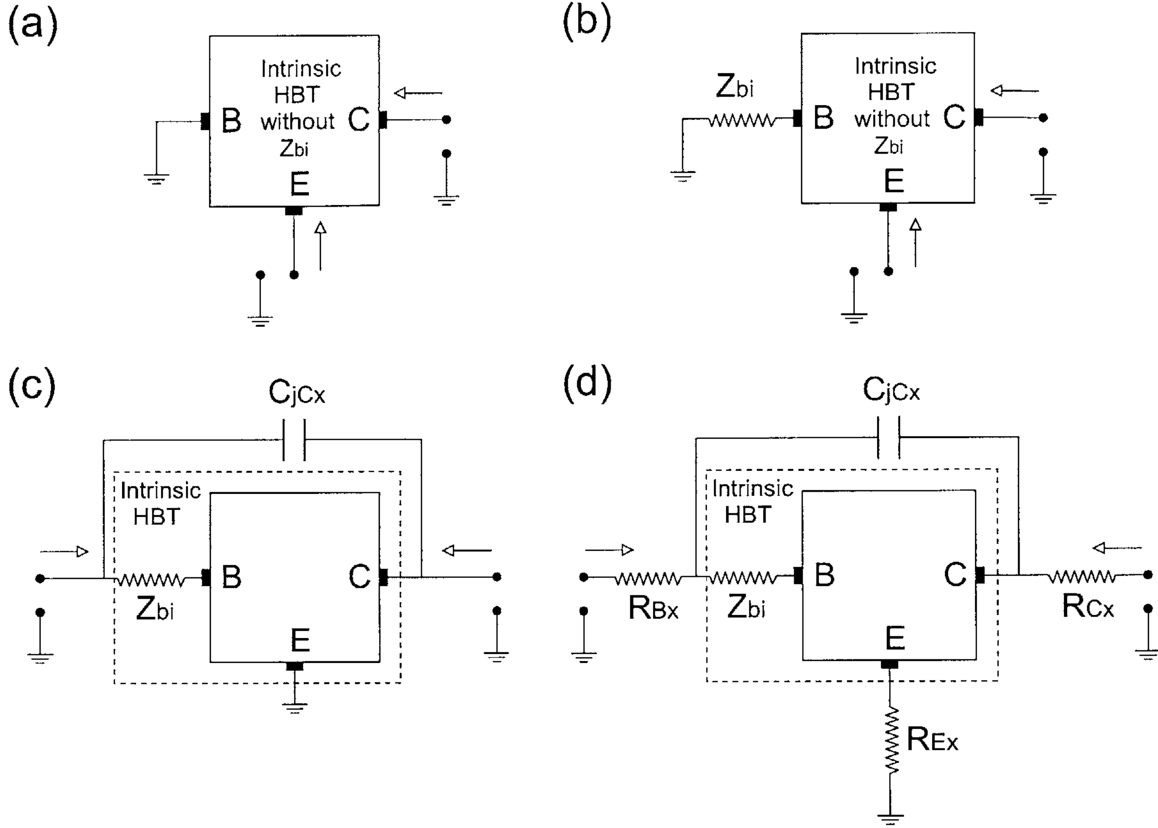

Figure 2-10: Circuit evolution of the HBT for the calculation of small signal parameters. The common-base configurations (a) and (b) develop into more complex common-emitter configurations (c) and (d) with the addition of the extrinsic elements C_{jCx}, R_{Ex}, R_{Bx}, and R_{Cx}.

and it is given by

$$\overline{\overline{Y}}^e = \frac{1}{z_{11}^b z_{22}^b - z_{12}^b z_{21}^b} \begin{bmatrix} z_{11}^b + z_{22}^b - z_{12}^b - z_{21}^b & z_{12}^b - z_{11}^b \\ z_{21}^b - z_{11}^b & z_{11}^b \end{bmatrix} \tag{2.47}$$

A straightforward application of Kirchoff's current law leads to the common-emitter y-parameter matrix

$$\overline{\overline{Y}}^e (Z_{bi}, C_{jCx}) = \overline{\overline{Y}}^{e,i} (Z_{bi}) + \begin{bmatrix} j\omega C_{jCx} & -j\omega C_{jCx} \\ -j\omega C_{jCx} & j\omega C_{jCx} \end{bmatrix}. \tag{2.48}$$

Finally, the transformation $\overline{\overline{Y}}^e (Z_{bi}, C_{jCx}) \rightarrow \overline{\overline{Z}}^e (Z_{bi}, C_{jCx})$ facilitates the inclusion of the extrinsic resistances R_{Ex}, R_{Bx}, and R_{Cx} in Fig. 2-10(d). After a simple circuit analysis, the common-emmitter z-parameter matrix of the complete HBT circuit is

$$\overline{\overline{Z}}^e \equiv \overline{\overline{Z}}^e (Z_{bi}, C_{jCx}, R_{Ex}, R_{Bx}, R_{Cx}) = \overline{\overline{Z}}^e (Z_{bi}, C_{jCx}) + \begin{bmatrix} R_{Ex} + R_{Bx} & R_{Ex} \\ R_{Ex} & R_{Ex} + R_{Cx} \end{bmatrix}. \tag{2.49}$$

The explicit matrix manipulations explained above yield

$$z^e_{11} = \left[y^{b,i}_{22} + Z_{Bi}\Delta^{b,i}_y + j\omega C_{jCx}\left(1 + Z_{bi}\Sigma^{b,i}_y\right)\right]\Delta_0^{-1} + R_{Ex} + R_{Bx}, \tag{2.50}$$

$$z^e_{12} = \left[y^{b,i}_{12} + y^{b,i}_{22} + j\omega C_{jCx}\left(1 + Z_{bi}\Sigma^{b,i}_y\right)\right]\Delta_0^{-1} + R_{Ex}, \tag{2.51}$$

$$z^e_{21} = \left[y^{b,i}_{21} + y^{b,i}_{22} + j\omega C_{jCx}\left(1 + Z_{bi}\Sigma^{b,i}_y\right)\right]\Delta_0^{-1} + R_{Ex}, \tag{2.52}$$

$$z^e_{22} = \left[\Sigma^{b,i}_y + j\omega C_{jCx}\left(1 + Z_{bi}\Sigma^{b,i}_y\right)\right]\Delta_0^{-1} + R_{Ex} + R_{Cx}, \tag{2.53}$$

where $\Sigma^{b,i}_y \equiv y^{b,i}_{11} + y^{b,i}_{12} + y^{b,i}_{21} + y^{b,i}_{22}$, $\Delta^{b,i}_y \equiv y^{b,i}_{11}y^{b,i}_{22} - y^{b,i}_{12} + y^{b,i}_{21}$, and $\Delta_0 \equiv \Delta^{b,i}_y\left(1 + j\omega C_{jCx}Z_{bi}\right) + j\omega C_{jCx}y^{b,i}_{11}$. The small-signal parameters z^e_{11}, z^e_{12}, z^e_{21}, z^e_{22}, capture in essence the relative importance of the intrinsic and the extrinsic elements for the overall device performance. They are sufficient for the extraction of the essential figures of merit of the device.

2.9 Microwave/Millimeter Wave Figures of Merit

A HBT operates as a switch in a logic circuit and as an amplifier in an analog circuit. The current gain performance is a good indicator of the switching speed for the former whereas the power gain performance is a good measure of the power handling capability for the latter. As we shall see later, there is a correlation between the current gain and the power gain, and practical analog devices should demonstrate optimum performance for both. The emergence of a common emitter negative output resistance within the microwave/millimeter wave band indicates that a high frequency oscillator is feasible.

The common emitter forward current gain h^e_{21} is given in terms of the common-emitter z-parameters by

$$h^e_{21} = -z^e_{21}/z^e_{22}. \tag{2.54}$$

From Eqs. 2.52-2.53-2.54, it can be easily deduced that the current gain h^e_{21} is independent of R_{Bx}. The cutoff frequency f_T is the unit gain frequency of h^e_{21}. Therefore, no current amplification takes place in the frequency region $f > f_T$. It is enlightening to derive h^e_{21} for a HBT with a uniform base. If we use the approximation of Eq. 2.39 and keep only the ω^0 term in the numerator and ω^1 term in the denomenator, Eq. 2.54 simplifies to the expression

$$h^e_{21} \approx \frac{1}{j\omega\left(\tau_1 + \tau_2 + \tau_3 + \tau_4\right)}, \tag{2.55}$$

where $\tau_1 \equiv (C_{jE} + C_{jCi} + C_{jCx})/g_E$ is the emitter charging time, $\tau_2 \equiv X_B^2/(2D_n)$ is the diffusion transit time, $\tau_3 \equiv \tau_C/2$ is the collector signal delay, and $\tau_4 \equiv (C_{jCi} + C_{jCx})(R_{Ex} + R_{Cx})$ is the charging time of the capacitors. Therefore, the cutoff frequency is $f_T = \left[2\pi\left(\tau_1 + \tau_2 + \tau_3 + \tau_4\right)\right]^{-1}$. It becomes evident that cutoff frequency f_T captures compactly the characteristics of transport in the

emitter-collector direction. However, it is not a sufficient figure of merit for the horizontal transport via the base since R_{Bx} does not affect the forward current gain h_{21}^e.

The unilateral power gain U of a transistor represents the maximum achievable power gain [37]. It can be realized if a lossless feedback network is connected to the transistor so that the overall circuit is unilateral. A unilateral two-port device is characterized by perfect isolation between the input and output port. The reverse small signal transmission parameter (z_{12}, y_{12}, h_{12}, s_{12}) of a unilateral device is zero. It can be expressed in terms of the small signal z-parameters as

$$U = (1/4)\left|z_{21}^e - z_{12}^e\right|^2 \Big/ \left[\mathrm{Re}\left(z_{11}^e\right)\mathrm{Re}\left(z_{22}^e\right) - \mathrm{Re}\left(z_{12}^e\right)\mathrm{Re}\left(z_{21}^e\right)\right]. \tag{2.56}$$

The maximum oscillation frequency f_{max} is the unity gain frequency of U. The device is passive when $0 < U < 1$. Thus, f_{max} defines a boundary between the active and passive HBT operation. The frequency range where $U < 0$ marks also an active region which is particularly important for our device. The denominator of the right hand side of Eq. 2.56, includes the common emitter output resistance $r_{22}^e \equiv \mathrm{Re}\left(z_{22}^e\right)$. It is instructive to study the denominator of U. Let us assume for simplicity that $R_{Cx} = 0$ and $C_{jCx} = 0$. After a straightforward use of Eqs. 2.50-2.51-2.52-2.53, the denominator of U assumes the form $\left(Z_{bi} + R_{Bx}\right) r_{22}^e$. Thus, the unilateral power gain follows the sign of the output resistance. If r_{22}^e alternates between positive and negative values, then U takes positive and negative values accordingly. It was pointed out in [38] that negative U does not have a physical meaning because it requires a negative load for a matching termination. However, it suggests that a high gain amplifier can be realized in the frequency region where $r_{22}^e < 0$ if a resistance R_{ex} is added so that $r_{22}^e + R_{ex} \geq 0$. For a HBT of uniform base, if we follow the same approximations mentioned above for h_{21}^e and assume for simplicity that $R_{Cx} = 0$, $C_{jCx} = 0$, then $U = \omega_T \big/ \left[4\omega^2 C_{jCi}\left(Z_{bi} + R_{Bx}\right)\right]$ and $f_{max} = \sqrt{f_T / \left[8\pi C_{jCi}\left(Z_{bi} + R_{Bx}\right)\right]}$. Therefore, the maximum frequency of oscillation captures the emitter-base transport via f_T and in addition, it reflects the horizontal transport via R_{Bx}. This is evident since the power gain refers to a current and voltage ratio whereas the current gain refers only to a current ratio. The unilateral power gain is expected to be more sensitive to parasitics than the forward current gain. From the correlation between f_{max} and f_T, it becomes clear that a poor frequency performance in the current gain affects adversely the frequency performance in the power gain. Let us assume that the various extrinsic elements are favorably low to boost f_{max} while f_T is small. Since $P_{out}/P_{in} = \left(i_{out}/i_{in}\right)^2 \left(R_{out}/R_{in}\right)$, a HBT with an exceptional power gain but poor current gain is characterized by high R_{out}/R_{in}. This is not practical for most common applications since the source at the input of the HBT and the load at the output of the HBT have similar values of input resistance and $R_L/R_S \approx 1$. Therefore, a large impedance mismatch will take place and the actual delivered power will be low. Thus, the optimization of both unilateral power gain and current gain is essential.

The feasibility of a negative common emitter output resistance can be easily examined for the intrinsic case. If we set R_{Ex}=R_{Cx}=0 and C_{jCx}=0 in Eq. 2.53, the intrinsic common emmiter output

Table 2.2: Parameters used for the HBT evaluation

Perpendicular dimensions (Å)	X_{CAP}=1500, X_E=1500, X_{SC}=10000, X_C variable
Horizontal dimensions (μm)	W_E=2, W_B=1.5, W_{SC}=20, S_{BE}=0.3, S_{EC}=3, L_E=15
Doping (cm^{-3})	$N_{CAP}=5 \times 10^{18}$, $N_E=5 \times 10^{17}$, $N_B=2 \times 10^{19}$, $N_C=2 \times 10^{16}$, $N_{SC}=5 \times 10^{18}$
Base impurity length (Å)	l_{imp}=300
Contact resistivity (Ω-cm^2)	$\rho_{cap,c}=10^{-6}$, $\rho_{b,c}=10^{-6}$, $\rho_{sc,c}=10^{-6}$
Al concentration	x_E=0.35, x_C=0
Energy gap discontinuity between succesive steps	Δ=1.2 $\hbar\omega_{LO}$
Bias conditions (V)	V_{BE}=0.95 Φ_{bi}, V_{CB} sufficient for $X_{dep,C}=X_C$
Electron saturation velocity (cm/s)	$v_{sat}=8 \times 10^6$

resistance can be written as

$$r_{22}^{e,i} = \left(\mathrm{Re}\,(g_e)\Big/|g_e + j\omega C_{jE}|^2\right) - \mathrm{Im}\,(\alpha_E\alpha_T\alpha_C)/(\omega C_{jCi}), \tag{2.57}$$

where Re and Im denote the real and imaginary part of an expression, respectively. Depending on the values of $\angle\alpha_E\alpha_T\alpha_C$, $\mathrm{Im}\,(\alpha_E\alpha_T\alpha_C)$ can take negative and positive values. Therefore, for a sufficiently large $|\alpha_E\alpha_T\alpha_C|$, $r_{22}^{e,i}$ can alternate between positive and negative values in various frequency regions. This is a transit time effect since the emergence of negative output resistance stems from the injection delay $\angle\alpha_E\alpha_T$ of the current entering the drift region of the collector. The injection mechanism is phonon-enhanced diffusion in the base. The importance of α_T becomes evident. Large values of $|\alpha_T|$ and $\angle\alpha_T$ are essential for the achievement of negative output resistance. The role of a_C must also be underscored. The collector delay facilitates significantly the requirement for large $\angle\alpha_E\alpha_T\alpha_C$. The complete expression of r_{22}^e that incorporates the intrinsic and extrinsic elements of the device is more complex than that of Eq. 2.57. However, it can be readily derived from Eq. 2.53. The presense of the extrinsic elements makes the requirement for large $\angle\alpha_E\alpha_T\alpha_C$ and $|\alpha_E\alpha_T\alpha_C|$ even more demanding. It is worth noticing that the emergence of negative resistance is a an inherent device property. This should be contrasted with the most common oscillatory systems that usually employ a high frequency amplifier and a properly designed feedback system in order to achieve negative output resistance.

2.10 HBT Microwave/Millimeter Wave Performance

The intrinsic and extrinsic elements of the HBT affect the overall device performance. Their relative importance can be easily unfolded by the derived small signal parameters z_{11}^e, z_{12}^e, z_{21}^e, z_{22}^e and the microwave/millimeter wave figures of merit. The commom emitter forward current gain h_{21}^e, the unilateral power gain U, and the common emitter output resistance r_{22}^e will be examined for a HBT

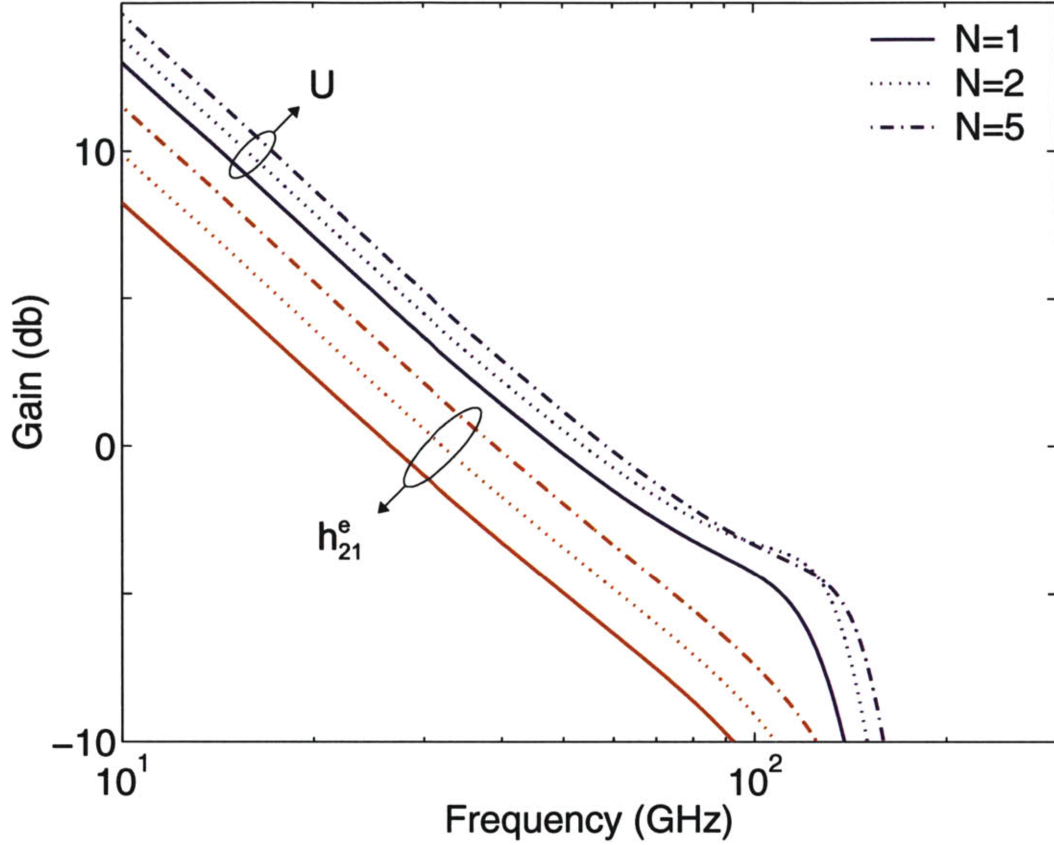

Figure 2-11: Unilateral power gain U (blue curves) and common emitter forward gain h^e_{21} (red curves) for a HBT with $N \times X_{step}$=1000 Å, X_C=4000 Å, device parameters of Table 2.2, and variable number of base steps (N=1, 2, 5). The introduction of base steps results in larger $|\alpha_T|$, improving both U and h^e_{21}.

structure with the devices parameters of Table 2.2.

We consider the case of a HBT with constant base thickness, $N \times X_{step}$=1000 Å, and variable number of base steps, N=1, 2, 5. The simulation results are presented in Fig. 2-11. The intrinsic operation of this structure has already been studied in Fig. 2-5. The introduction of base steps decreases the magnitude attenuation and the phase delay of the base transport factor. The transport of minority carriers is accelerated and the improvement of the high frequency performance is reflected by both U and h^e_{21}. Therefore, an important perspective of the device is the enhanced frequency performance by the combination of low base resistance (large $N \times X_{step}$) and fast transport (large N, moderate X_{step}).

The most important aspect of the device of this work is the potential for negative output resistance due to the transit time effect. We examine in Fig. 2-12 a HBT structure with an increasing number of base steps N=1,2,5, and constant base step thickness, X_{step}=600 Å. As N increases, the base resistances R_{Bx} and Z_{bi} decrease and the base transit time increases. The reduction of Z_{bi} does

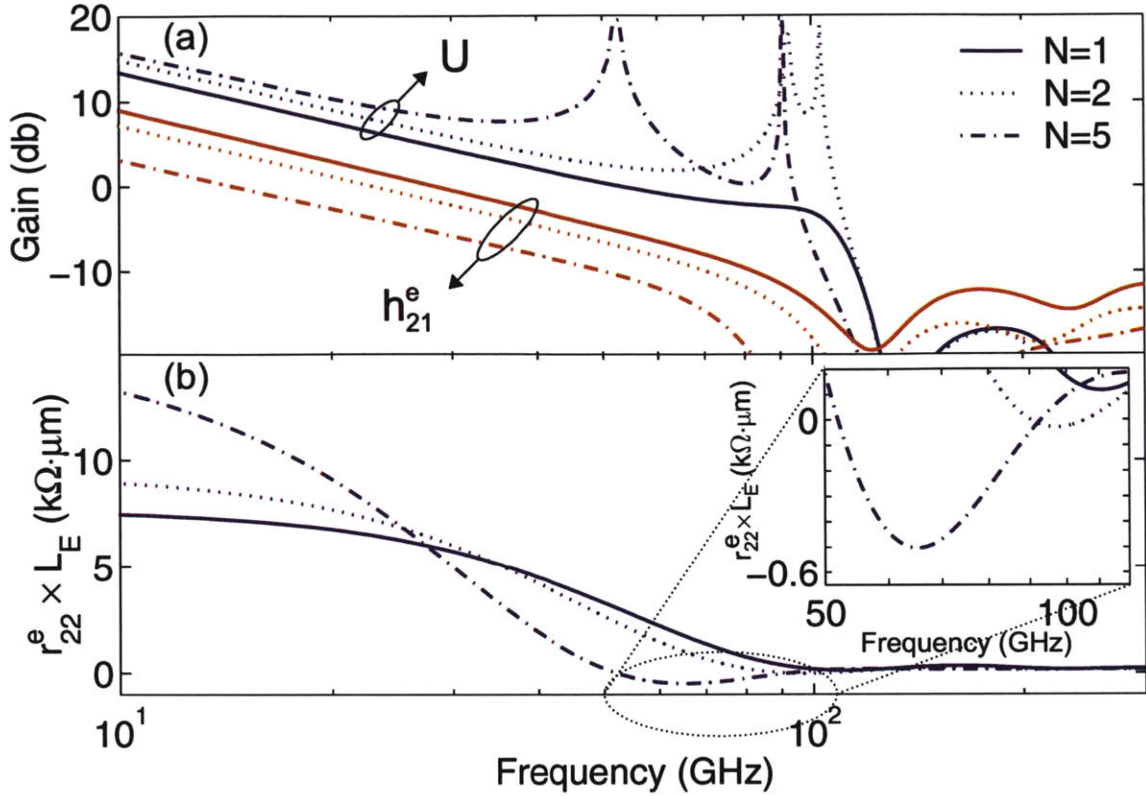

Figure 2-12: (a) Unilateral power gain U (blue curves), common emitter forward gain h^e_{21} (red curves), and (b) output resistance for X_{step}=600 Å, X_C=6000 Å, device parameters of Table 2.2, and variable number of base steps (N=1, 2, 5). The inset in (b) is a magnification of the output resistance for the frequency range 50-120 GHz. As the number of base steps increases, peaks of resonance appear for the unilateral power gain. These shift to lower frequencies for increasing N and $U < 0$, $r^e_{22} < 0$ between the first two peaks. The maximum value of $|r^e_{22}|$ when $r^e_{22} < 0$ increases for increasing N. The larger base transport delay causes a shift of f_T to lower frequencies.

not improve the current gain significantly. However, the increase of the base transit time shifts f_T to lower frequencies. On the other hand, f_{max} shifts to higher frequencies. This is expected since the unilateral power gain is favored by low values of R_{Bx} and Z_{bi}. Furthermore, the unilateral power gain resonances for N=2,5 extend the frequency range for power amplification. By increasing the number of base steps from N=1 to N=2, f_{max} shifts from 53 GHz to 105 GHz. Additional steps result in slightly lower f_{max} but higher values of negative output resistance. This is a general trend. If our goal is a trade-off between f_T and f_{max}, there exists an optimum number of base steps N_{opt} for the highest f_{max}. For the case of Fig. 2-12, N_{opt}=2. Additional steps shift the peaks of resonance and f_{max} to lower frequencies. If our aim is a high negative output resistance for the implementation of an oscillator, the choice of N depends on the frequency of interest. It is worth noticing that the negative output resistance is band-limited. On the contrary, RTDs have a broadband negative resistance which causes dc instabilities.

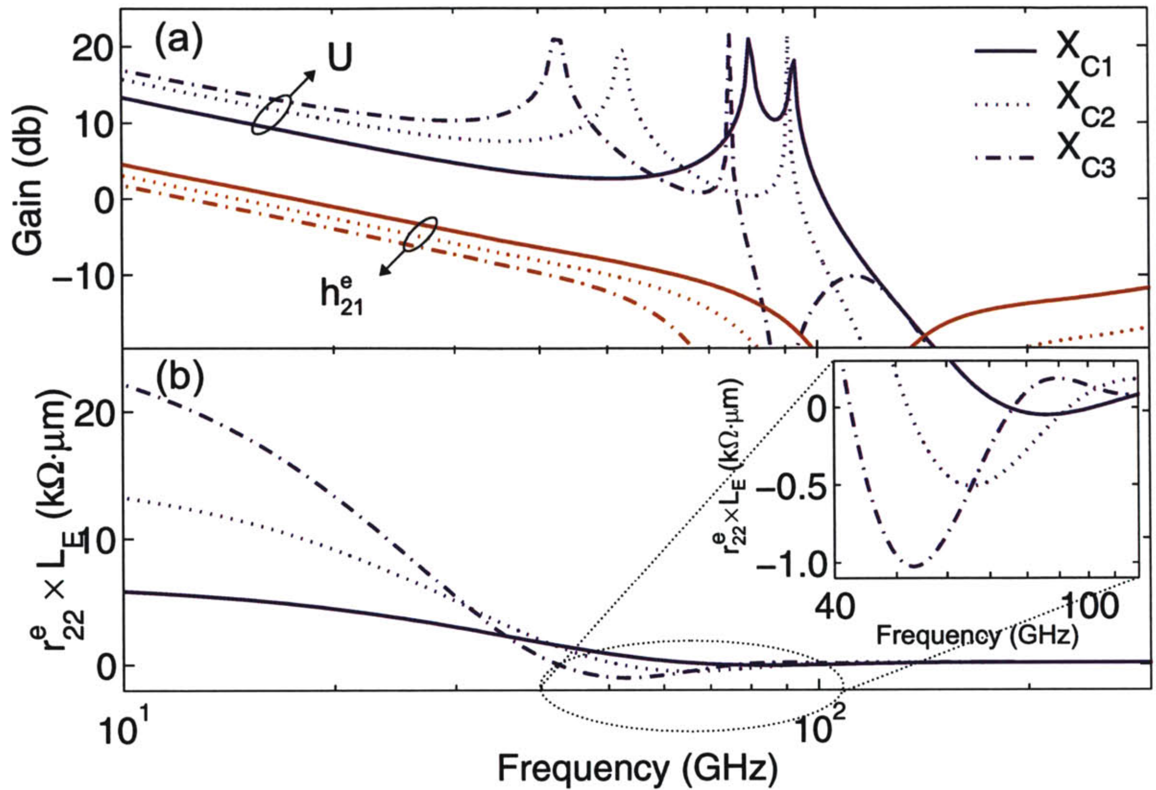

Figure 2-13: (a) Unilateral power gain U (blue curves), common emitter forward gain h_{21}^e (red curves), and (b) output resistance for N=5, X_{step}=600 Å, device parameters of Table 2.2, and variable collector thickness (X_{C1}=3000 Å, X_{C2}=6000 Å, X_{C3}=9000 Å). The inset in (b) is a magnification of the output resistance for the frequency range 40-120 GHz. As the collector thickness increases, the peaks of unilateral power gain resonance shift to lower frequencies, and f_T decreases due to the larger collector delay. The maximum value of $|r_{22}^e|$ when $r_{22}^e < 0$ increases and shifts to lower frequencies for increasing X_C.

The role of the collector thickness X_C must not be underestimated. The collector transit delay is crucial for the achievement of a high-value negative output resistance. A large number of base steps combined with a small collector thickness is not usually sufficient for an oscillatory behavior. The simulation results of a HBT with N=5, X_{step}=600 Å, and variable collector thickness, are presented in Fig. 2-13. As X_C increases, the peaks of resonance move to lower frequencies. In addition, the maximum value of $|r_{22}^e|$ when $r_{22}^e < 0$, shifts to lower frequencies and increases significantly. Therefore, engineering both α_T and α_C by the choice of X_{step}, N, and X_C is required for a high performance microwave/millimeter wave oscillator.

Chapter 3

HBT Design and Fabrication

The design of our HBT consists of the choice of the material parameters and the various layout details. We unfold the various material parameters by casting light upon the MBE design and the ohmic contacts in the following sections. The layout details refer to the device layout, the transmission line design, the on-wafer calibration structures, and the device isolation. Finally, the fabrication will be discussed in extent unveiling the important details of the process flow.

3.1 MBE Design

The design of the MBE growth focuses on the material, the thickness, and the doping level of the device layers. Furthemore, the substrate temperature during the MBE growth is crucial for the quality of the grown layers. The choice of these parameters is dictated by the simulation results of the device. These were produced by the simulation tools described in Chapter 2. In addition, the design parameters should be within the acceptable limits set by our MBE collaborator. The material sources that are allowed in the MBE chamber, the minimum and maximum doping levels as well as the background doping level, the type of dopants, the control of the layer thickness and the composition of the material, and the alloy grading capability are some of the contraints that should be taken into account. The various MBE design parameters are shown in Table 3.1. In what follows, we will discuss these choices in detail.

The Al concentration of the emitter should be large enough so that there is a satisfactory bandgap difference between the emitter and the base for the suppression of the base current. We set a 35% Al concentration for the emitter. The emitter thickness is not a critical parameter. It should be sufficiently large to account for the emitter-base depletion region. There should also be adequate distance between the emitter and base contact to avoid a possible electric short during the base metal evaporation. On the other hand, large emitter resistance and excessive undercut during the emitter wet etching characterize a HBT with thick emitter. We designed a 900 Å emitter and a

Table 3.1: Design sheet for the MBE growth of the device. The device consists of the emitter cap, the emitter, the spacer, the base, the collector, and the subcollector. The collector thickness varies depending on the frequency range of interest for transit-time oscillations.

Layer	Material	Doping (cm^{-3})	Thickness (Å)	Sub. Temperature (°C)	Description
1	$In_{0.6}Ga_{0.4}As$	n^+, 2×10^{19}	500	450	
2	$In_xGa_{1-x}As$, $x=0.6 \rightarrow 0$ (Linear Grading)	n^+, 2×10^{19}	500	450	Emitter Cap
3	GaAs	n^+, 5×10^{18}	500	600	
4	$Al_yGa_{1-y}As$, $y=0 \rightarrow 0.35$ (Linear Grading)	n, 5×10^{17}	300	600	
5	$Al_{0.35}Ga_{0.65}As$	n, 5×10^{17}	900	600	Emitter
6	$Al_zGa_{1-z}As$, $z=0.35 \rightarrow 0.18$ (Linear Grading)	n, 5×10^{17}	200	600	
7	$Al_{0.18}Ga_{0.82}As$	undoped	100	600	Spacer
8	$Al_{0.18}Ga_{0.82}As$	p^+, 2×10^{19}	600	550	
9	$Al_{0.14}Ga_{0.86}As$	p^+, 2×10^{19}	600	550	
10	$Al_{0.10}Ga_{0.90}As$	p^+, 2×10^{19}	600	550	Base
11	$Al_{0.05}Ga_{0.95}As$	p^+, 2×10^{19}	600	550	
12	GaAs	p^+, 2×10^{19}	600	550	
13	GaAs	n, $\leq 3 \times 10^{16}$	variable	600	Collector
14	GaAs	n^+, 5×10^{18}	1000	600	Subcollector
15	GaAs	S.I			Substrate

200 Å layer with linear alloy-grading between the base and the emitter for a smooth transition of the conduction band. Although the parabolic grading has been proven to be better than the linear grading in terms of conduction band smoothness under bias conditions [39], such a capability was not available for our growth. The emitter doping level should not be too low because a conduction band spike appears in the alloy-graded region at high bias voltage V_{BE} [39, 40]. This can be easily explained. The conduction-band edge E_C can be obtained by the superposition of the alloy-grading potential φ_G and the electrostatic potential across the junction φ_{ES}, $E_C = \varphi_G - \varphi_{ES}$. ϕ_G is a linear function of the grading distance for linear alloy-grading , whereas φ_{ES} is a parabolic function of the distance in the space-charge region of the emitter-base junction. We illustrate E_C vs distance from the emitter-base junction for N_E=1 $\times$ 10^{17} cm^{-3} in Fig. 3-1(a), and N_E=5 $\times$ 10^{17} cm^{-3} in Fig. 3-1(b). For the same bias voltage V_{BE}, the lower the value of N_E is, the larger the depletion

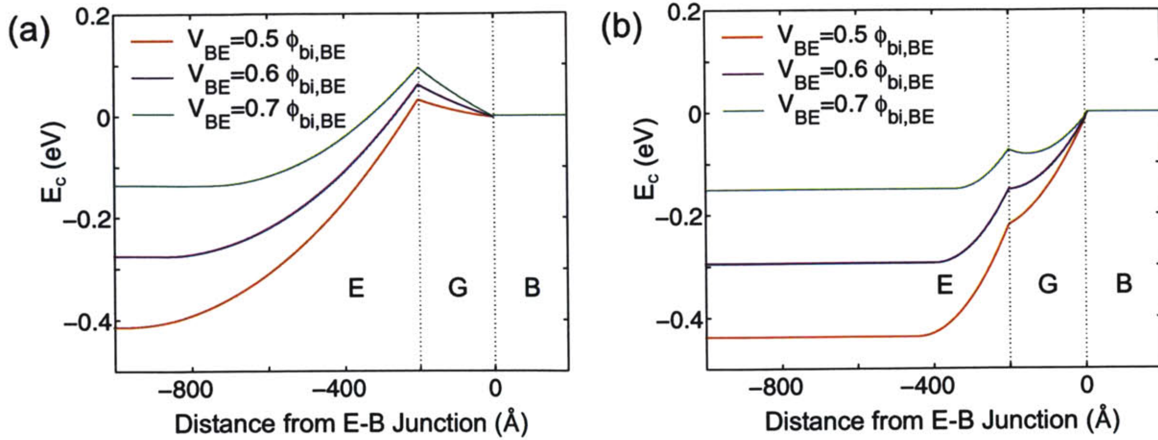

Figure 3-1: Conduction band edge vs distance from the E-B junction for a family of V_{BE} values. The emitter is $Al_{0.35}Ga_{0.65}As$, the base is GaAs and the thickness of the linear alloy-grading layer is 200 Å. The base doping level is N_B=2×10^{19} cm^{-3}. The emitter doping level is N_E=1×10^{17} cm^{-3} in (a), and N_E=5×10^{17} cm^{-3} in (b). The superposition of the linear alloy-grading potential and the electrostatic potential creates a barrier for the transport of electrons in (a), and a slight peak in (b).

layer becomes. In Fig. 3-1(a), a barrier for the transport of electrons is created in E_C. In Fig. 3-1(b), a slight peak is created in E_C. Consequently, the E-B junction of Fig. 3-1(b) is more preferable than the E-B junction of Fig. 3-1(a). We should point out that a low N_E creates an additional problem. When I_E is high, the mobile carriers can compensate the background charge of the space charge region and additional dips or barriers are created in the conduction band. It also becomes clearer why parabolic alloy-grading is better than linear alloy-grading. In parabolic grading, both φ_{ES} and φ_G vary parabolically with the distance and after a careful choice of material parameters, E_C varies smoothly in the space-charge region. We should point out that a high N_E increases the emitter-base capacitance C_{jE}. We chose the moderate value of N_E=5×10^{17} cm^{-3}. A substrate temperature of 600 °C during the emitter growth yields good quality $Al_xGa_{1-x}As$. The emitter cap shown in Table 3.1 will be explained during the discussion of the device ohmic contacts.

The base step thickness must be sufficiently large to allow the formation of a Maxwellian distribution via the randomizing mechanism of impurity scattering. Furthermore, X_{step} must not be excessively large in order to have a moderate magnitude attenuation of the base transport factor. We chose X_{step}=600 Å. The number of base steps affects significantly the frequency range of the transit-time oscillations. We set N=5, so that the transit-time effect can be easily captured by the network analyzer operating in the 0-67 GHz range. The frequency shift of the transit-time effect with the addition of base steps was illustrated in Fig. 2-12. We can achieve a conduction band discontinuity Δ=1.2 $\hbar\omega_{\text{LO}}$ between succesive steps if the change of the Al concentration is 3.5 %. The MBE grower set a change of 4 % in the Al concentration as a safer choice for reliable MBE growths.

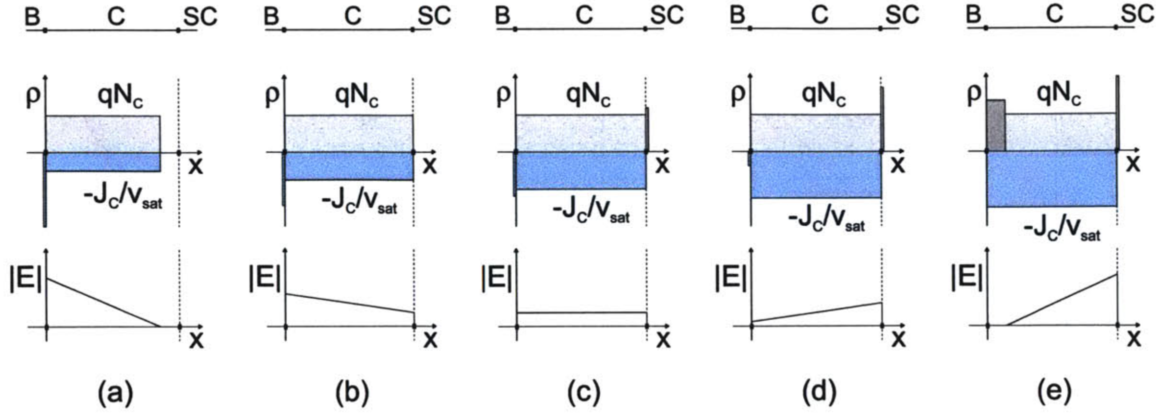

Figure 3-2: Illustration of the charge concentration ρ and the magnitude of the electric field $|E|$ in the collector for different values of the collector current density J_C and constant value of V_{CB}. The base, collector, and subcollector regions are designated by B, C, and SC, respectively. In (a), the collector is partially depleted and J_C is low. As J_C increases, the net positive charge in the collector decreases and the space-charge region in the collector increases. In (b), the collector is fully depleted and $J_C < qN_C v_{sat}$. In (c), ρ=0 in the collector and $|E|$ is constant. In (d), $\rho < 0$ in the collector and $|E|$ is low towards the base. In (e), high values of J_C result in vanishing $|E|$ at the B-C junction and base pushout occurs.

In addition, the Al concentration of the fourth step is relatively low and not easily controlled. For this reason, we adopted a 4 % Al concentration step for the first and second base step discontinuities, and a 5 % Al concentration step for the third and fourth base step discontinuities. The doping of the base must be high enough so that both R_{Bx} and Z_{bi} are sufficiently low. The dopant used by our MBE grower is Be. The MBE growth of a p^+-$Al_xGa_{1-x}As$ layer is characterized by an inherent difficulty [41, 42]. A high substrate temperature, about 600 °C, favors the incorporation of Al. A lower substrate temperature may lead to increased recombination centers. On the other hand, we can achieve a high level of p-type doping ($\geq 5\times10^{19}$cm^{-3}) at a low substrate temperature, about 450-500 °C. At high substrate temperature, the Be atoms are placed in antisites or intertitial sites and not in group III sites. Therefore, the Be atoms cannot activate as acceptors and the doping level is lower than expected. Furthermore, dopant outdiffusion towards the emitter can take place during the growth or at forward bias conditions [43, 44]. This deteriorates the HBT operation since the emitter-base junction shifts towards the wide-bandgap emitter and the HBT becomes a BJT. Abrupt HBT devices (no alloy grading between the emitter and base) suffer from this effect since a small Be outdiffusion can transform the HBT into a BJT. The design compromise that we followed was to choose a moderate base doping, N_B=2×10^{19} cm^{-3}, at a moderate substrate temperature during MBE growth, T_{sub}=550 °C. In addition, a thin undoped spacer is grown between the emitter and the base to account for a possible Be outdiffusion towards the emitter.

The collector design determines to a large extent the frequency range of transit-time oscillations

and the maximum value of the output negative resistance. This was illustrated in Fig. 2-13. For this work, we kept the same MBE layers for all of our devices with the exception of the collector layer. In our design approach, we always assume that the bias voltage V_{CB} is large enough so that the collector is fully depleted. This stems from the fact that the capacitance of an undepleted collector can be prohibitively large, washing out the emergence of negative resistance. Transit-time oscillations are more pronounced for $X_C \geq 6000$ Å and the frequency band of negative output resistance is within the frequency range of the network analyzer. Most HBT designs include a moderate level of N_c, in the vicinity of 10^{17} cm^{-3} or higher. High values of N_C increase the maximum collector current density, $J_{\rm Kirk}$, before the onset of the base pushout effect or Kirk effect [35].

An illustration of the emergence of the Kirk effect is show in Fig. 3-2. Let us assume that V_{CB} is low enough that the collector is partially depleted. If J_C is low, then $\rho \approx N_C$, where ρ is the net charge density in the depleted collector (Fig. 3-2(a)). As J_C increases, the total charge of the mobile carriers becomes significant and $\rho = N_C - J_C/v_{sat}$, where we assume that the electrons move with the saturation velocity v_{sat}. The space-charge region increases until the collector becomes fully depleted (Fig. 3-2(b)). The depletion region cannot increase further since the subcollector is heavily doped. The electric field becomes constant across the collector when $\rho = 0$ (Fig. 3-2(c)). Higher values of J_C lead to $\rho < 0$ and the magnitude of the electric field close to the base assumes lower values (Fig. 3-2(d)). In the extreme case of very high J_C, the electric field vanishes at the base-collector junction. Since there is no electric field to keep the holes in the base, they move into the collector and the base pushout effect or Kirk effect takes place. In Fig. 3-2(e), it becomes evident that the effective base thickness is larger than the actual base thickness. In conclusion, the Kirk effect is related to the compensation of the background charge density by the charge density of the mobile carriers. It manifests by the increase of the space charge region, and finally by the base pushout. We define as $J_{\rm Kirk}$ the value of J_C where the electric field vanishes at the base-collector interface. After some calculations, it can be shown that $J_{\rm Kirk} = [1 + (V_{CB} + \varphi_{bi,BC})/(V_2 + \varphi_{bi,BC})]\, qN_C v_{sat}$, where V_2 is the value of V_{CB} that fully depletes the collector for J_C=0. We can clearly see that high values of N_C lead to high $J_{\rm Kirk}$.

The collector thickness of our device is much larger than in most common HBT devices. A high doping level would call for a very large value of V_{CB} for full collector depletion. This leads to elevated power levels and collector-base bias close to the breakdown voltage of the collector. For this reason, we chose a lower doping level with a moderate value of $J_{\rm Kirk}$. For N_C=2$\times$10^{16} cm^{-3}, V_{CB}=5.4 V for X_C=7000 Å, V_{CB}=9.8 V for X_C=9000 Å, and $J_{\rm Kirk}$=51 kA/cm^2. A substrate temperature of 600 °C during the collector growth produces good quality GaAs.

The collector-subcollector junction is a homojunction and the subcollector consists of a GaAs layer. From Eq. 2.44, the value of R_{Cx} decreases as the subcollector sheet resistance $R_{sc,s}$ decreases. Therefore, large subcollector thickness X_{sc} and high doping level N_{sc} are desirable design features.

As we shall see in Sec. 3.7, device isolation requires an etching of about 1.5-2 μm after the evaporation of the subcollector metal. The maximum doping level of a n-type GaAs layer is 5×10^{18}. Therefore, we can choose the parameters N_{sc}=5×10^{18} cm^{-3}, and X_{sc}=1 μm. We chose the same substrate temperature during the subcollector growth as for the collector growth.

3.2 Ohmic Contacts

The importance of the extrinsic resistances R_{Ex}, R_{Bx}, R_{Cx} became evident from the expressions of the common-emitter small signal parameters in Eqs. 2.50-2.53 and the discussion about the microwave/millimeter-wave parameters in Sec. 2.9. Poor ohmic contacts, especially for the emitter and the collector, can deteriorate the performance of our device. Transit-time oscillations call for low values of extrinsic resistances and capacitances.

As mentioned before, the maximum doping level of a n-type GaAs is about 5×10^{18} cm^{-3}. This is a relatively low value and the implementation of an ohmic contact on n-GaAs with specific contact resistance better than 10^{-6} $\Omega\cdot$cm^2 becomes challenging. For the subcollector, an alloyed ohmic contact is suitable. The diffusion of metals in the subcollector during the annealing process is acceptable since there is no active layer under the subcollector. Furthermore, the subollector is much thicker than a moderate diffusion distance. A specific contact resistance of 3×10^{-7} $\Omega\cdot$cm^2 has been reported in [45] using a Au(88%)Ge(12%)/Ni/Ti/Au metallization and an alloying temperature of 370 °C for 30 s. AuGe melts above 360 °C and the diffusion of AuGe/Ni takes place. For this work, we used a similar metallization, namely Ni/Au/Ge/Au/Ni/Au, and an alloying temperature of 380 °C for 30 s [46].

The emitter thickness is relatively small and an alloyed ohmic contact should be avoided if possible. The use of a low temperature grown GaAs (LTG:GaAs) could be adopted [47, 48]. However, the commonly achieved specific contact resistance of 2×10^{-6} $\Omega\cdot$cm^2 on LTG:GaAs is not exceptionally low and subsequent thermal treatment is restricted. A shallow alloyed ohmic contact for an emitter-up HBT configuration was proposed in [49]. This is a Pd/Ge metallization with a 535 °C annealing temperature for 90 s. The reported specific contact resistance is relatively low, about 4×10^{-7} $\Omega\cdot$cm^2. For this work, we adopted a commonly used approach for $\mathrm{Al_xGa_{1-x}As}$/GaAs HBT devices. An $\mathrm{In_xGa_{1-x}As}$ cap was grown on top of the emitter and a Ti/Pt/Au metallization was evaporated to provide a non-alloyed ohmic contact [50, 51, 52, 53]. The Pt layer serves as a barrier for the diffusion of Au during subsequent annealing steps. The maximum doping level of n-type $\mathrm{In_xGa_{1-x}As}$ increases with the In mole concentration and it can reach the value of 2×10^{19} cm^{-3} for $\mathrm{x} \geq 0.65$ [51]. The electron affinity of $\mathrm{In_xGa_{1-x}As}$ is given by $X_e\,(\mathrm{In_xGa_{1-x}As}) = (4.07 + 0.83x)$ eV. For high mole concentration of In, $X_e\,(\mathrm{In_xGa_{1-x}As})$ becomes higher than the work function Φ of most common metals ($\Phi_{\mathrm{Ti}} = 4.3$ eV $< X_e\,(\mathrm{In_xGa_{1-x}As})$ for $x > 0.72$ [54]). Therefore, the barrier

height of the Schottky contact is negative and the $In_xGa_{1-x}As$ conduction band bends downwards at the metal/$In_xGa_{1-x}As$ interface. Thus, no tunneling takes place contrary to the most common ohmic contacts, and the transport of carriers is enhanced. However, it is not necessary to achieve a negative barrier height for a good ohmic contact. Satisfactory results can be obtained by a sufficient lowering of the Schottky contact barrier height. The reported specific contact resistance is in the vicinity of $10^{-8}\ \Omega \cdot cm^2$ for $x \geq 0.6$. Furthermore, the metallization is acceptably stable for the subsequent step of the subcollector contact annealing [55, 56]. As shown in Table 3.1, the emitter cap consists of three layers with a linear alloy grading so as to achieve a smooth conduction band transition between the metal contact and the emitter. The substrate temperature of 450 °C during the MBE growth of the $In_xGa_{1-x}As$ layers yields high doping level.

A deep alloyed ohmic contact for the base may cause an electric short between the base and the collector if the alloying depth is high. Again, a non-alloyed base ohmic contact is desirable. A Pt/Ti/Pt/Au contact on p-type $Al_xGa_{1-x}As$ for the purpose of contacting the base of an $Al_xGa_{1-x}As$/GaAs HBT was used in [57, 58]. The reported specific contact resistance is about $4\times10^{-7}\ \Omega \cdot cm^2$ which is satisfactory for our device. The use of the first Pt layer is suggested because of its low barrier height when contacting a p-type semiconductor. In addition, Pt can easily penetrate the native oxide of $Al_xGa_{1-x}As$ at temperatures higher than 350 °C and forms the thermally stable intermetallic compound $PtAs_2$. The second Pt layer prevents the Au diffusion during subsequent thermal annealing steps. This ohmic contact was used in our work when N_B=5×10^9 cm^{-3}. For lower base doping levels, the use of alloyed ohmic contacts is unavoidable. The most common p-dopants used in alloyed ohmic contacts to p-GaAs are Be, Zn, and Mn. A satisfactory ohmic contact on p-GaAs using an alloyed Pt/Zn/Au layer was suggested in [59]. The Pt layer offers the benefits discussed earlier, and in addition, it controls the thickness of the alloyed layer. Zn diffuses through the Pt in the GaAs or $Al_xGa_{1-x}As$ layer creating a shallow layer (50-100 Å) of high doping level. This is particularly important for the base layer. Furthermore, the specific contact resistance is less sensitive to the Al concentration of the $Al_xGa_{1-x}As$ layer as opposed to the more common Au/Zn/Au contact. The reported specific contact resistance is $5\times10^{-7}\ \Omega \cdot cm^2$ on p-GaAs with doping level $5\times10^{18}\ cm^{-3}$ and alloying conditions 360 °C for 40 s. We utilized this contact when N_B=$2\times10^{19}\ cm^{-3}$.

3.3 Device Layout

The layout of the device must fulfill the requirements set by the demand for low extrinsic resistances and capacitances. Furthermore, the layout of the device must comply with the limitations of the clean room facilities. Therefore, a high yield fabrication process imposes layout restrictions. The mask design should reflect an optimum compromise between the desired and the feasible geometries.

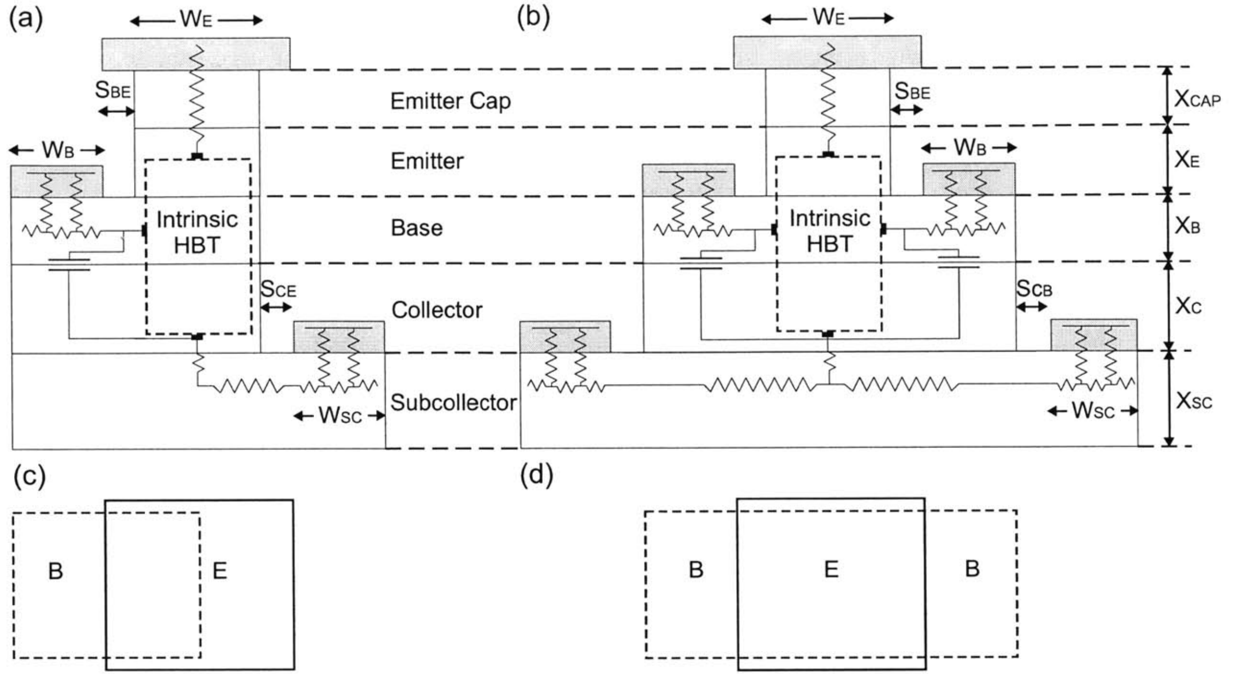

Figure 3-3: Schematic of emitter-up HBT configurations with a (a) B-E-C mesa, and (b) C-B-E-B-C mesa. The dashed rectangle in (a) and (b) indicate the intrinsic part of the device. The emitter-base masks of (a) and (b) are shown in (c) and (d), respectively. The emitter-base masks are designed for self-aligned HBTs. The S_{BE} separation between the emitter and the base is due to wet etching.

The HBT of this work is self-aligned. Self alignment refers to the emitter-base alignment and ideally $S_{BE} \approx 0$, where S_{BE} is illustrated in Fig. 3-3. According to Eq. 2.43, the extrinsic base section along S_{BE} contributes to the extrinsic base resistance. More importantly, the extrinsic base-collector capacitance C_{jCx} increases with an increasing S_{BE} as indicated in Eq. 2.45. A large C_{jCx} can be detrimental for the device performance since it can wash out any transit-time effect. Many researchers have proposed a number of novel fabrication techniques for self-aligned HBTs [60, 61, 62, 63, 64, 65]. These ideas apply for a C-B-E-B-C mesa configuration shown in Fig. 3-3(b), where E, B, and C denote the emitter, the base, and the collector, respectively. The emitter-base masks of Fig. 3-3(a)-(b) are illustrated in Fig. 3-3(c)-(d), respectively. The advantage of the C-B-E-B-C mesa during the photolithography process is that a horizontal misalignment of the base with respect to the emitter will not affect the total base area. On the other hand, the base-emitter alignment is crucial for the B-E-C mesa since it affects directly the base area. The extrinsic elements of the two mesa configurations differ as expected. If we follow carefully the steps outlined in Sec. 2.7, we can readily derive the relations between the extrinsic elements:

$$Z_{bi,2} = Z_{bi,1}/4, \tag{3.1}$$

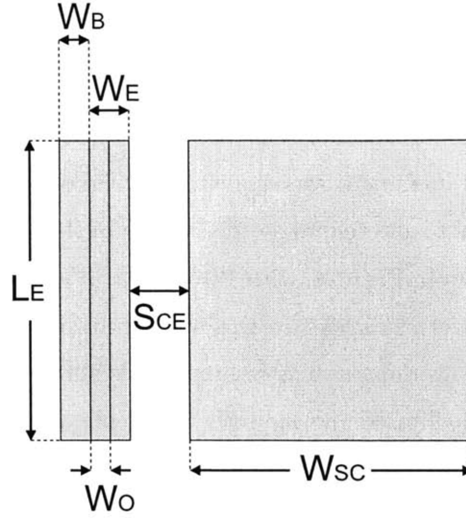

Figure 3-4: Detail of the device layout illustrating the various dimensions of importance. The coplanar waveguide connected to the HBT is not shown.

$$R_{Bx,2} = R_{Bx,1}/2, \tag{3.2}$$

$$C_{jCx,2} = 2C_{jCx,1}, \tag{3.3}$$

$$R_{Cx,2} = \frac{\sqrt{\rho_{sc,c}R_{sc,s}}}{2L_E}\coth\left(W_{SC}\sqrt{R_{sc,s}/\rho_{sc,c}}\right)+\frac{R_{c,s}S_{CB}}{2L_E}+\frac{\rho_{sc}\left(W_E+W_B+S_{BE}\right)}{12L_E}+\frac{\rho_c\left(X_C-X_{dep,C}\right)}{W_E L_E}, \tag{3.4}$$

where the subscripts 1 and 2 refer to the B-E-C and C-B-E-B-C configurations, respectively, and the various definitions of Sec. 2.7 are used. These expressions reveal that the extrinsic resistances are lower for the C-B-E-B-C mesa configuration whereas the extrinsic base-collector capacitance C_{jCx} is lower for the B-E-C mesa configuration. Simulations of both structures revealed that the B-E-C mesa configuration yielded higher values of negative resistance. Therefore, it appears that a low C_{jCx} and moderate values of extrinsic resistances favor the emergence of transit time effects.

An additional advantage of the B-E-C mesa configuration is that the terminals are readily accesible. A coplanar waveguide system can be easily devised for a common emitter configuration since the base, the emitter, and the collector electrodes are naturally separated. On the contrary, the C-B-E-B-C mesa configuration complicates the fabrication process. The presence of two base and two collector contacts calls for the the use of airbridges. This is not a trivial process because it requires the use of sacrificial layers and electroplating. In addition, airbridges can add significant parasitic capacitances. For all the aforementioned reasons, we chose the simple B-E-C mesa configuration for the HBT of this work, despite the misalignment sensitivity during photolithography that this design entails.

The Karl-Suss aligner of the clean room can achieve a minimum dimension of about 1.2-1.5 μm

with the AZ5206 photoresist (0.6 μm thickness). The emitter width W_E and the base width W_B must be small enough so that the values of intrinsic devices capacitances C_{jE}, C_{jCi}, and the extrinsic capacitance C_{jCx} are sufficiently low. The base should also be aligned with the emitter electrode. During the early stages of the fabrication process, we tried to achieve small emitter widths of 1-1.5 μm. However, the base-emitter alignment was dificult, the yield of a thin emitter electrode was low, and the undercut during the first wet etch made the stiction of the emitter metal weak. We chose a more conservative design, shown in Fig. 3-4, with W_E=2 μm, W_B=1.5 μm, and W_O=1 μm overlap between the base and the emitter electrode. In this way, both the alignment marks and the visual verification of the base-emitter overlap serve as essential tools for the self-alignment process. A high resolution stepper could have facilitated enormously the fine photolithography in terms of minimum dimension, alignment, yield, and time.

The emitter-collector separation S_{CE} is not crucial. According to Eq. 2.44, the separation S_{CE} gives rise to the extrinsic transverse collector resistance. However, the collector contact resistance is higher than any of the other contributing terms of the total extrinsic collector resistance R_{Cx}. A self-aligned emitter-collector design reduces significantly the S_{CE} separation but it poses a potential problem. If the subcollector is reached via dry etching, the semiconductor surface must undergo a shallow wet etching prior to subcollector metal evaporation. This wet etching ensures a clean surface for the subsequent ohmic contact. The emitter must be protected with photoresist from undesirable undercuts during this wet etching. Therefore, a non-zero S_{CE} separation is inevitable. We chose an emitter-collector separation S_{CE}=3 μm. According to Eq. 2.44, R_{Cx} reduces for increasing W_{SC}. If the subcollector width W_{SC} is larger than the subcollector transfer lenth $L_{SC,T}$, the improvement in R_{Cx} is minimal. Here, we chose W_{SC}=14 μm. This was dictated mostly by the coplanar waveguide design and not by the value of $L_{SC,T}$. As we shall see later in the discussion of the transmission line design and the device isolation strategy, the subcollector contact includes the whole collector electrode of the HBT coplanar waveguide.

To a first approximation, the dimension L_E does not affect the device operation. The common emitter output resistance is inversely proportional to L_E. A large L_E increases the chances for an electric short between the emitter and the base contact during the base metal deposition. The length of the device must also be compatible with the coplanar waveguide design. For our device layout, we chose L_E=15 μm. According to [35], a large L_E can cause secondary effects due to the finite voltage drop along L_E and the temperature gradient along L_E. More specifically, a long device exhibits nonuniform current distribution because of the distributive nature of resistances along the device. This is similar to the transmission line model discussed in Sec. 2.7 for the base and collector contact resistance. In addition, a temperature gradient occurs in long devices, with the highest temperature at the center of the device. This leads to lower turn-on voltage near the hot spot of the device and the emitter current is not uniform. The length of our device is relatively short, so we do not expect

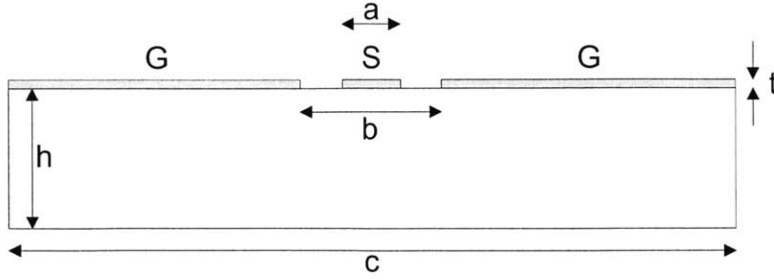

Figure 3-5: Cross section of a coplanar waveguide illustrating the various dimensions of importance. The direction of wave propagation is perpendicular to the illustrated cross section.

to encounter these secondary effects.

3.4 Transmission Line Design

The device layout must be incorporated in a transmission line design which serves as the electromagnetic propagation medium between the network analyzer/probes and the device. The device is connected in a common-emitter configuration which is used when the HBT functions as an amplifier. Therefore, the emitter electrode should be connected to the ground (G), and the signal (S) is connected to the base and the collector electrode.

The coplanar waveguide (CPW), illustrated in Fig. 3-5, was the transmission line of choice. It offers several advantages compared to a microstrip line [66]. The ground plane and the signal line are easily accesible and vias are not required. It is a planar structure and the characteristic impedance is determined mostly by the photolithographically defined dimensions a, b, c and the metal thickness t. Furthermore, the variation of the substrate thickness does not affect much the propagation characteristics. It exhibits relatively low dispersion and radiation losses. The coplanar waveguide shows also lower radiation losses and crosstalk than a pair of coplanar strips (G-S) since the signal line is shielded on both sides by its ground planes (G-S-G). According to [67], the characteristic impedance Z_0 and the effective permittivity ε_{eff} can be expressed in closed forms:

$$Z_0 = \frac{30\pi}{\sqrt{\varepsilon_{\text{eff}}}\left[K\left(k_1'\right)/K\left(k_1\right) + t/(b-a)\right]}, \tag{3.5}$$

$$\varepsilon_{\text{eff}} = 1 + \frac{\left(\varepsilon_r - 1\right)\left[K\left(k_2'\right)/K\left(k_2\right)\right]}{2\left[K\left(k_1'\right)/K\left(k_1\right) + t/(b-a)\right]}, \tag{3.6}$$

where $k_1 \equiv (c/b)\sqrt{(b^2-a^2)/(c^2-a^2)}$, $k_2 \equiv \sqrt{(1-\lambda_1^2)/(1-\lambda_2^2)}$, $k_n' \equiv \sqrt{1-k_n^2}$, n=1,2, $\lambda_1 \equiv \sinh\left[\pi a/(4h)\right]/\sinh\left[\pi b/(4h)\right]$, $\lambda_2 \equiv \sinh\left[\pi a/(4h)\right]/\sinh\left[\pi c/(4h)\right]$, and $K(x)$ is the complete elliptic integral of the first kind. When $c > 5b$, the finite ground extension behaves similarly to an infinite ground plane. If this condition holds and $h \gg b$, Z_0 is determined approximately by the ratio a/b

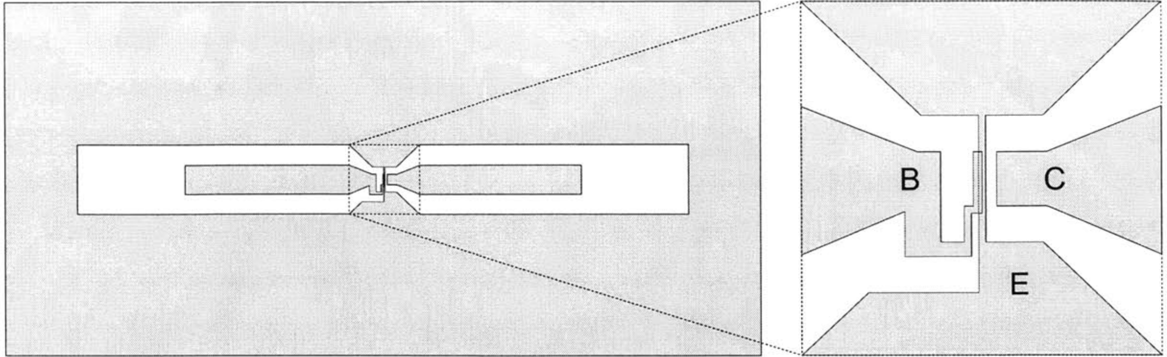

Figure 3-6: Top view of the coplanar waveguide and the HBT in a common-emitter configuration. The dashed rectangle includes the transition area between the coplanar waveguide and the HBT, and the various details are shown magnified. The ratio a/b is kept constant along most of the coplanar waveguide for a uniform Z_0.

and the metal thickness t.

The useful coplanar waveguide mode is often called the odd mode of the waveguide. It can be excited if a source wave is launched with a vector voltage $V_{ex} = \left[\begin{array}{ccc} -V_1 & 0 & -V_1 \end{array} \right]$, where $V_{ex} \equiv \left[\begin{array}{ccc} V_{G,Left} & V_S & V_{G,Right} \end{array} \right]$. Unfortunately, there exist other modes that contribute to the power loss and the dispersion characteristics of the launched signal [68, 69]. Another mode is the slotline mode which is often called the even mode of the waveguide. It can be excited if a source wave is launced with a vector voltage $V_{ex} = \left[\begin{array}{ccc} -V_1 & 0 & V_1 \end{array} \right]$. From this expression, we can easily deduce that the even mode can be suppressed if the two ground planes are connected to each other. Furthermore, the finite substrate thickness gives rise to other wave modes. These are the parallel plate modes if there exists a back-side ground plane. When there is no back-side ground plane, these are called dielectric slab modes or surface modes. The criterion for the excitation of only the first parallel plate or surface mode is rather strict, $h < 0.1\lambda_d$, where λ_d is the wavelength of the propagated signal in the substrate. However, when $b \ll h$ and $b \ll \lambda_d$, the useful odd mode interacts weakly with the parallel plate and surface modes and the dispersion effects are limited.

The impedance of the G-S-G probes of the network analyzer is 50 Ω. The coplanar waveguide design must ensure good impedance matching. A poor impedance matching causes unwanted signal reflections that deteriorate the accuracy of microwave/millimeter wave measurements. The footprint of the signal probe is about 20 μm wide, and this sets a lower limit of the signal width a. Pad parasitics are significantly reduced when the signal width is relatively small. We have chosen the dimensions a=40 μm, b=98 μm, c=498 μm, and $h \approx 500$ μm for the coplanar waveguide of our design in order to achieve a $Z_0 \approx 50$ Ω. The pair of the G-S-G probes must be separated by a distance greater than 200-300 μm to avoid probe cross talk. In addition, a length of a least 70 μm must be included to account for the probe skating. We have dedicated a length 80 μm for probe

scating and an additional length of 150 μm of constant a/b ratio between the probe pad and the device area.

An advantage that the coplanar waveguide design offers is the flexibility of the chosen ratio a/b. The dimensions of the active device are usually small. Signal reflections are significantly minimized if the signal width a narrows smoothly to the device dimension while keeping the same a/b and Z_0. In our design illustrated in Fig. 3-6, we have dedicated a transition area of length 100 μm between the input and output signal lines. The base and collector signal lines narrow from 40 μm to 15 μm in width. The collector transition is optimum since the final signal width of the collector coincides with the collector width of the active device. On the other hand, the base transition is not ideal. This is due to the fact that the base width of the active device is very small (2 μm). In addition, the base transition layout is dictated by the active device isolation technique that was employed in the fabrication process. We will focus later on the details of the active device isolation. Given this layout restriction, we decided to adopt a base-collector transition as symmetrical as possible.

3.5 On-Wafer Calibration Structures

At microwave and millimeter wave frequencies, the measurements taken by the network analyzer are prone to errors [70]. They are usually classified as systematic, random, or drift errors. The systematic errors are due to non-idealities such as leakage, signal reflections, and frequency response. The signal leakage causes directivity and crosstalk errors. The signal reflections are associated with the source and load impedance mismatches. The frequency response errors stem from the reflection and transmission tracking in the test receivers. If these errors do not change over time, they can be estimated during the calibration process of the network analyzer and the measurements can be corrected accordingly. The random errors change over time and they originate from the noise of the network analyzer. The calibration can not account for this type of errors. The drift errors originate from any temperature variation. The calibration should be repeated periodically to account for drift errors.

The systematic errors of the network analyzers can be modeled as a pair of two-port devices, A and B, connected to the input and output of the device under test (DUT)[71, 72, 73]. This is illustrated in Fig. 3-7. The aim of the calibration process is to estimate the scattering matrices $\overline{\overline{S}}_A$ and $\overline{\overline{S}}_B$. Therefore, the actual scattering matrice $\overline{\overline{S}}$ of the DUT can be found from the relation $\overline{\overline{S}} = \overline{\overline{S}}_A{}^{-1}\overline{\overline{S}}_m\overline{\overline{S}}_B{}^{-1}$, where $\overline{\overline{S}}_m$ is the measured scattering matrice.

The extraction of the scattering matrices $\overline{\overline{S}}_A$ and $\overline{\overline{S}}_B$ is achieved if we substitute the DUT with simple structures of well known scattering matrices. The TRL calibration stands for Through-Reflect-Line calibration method. The input and output port are connected via a short length $2L_0$ of transmission line for the Through standard. The scattering parameters of the Through standard

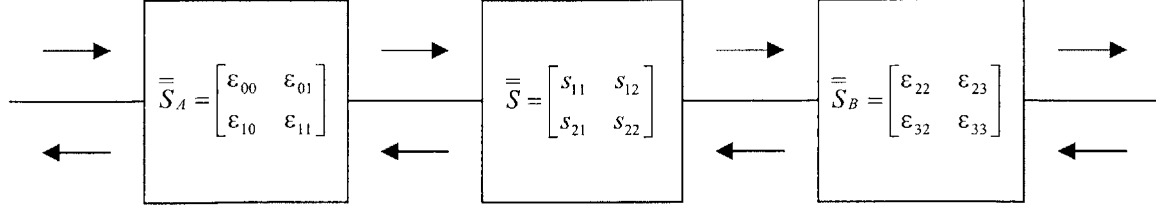

Figure 3-7: Representation of the network analyzer systematic errors as a pair of two-port devices, A and B, at the input and output of the device under test. The TRL calibration resolves the scattering parameters of A and B and estimates the reflection coefficient of the Reflect standard and the propagation constant of the Line standard.

are s_{11}=s_{22}=0, and s_{12}=s_{21}=$\exp(-2\gamma L_0)$, where γ is the propagation constant. The input and output port are connected to a highly reflective structure via a short length L_0 of transmission line for the Reflect standard. We use a short or an open circuit and we conduct one-port measurements for both the input and output port. Consequently, the scattering parameters of the Reflect standard are s_{11}=s_{22}= $\rho_L \exp(-2\gamma L_0)$. For the Line standard, we connect the input and output port with a transmission line of length $L_1 + 2L_0$. The scattering parameters of this standard are s_{11}=s_{22}=0, and s_{12}=s_{21}=$\exp[-\gamma(2L_0 + L_1)]$. The characteristic impedance Z_0 of the transmission lines used for the Through, Reflect, and Line must be the same. The TRL calibration consists of ten measurements (four measurements for the Through, two measurements for the Reflect, four measurements for the Line). The unkown parameters are also ten: eight error scattering parameters, the reflection coefficient ρ_L, and the propagation constant γ. Therefore, the calibration is complete.

From the above discussion, it becomes clear that the LINE standard gives the same information as the THROUGH standard for a frequency point where $\exp(-\gamma L_1) = \pm 1$. The number of linearly independent equations becomes six while the number of unknown parameters remains ten. Therefore, the TRL calibration becomes ill-conditioned. For lossless lines, $\gamma = j\beta \equiv j(2\pi/\lambda_g)$, where $\lambda_g \equiv 1/(f\sqrt{\mu_0\varepsilon_0\varepsilon_{r,\text{eff}}})$ is the guided wavelength. The condition $\exp(-\gamma L_1) = \pm 1$ occurs when L_1 is an integer multiple of $\lambda_g/2$, or equivalently when the phase $\varphi \equiv \beta L_1$ is an integer multiple of π radian. A rigorous numerical error analysis of the TRL calibration leads to the conclusion that the error in the computation of the s-parameters is proportional to $1/|\sin(\varphi)|$ [74]. The minimum error occurs when φ is an odd multiple of $\pi/2$ and as expected, the error becomes infinite when φ is an integer multiple of π radian. A common design rule adopted by many microwave engineers is to allow $\pi/9 \leq \varphi \leq 8\pi/9$. The expected error at the band edges is approximately 2.92 times higher that the error at $\varphi = \pi/2$. The minimum and maximum frequency where the calibration is valid, is determined by demanding $\varphi = \pi/9$ and $\varphi = 8\pi/9$, respectively. Consequently, $f_{\text{min}} = 2f_{\text{opt}}/9$, $f_{\text{max}} = 16f_{\text{opt}}/9$, and $f_{\text{opt}} = 1/4L_1\sqrt{\mu_0\varepsilon_0\varepsilon_{r,\text{eff}}}$. If we wish to expand the frequency range, multiple Line standards must be used. From the expression of f_{opt}, it becomes evident that the length of

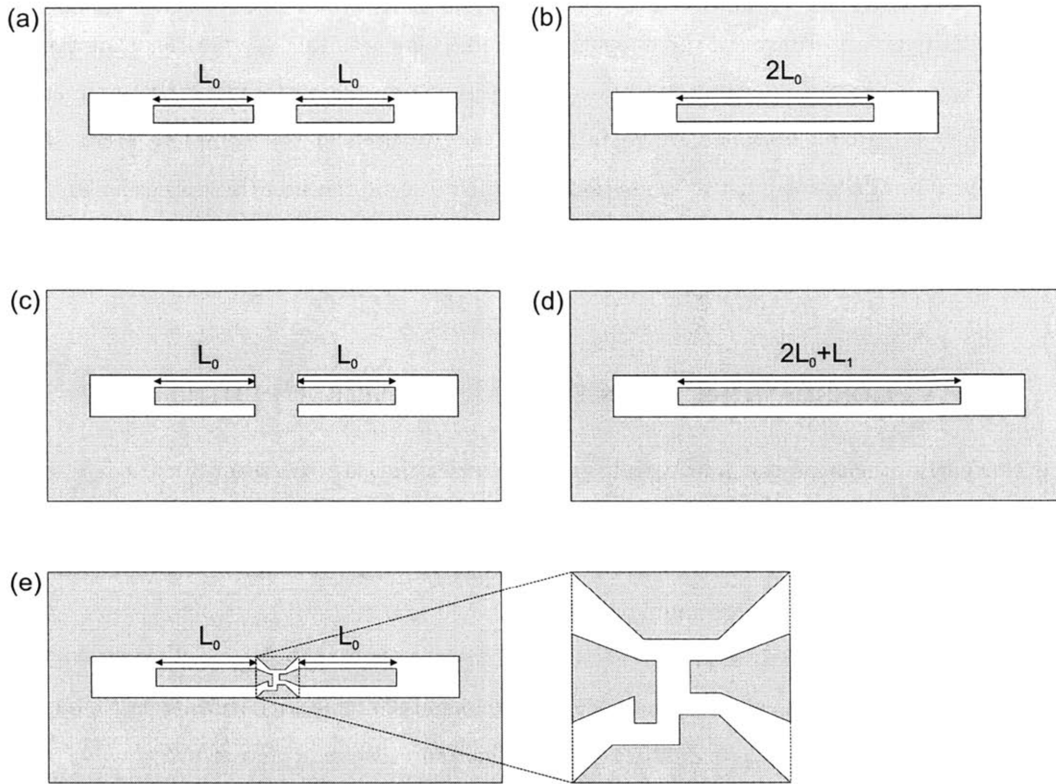

Figure 3-8: On-wafer coplanar waveguide structures for the TRL calibration: (a) open, (b) through, (c) short, and (d) line calibration standard. The length L_1 is chosen according to the frequency region of interest. Multiple line standards can be used for a broader frequency range. The TRL calibration brings the calibration planes at the beginning of the transition region. The open structure (e) is used for the de-embedding of the transition region.

the Line standard must be very large if we wish to take low frequency measurements. This is one of the disantantages of the TRL calibration. Large coplanar waveguides take significant space and they are also prone to undesirable odd modes. This problem is not serious if we are interested in high frequency measurements. There exist other calibration methods that are more suitable for a low frequency range. The disadvantage of these methods is that they require a precise load resistor of Z_L=50 Ω for the LOAD standard.

The TRL calibration structures of our design are shown in Fig. 3-8(a)-(d). The length L_0 is 230 μm (80 μm for probe scating plus 150 μm for reduced crosstalk between the probes). For our design, we selected 20 GHz, 40 GHz, and 60 GHz as optimum calibration frequencies. The frequency span for each Line standard is 4.4 $\rightarrow$ 35.6 GHz, 8.9 $\rightarrow$ 71.1 GHz, and 13.3 $\rightarrow$ 106.7 GHz, respectively. For $\varepsilon_{r,\text{eff}} \approx 6.9$, the Line standard must be 1427 μm, 713 μm, and 476 μm, respectively. Prior to the TRL calibration, the planes of measurement are located at the probe tips and the measurements are corrupted by systematic errors. After the TRL calibration, the planes of measurement are located

at the beginning of the transition region shown in Fig. 3-6, and the measurements are not affected by the systematic errors. However, the transition region adds parasitic capacitances that can not be neglected. We can take into account the effect of the transition region by using the open structure in Fig. 3-8(c). It can be obtained by removing the active area of the complete HBT structure shown in Fig. 3-6. Therefore, if the transition region can be represented by an equivalent circuit, the measurements can be further corrected, reflecting solely the high frequency performance of the active device.

3.6 CPW Losses and Effective Dielectric Permittivity

During the early stages of the fabrication process, we fabricated the on-wafer TRL calibration standards for de-embedding purposes of future high-frequency measurements, and we evaluated the coplanar waveguide losses and the effective dielectric permittivity. The de-embedded S-parameters of the HBT are not affected by the line losses.

We verified the OPEN, SHORT, and THROUGH standards for the frequency range 6-50 GHz. The reflection coefficient ρ_L of a load Z_L connected to transmission line with characteristic impedance Z_0 is given simply by $\rho_L \equiv (Z_L - Z_0)/(Z_L + Z_0)$. Therefore, we expect $S_{11} = S_{22} = \rho_L = 1$ and $S_{12} = S_{21} = 0$ for the OPEN standard ($Z_L = \infty$ and isolation between port 1 and port 2), $S_{11} = S_{22} = \rho_L = -1$ and $S_{12} = S_{21} = 0$ for the SHORT standard ($Z_L = 0$ and isolation between port 1 and port 2), and finally $S_{12} = S_{21} = 1$ and $S_{11} = S_{22} = 0$ for the THROUGH standard (match between port 1 and port 2). The measured S-parameters of the OPEN, SHORT, and THROUGH standards are shown in Fig. 3-9, and the anticipated values were approximately reached. Slight deviations from the expected S-parameters originate from the moderate quality of the probes and the difficulty to probe accurately all the calibration standards at equal distances from the beginning of the signal line. Therefore, the calibration is prone to small phase errors.

The effective permittivity and the loss of a coplanar waveguide of length L can be extracted if we utilize the expressions of S_{12} and S_{21}. Specifically, $S_{12} = S_{21} = \exp(-\gamma L) = \exp(-\alpha L) \times \exp(-j\beta L)$, where $\gamma \equiv \alpha + j\beta$, $\alpha \equiv \mathrm{Re}(\gamma)$ represents the attenuation per unit length, and $\beta \equiv \mathrm{Im}(\gamma) = \omega\sqrt{\mu_0\varepsilon_0\varepsilon_{r,eff}}$ is the propagation constant. Thus, the relative effective permitivity $\varepsilon_{r,eff}$ and the attenuation per unit length A (db/mm) can be found from $\varepsilon_{r,eff} = \left[\angle S_{12}/\left(2\pi f L\sqrt{\mu_0\varepsilon_0}\right)\right]^2$ and $A = -20\log_{10}(|S_{12}|)/L$, respectively. The S-parameters of a line were measured and the extracted values of A and $\varepsilon_{r,eff}$ are shown in Fig. 3-10 for the frequency range 10-40 GHz. The losses are within the range 0.4-0.6 db/mm and $\varepsilon_{r,eff} \approx 6.5$. The total losses (dielectric and conductor) of a CPW with the same planar dimensions were estimated to be within the range 0.25-0.30 db/mm [75]. The discrepancy can be attributed to the presence of doped layers under the signal line and the ground plane. These MBE grown layers increase the dielectric losses. The relative effective

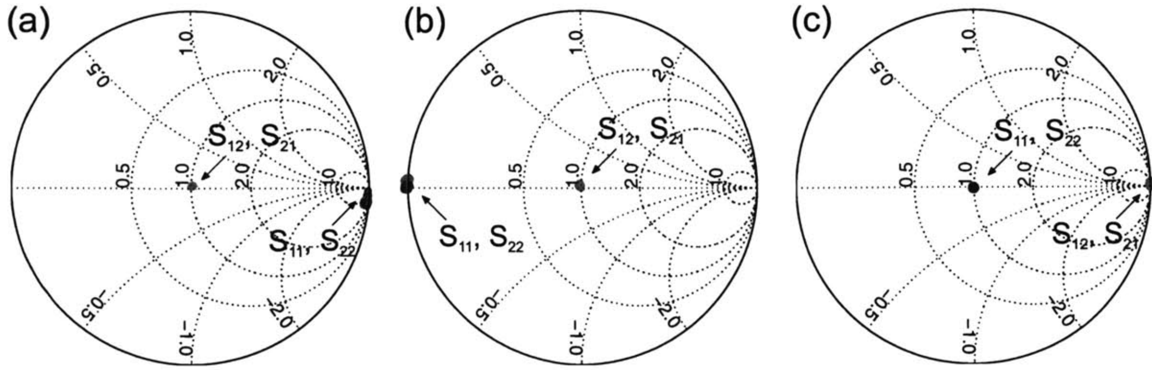

Figure 3-9: Smith charts showing the measured S-parameters of the (a) OPEN, (b) SHORT, and (c) THROUGH on-wafer calibration standards for the frequency range 6-50 GHz.

permittivity of a CPW with the same planar dimensions was estimated to be about 6.8 [75]. We could explain this deviation from the non-zero height between the metal layer and the exposed semi-insulating layer. For a common CPW, the electric field is distributed between the substrate and the air, yielding the average value $\varepsilon_{r,eff} \approx (\varepsilon_r + 1)/2$, where ε_r is the relative dielectric permittivity of the substrate. Due to the presence of the device mesa, a larger portion of the electric field is distributed in the air, lowering the value of $\varepsilon_{r,eff}$. The small feature shown in the vicinity of 23 GHz for both the loss and the relative effective permittivity can be attributed to an error due to the change of LINE standard of the TRL calibration at this frequency.

3.7 Device Isolation

The device isolation is an essential fabrication step for the definition of the active device area. The advantages of a fine photolithographic process can be severely overshadowed by an ineffective device isolation. A well-defined active area is characterized by low parasitic capacitances and low device crosstalk. The choice of the device isolation scheme affects significantly the fabrication sequence and the fabrication cost.

There are three commonly employed isolation processes [76]. In the first method shown in Fig. 3-11(a), the interconnects run over the edge of the device mesa. The edge is covered by a dielectric film to avoid an electric short between different device layers. However, a fine photolithography along the mesa edge cannot be easily achieved. Furthermore, the deposition and etching of the dielectric films degrade the active layers and a pinhole in the dielectric may result in an electric short between active layers. In the second method illustrated in Fig. 3-11(b), a dielectric layer covers the device mesa and interconnects are formed through openings of the dielectric by either electroplating or evaporation. Large areas are usually required for the interconnects and the parasitic capacitances are high. In

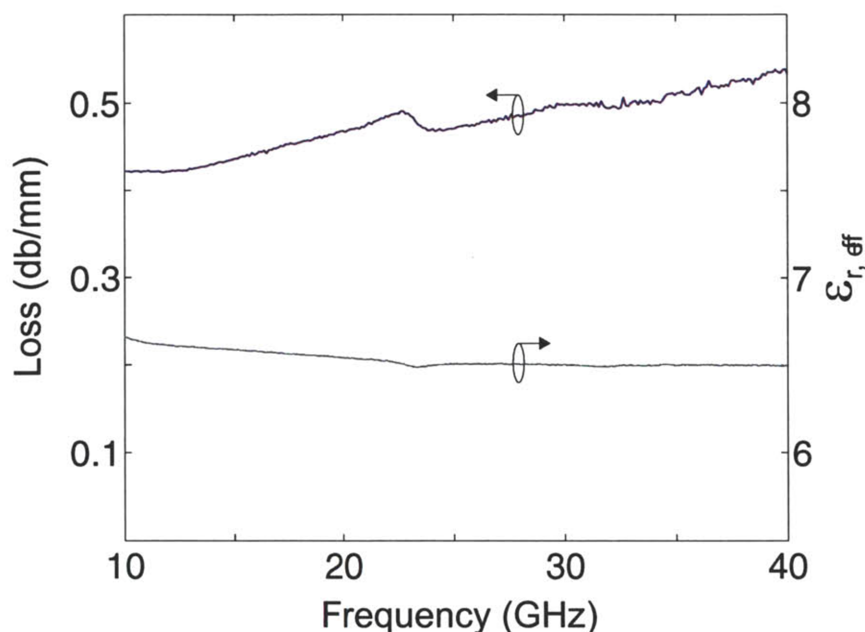

Figure 3-10: Measured values of the CPW loss and the relative effective permittivity for the frequency range 10-40 GHz. The loss is higher than expected due to the presence of the doped layers under the signal line and the ground plane of the CPW. The relative effective permittivity is slightly lower than expected due to the non-zero height between the metal layer and the exposed semi-insulating substrate.

addition, the fabrication process is relatively elaborate. In the third method shown in Fig. 3-11(c), deep ion implantation is used [77, 78]. The ion bombardment introduces midgap electron and hole traps. Therefore, charge carriers of both n and p type material can be easily trapped and the semiconductor appears highly resistive. The advantage of this method is that planar devices can be realized and the subsequent fabrication steps are much easier. There are however, some important issues to consider. The isolation of devices with active thickness less than 1 μm, usually requires multiple O^+ implantations with maximum energy in the range of 200 keV and doses in the range of 10^{15} cm^{-3}. For devices with thickness more than 2 μm, a large number of ion implantations is required or a single one of high energy (5 MeV). Consequently, the fabrication cost increases enormously. Moreover, ion implantation must be the first step in the fabrication process. A mask should be used to protect the active areas for ion implantation. It usually comprises of dielectric, metal, and photoresist layers and its removal is not trivial. The annealing temperature following the implantation is often high (700 °C) and Be outdiffusion can take place. Lighter ions such as H^+ require very low annealing temperature ($<$ 300 °C). However, alloyed ohmic contacts may require higher annealing temperature and the trap density can decrease dramatically.

An inexpensive and straightforward device isolation method is the formation of micro-airbridges by wet etching at the end of the fabrication process [76, 79, 80, 81, 82, 83]. This method was chosen

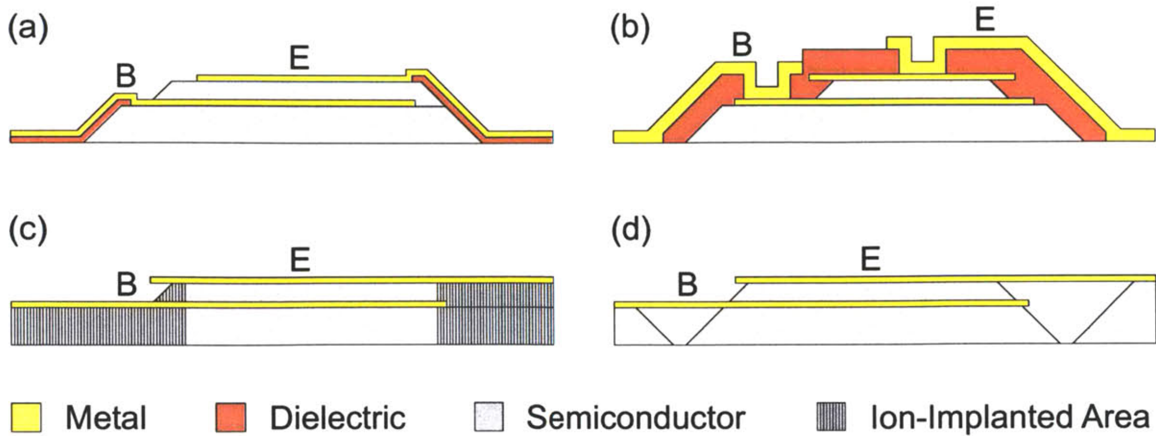

Figure 3-11: Cross sections of the HBT showing the different device isolation methods: (a) electrodes over the edge of the device mesa covered by a dielectric film, (b) electroplated electrodes contacting the device via openings of a dielectric layer, (c) planar electrodes for an active device defined by deep ion imlantation, and (d) micro-airbridges formed by deep wet etching. For (a)-(d), an emitter-up configuration is considered, the right electrode is for the emitter, the left electrode is for the base, and the substrate is semi-insulating.

for this work and it is illustrated in Fig. 3-11(d). The undercut formed around a metal surface during wet etching is often viewed as a undesirable feature. Dry etching offers high aspect ratios and it is attractive for many applications. However, the undercut offers a unique advantage. It can isolate an active device and it allows an electric contact of the device layers via short micro-airbridges. Nevertheless, there are several design issues that have to be addressed. The micro-airbridges should be relatively short, in the range of 5-10 μm, for good mechanical stability. They should also be thin so that the undercut needed is relatively small and the wet etch is moderate, in the range of 1.5-2 μm. The active device area must be protected by photoresist and the design should account for the photoresist undercut. In addition, this device isolation must be the last step since any subsequent process will result in breaking the fragile micro-airbridges.

Given the above guidelines, we can think of many micro-airbridge designs. Some of them are illustrated in Fig. 3-12. The emitter and base micro-airbidges are parallel to [0 1 1] in Fig. 3-12(a). If the wet etching is efficient for this orientation, this design is relatively simple. The disadvantage of this approach is that the emitter is connected to the ground plane from only one side and parasitic coplanar waveguide modes can emerge. In Fig. 3-12(b), the emitter and base micro-airbidges are parallel to the [0 1 1] and the emitter is connected to the ground from both sides. The only difficulty this design introduces is that the wet etching must be relatively deep to account for the width $W_E + W_B$ of the emitter and base micro-airbidge since there is no separation between them. In Fig. 3-12(c), the emitter and base micro-airbridges are in perpendicular directions and the emitter micro-airbridge is connected to the ground plane from both sides. Such a design is feasible if the

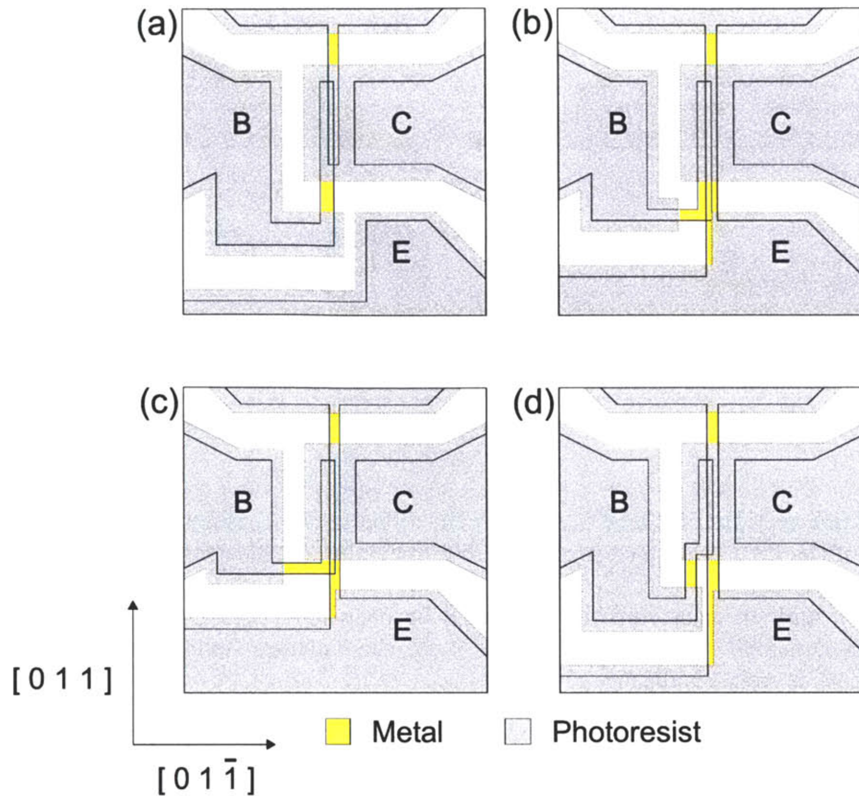

Figure 3-12: Different micro-airbridge designs illustrating the device electrodes (yellow) and the photoresist (grey) prior to wet etching: a) the emitter and base micro-airbridges are parallel to [0 1 1], and the emitter is connected to the ground from only one side, b) the emitter and base micro-airbridges are parallel to [0 1 1] with no separation, and the emitter is connected to the ground from both sides, c) the emitter and base micro-airbridges are perpendicular to each other, the emitter micro-airbridge is parallel to [0 1 1], and the emitter is connected to the ground from both sides, d) the emitter and base micro-airbridges are parallel to [0 1 1] with a non-zero separation, and the emitter is connected to the ground from both sides.

wet etching is equally efficient in both directions. The design in Fig. 3-12(d) combines some of the features of the previous designs. The emitter amd base micro-airbridges are parallel to [0 1 1], the emitter is connected to the ground from both sides and there is a non-zero separation between the emitter and base micro-airbridge. At the beginning of the base micro-airbridge, there is a small section that is perpendicular to the major axis. However, an undercut can be created from the combined effect of the etching along the main base micro-airbridge and the etching from the left side of the device.

We designed a set of 2 μm$\times$ 8 μm test micro-airbridges. We used two different solutions: (1) 30 ml H_3PO_4 : 10 ml H_2O_2 : 500 ml H_2O, and (2) 10 ml NH_4OH : 4 ml H_2O_2 : 500 ml H_2O. The etched depth was about 2 μm. We took various pictures using a Scanning Electron Microscope (SEM), and some of them are shown in Fig. 3-13. The solution (1) was used in Fig. 3-13(a),(b),

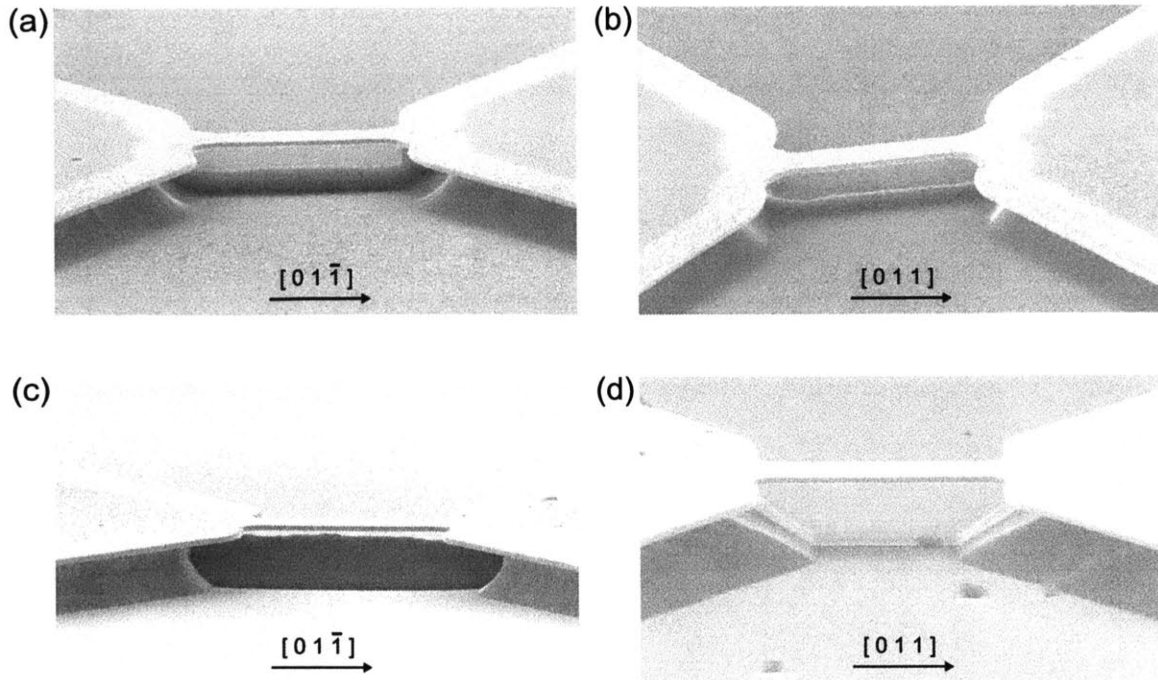

Figure 3-13: SEM pictures of 2 μm× 8 μm test micro-airbridges. In (a) and (b), the solution 30 ml H_3PO_4 : 10 ml H_2O_2 : 500 ml H_2O was used. In (c) and (d), the solution 10 ml NH_4OH : 4 ml H_2O_2 : 500 ml H_2O was used. The micro-airbridge is parallel to $[0\ 1\ \bar{1}]$ in (a) and (c), and parallel to [0 1 1] in (b) and (d). The etched depth is about 2 μm. Device isolation can be achieved in (a) and (b) if the etched depth is much larger than 2 μm and the (c) choice does not appear suitable. Device isolation can be easily achieved in (d).

and the solution (2) was used in Fig. 3-13(c),(d). The major flat is perpendicular to the major flat in Fig. 3-13(a),(c) and parallel to the major flat in Fig. 3-13(b),(d). From Fig. 3-13(a),(b) the etching appears isotropic and the device isolation may be realized if the etched depth is larger. The micro-airbridge in Fig. 3-13(c) is not recommended since the undercut is not substantial. The most suitable choice is shown in Fig. 3-13(d) as the semiconductor material underneath the micro-airbridge is almost completely etched away. Therefore, the design illustrated in Fig. 3-12(d) fulfills the need for device isolation and was chosen for this work.

3.8 Fabrication Steps

The HBT fabrication process of this work is complicated and time consuming. The small dimensions of the layout and the self-aligned architecture contribute mostly to the fabrication complexity. Overall, the HBT process includes 7 photolithographic steps, 3 metal evaporations, 4 wet etching processes, 2 dry etching processes, and 1 chemical vapor deposition. The various steps of the fabrication are illustrated in Fig. 3-14 where only the most important area of the HBT layout is shown.

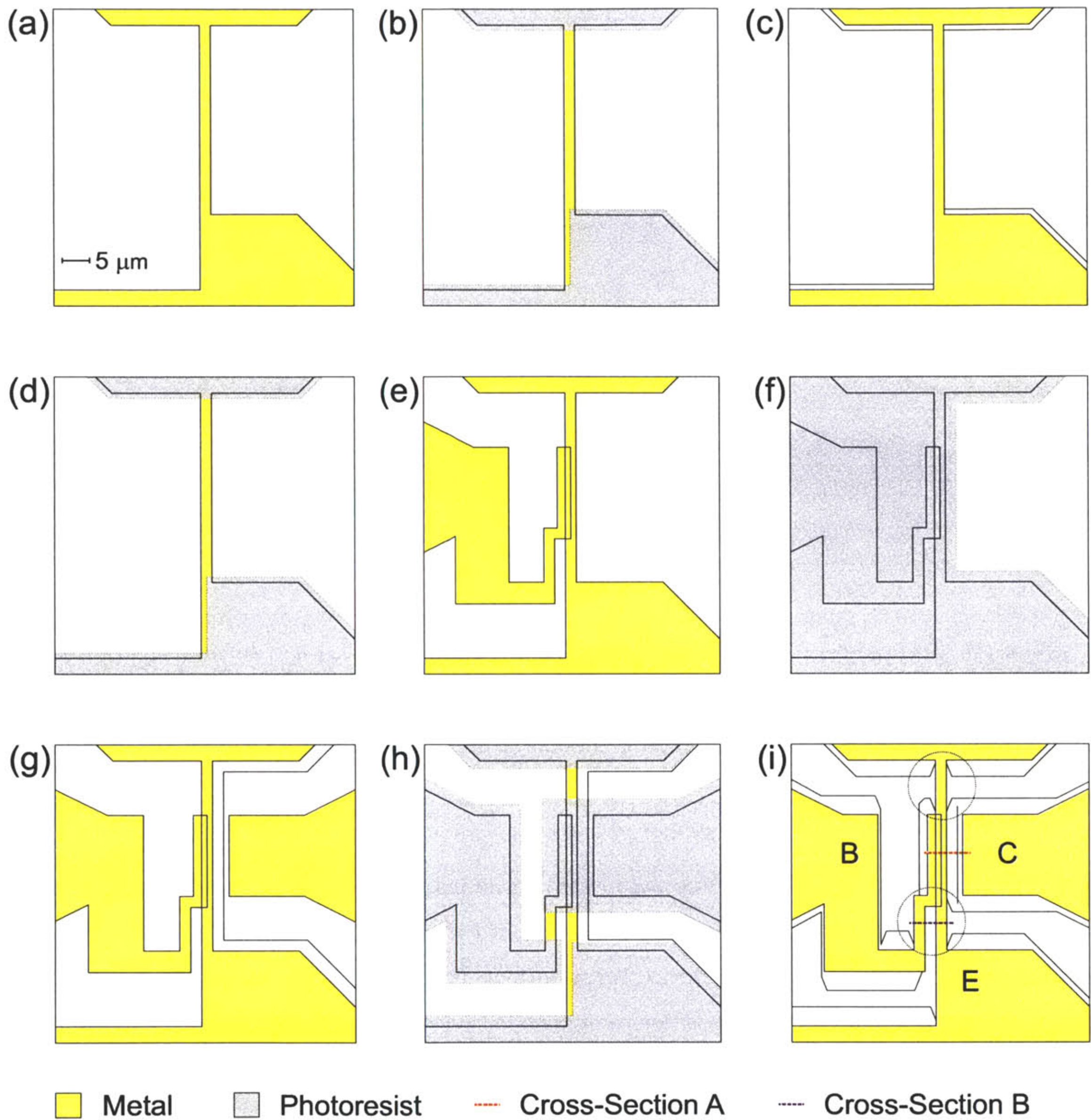

Figure 3-14: Steps of the HBT fabrication: (a) emitter metal deposition, (b)photoresist application on the emitter metal for the reduction of the galvanic effect, and wet etching, (c) ECR-CVD deposition of Si_3N_4 and directive RIE etching of Si_3N_4 for sidewall passivation, (d) photoresist application on the emitter metal for the reduction of the galvanic effect, and wet etching until the base is exposed, (e) base metal deposition, and RIE etching of the base and collector, (f) photoresist application on most of the device piece, and wet etching of the area where the subcollector metal will be deposited, (g) subcollector metal deposition, (h) photoresist application to define the active device area and reduce the galvanic effect, and deep wet etching. After the removal of the photoresist, the emitter and base micro-airbridges are revealed as shown in the dotted circles of (i), and the HBT fabrication is complete. The cross-sections A and B are utilized in Fig. 3-15 and Fig. 3-16.

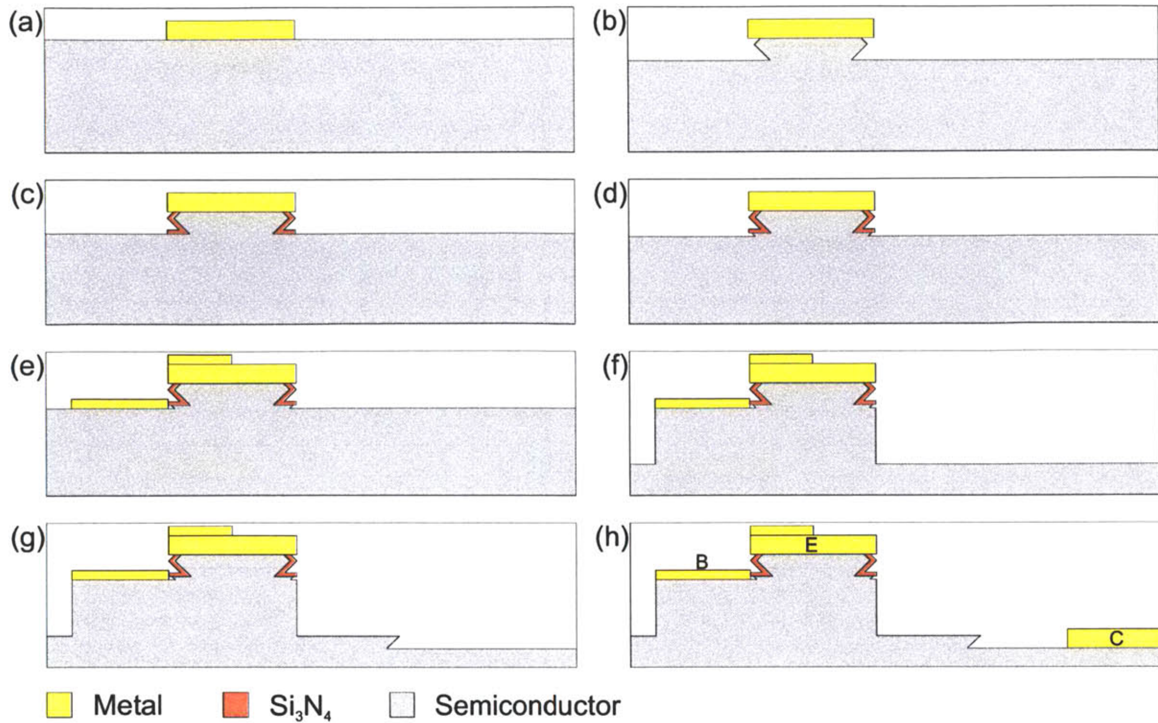

Figure 3-15: Device profile during the HBT fabrication process (cross-section A of Fig. 3-14): (a) emitter metal evaporation, (b) isotropic and anisotropic wet etching for the formation of the emitter mesa, (c) sidewall deposition of Si_3N_4, (d) shallow wet etching for the removal of the damaged surface due to the RIE process, (e) base metal evaporation, (f) dry etching until the subcollector is exposed, (g) shallow wet etching for the removal of the damaged surface due to the RIE process, and (h) subcollector metal evaporation. The last step of the device isolation (after step (h)) does not affect the device profile of this cross-section.

The device profile and the profile of the emitter and base micro-airbridges during the HBT fabrication process are illustrated in Fig. 3-15 and Fig. 3-16, respectively. In the following discussion, we will highlight some important aspects of every step. Throughout the time of this work, we had to revise our process and modify our mask to meet the challenges of the HBT process. We will describe intitial unsuccessful approaches and the solutions we implemented to resolve fabrication problems. All the details of the fabrication flow are presented in Appendix A.

3.8.1 Device Wafer Cleaving

Our MBE grower provided us with 2-inch device wafers. Every device wafer is cleaved in 6 cm × 6 cm pieces. Each piece can yield up to 15 devices. Although the active device is only 2 μm × 15 μm, most of the device area is utilized for the coplanar waveguide structure. A complete device occupies 1060 μm × 498 μm, and the spacing between neighboring devices is 300 μm for reduced crosstalk. The time and the cost of the fabrication process could have been significantly reduced

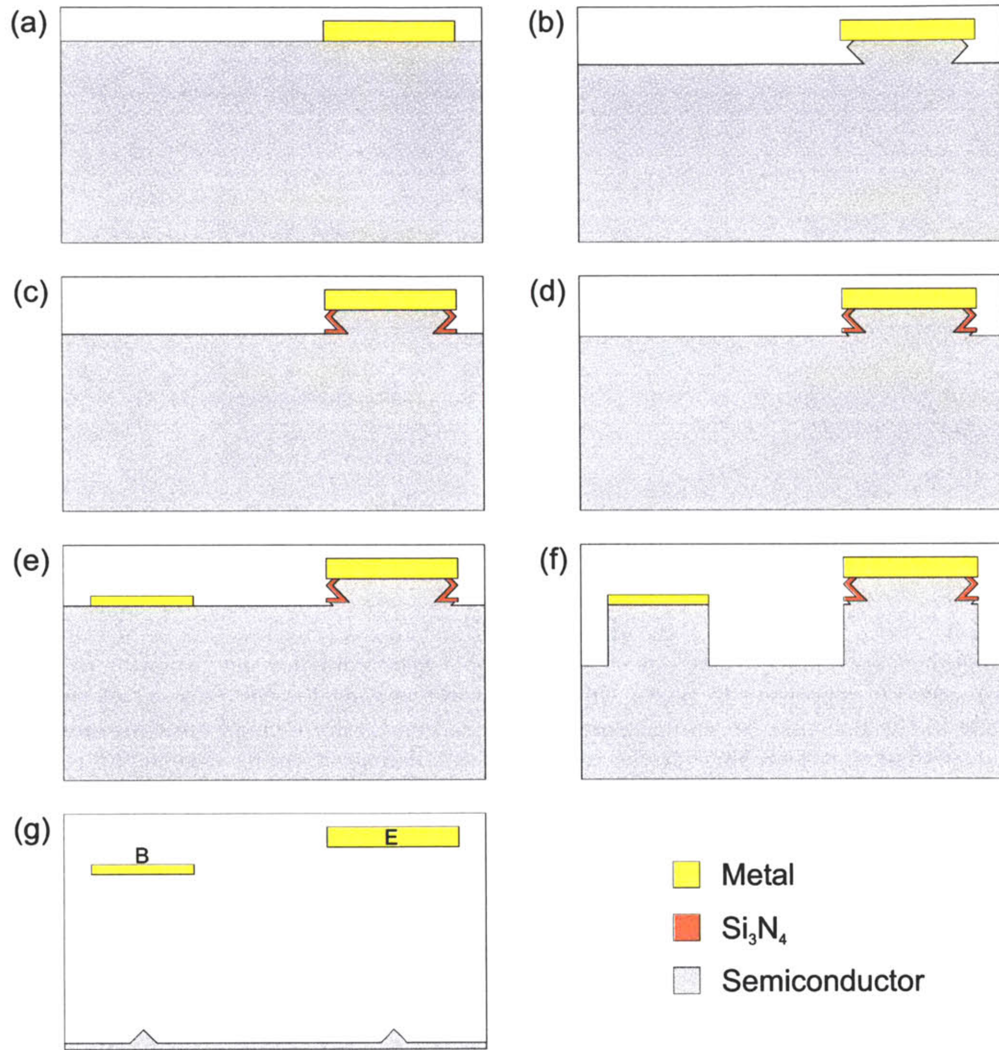

Figure 3-16: Profile of the emitter and base micro-airbridges during the HBT fabrication process (cross-section B of Fig. 3-14): (a) emitter metal evaporation, (b) isotropic and anisotropic wet etching for the formation of the emitter mesa, (c) sidewall deposition of Si_3N_4, (d) shallow wet etching for the removal of the damaged surface due to the RIE process, (e) base metal evaporation, (f) dry etching until the subcollector is exposed, (g) device isolation by deep wet etching and formation of micro-airbridges. The shallow wet etching for the removal of the damaged surface due to BCl_3 etching and the subcollector metal evaporation (between step (f) and step (g)) do not affect the profile of the emitter and base micro-airbridges of this cross section.

if larger pieces had been selected. However, the available wafers were very limited and common mishaps of the complex HBT fabrication process can quickly reduce the available number of pieces. Furthermore, a small rotational miscalignment during the photolithography can be severe for large pieces. In addition, the etching process is very critical and should be uniform across the device area. The base layer is relatively thin and excess non-uniformity ($\geq$ 500 Å) can be detrimental for the device yield. It was observed in the early stages of the fabrication process that large pieces suffer from non-uniformity during a wet etching process. The etched depth variation across small-size pieces is in the order of 100 Å which is acceptable. This can severely increase if the piece is not carefully placed at the center of the etching solution. After we cut the pieces, we lightly scribe on the backside the direction of the major flat of the device wafer for the given convention (US or EJ). This is important since the emitter stripe must be in the [0 1 1] direction for a satisfactory device isolation according to Fig. 3-12(d).

3.8.2 Emitter Contact

The first step of the fabrication process is the photolithography for the definition of the emitter, the emitter micro-airbridge, and the ground plane of the coplanar waveguide. The most critical dimension is the width of the emitter. A thin photoresist ($\approx$ 0.6 μm) was chosen for the emitter photolithography. We found at the early stages of the fabrication that the fine features of the mask cannot be accurately transferred with thicker photoresist ($\approx$ 1.4 μm) due to the larger diffraction of the UV light ($\lambda \approx$ 320 nm) during the exposure. However, a thin photoresist cannot be used throughout the HBT fabrication process. It is characterized by low viscosity and can be highly non-uniform in the presence of mesas. This is particularly important for a successful lift-off process since the photoresist thickness at the edges of a mesa is small and acetone cannot easily penetrate. It was also observed that a thin photoresist is more sensitive to variations of the photolithographic process than a thick photoresist. Changes in the relative humidity level of the clean room, the prebake oven temperature, the hot plate temperature, and the development time can significantly affect the yield of the photolithography. We found it useful to receive feedback from SEM pictures during the development of a photoresist recipe. A 2 μm feature may turn out to be within the 1.8-2.3 μm range.

A crucial factor for a successful photolithography of the emitter is the wedge error of the mask aligner. If the mask is not in full contact with all the photoresist area, the resolution can vary widely across the surface of the processed piece. The photoresist edge around the processed piece and the random $In_xGa_{1-x}As$ protrusions on the surface contribute to high wedge error. Furthermore, the small surface area of the piece does not help the wedge error correction of the mask aligner. We resolved this problem by using a thin neoprene film underneath the piece. In this way, higher pressure can be exerted on the mask without breaking the piece and more uniform contact can be

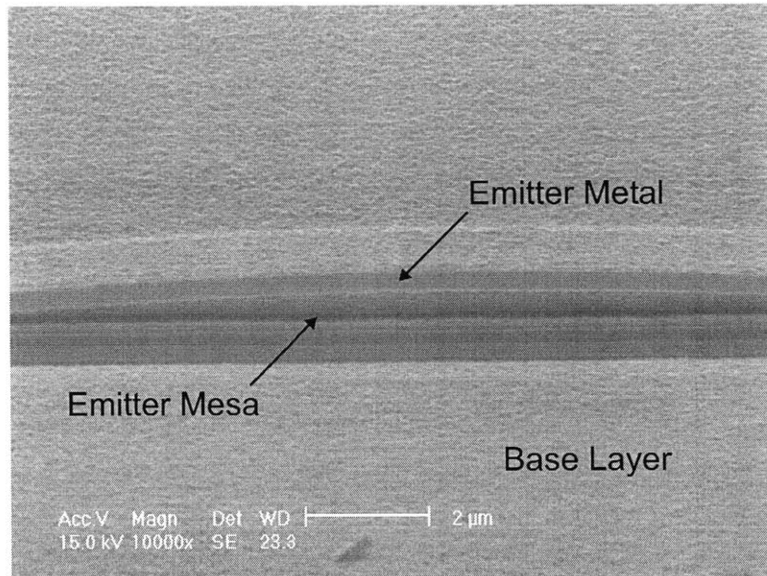

Figure 3-17: Emitter contact detachment and formation of an emitter bow during the emitter wet etching. This is the result of the galvanic effect caused by large metallic surfaces in the wet etchant.

established.

After the emitter photolithography and the native oxide removal by BOE etching, we evaporated Ti/Pt/Au. It is worth noticing that the temperature of the piece increases during the Pt evaporation. Excess Pt evaporation time can cause photoresist burning and the lift-off becomes problematic. The photoresist burning can be attributed to the high melting point of Pt in combination with the sensitivity of the thin photoresist to elevated temperatures. For a 200-500 Å Pt thickness, we did not experience this effect. We noticed that the emitter contact adhesion is poor. Therefore, ultrasonic agitation in acetone is not allowed. We found it more effective to soak the piece in acetone for a long time and later squirt generous amount of acetone with high pressure to remove any stubborn photoresist-metal areas. The resultant layout is illustrated in Fig. 3-14(a), and the important device and micro-airbridge profiles are shown in Fig. 3-15(a) and Fig. 3-16(a), respectively.

3.8.3 Emitter Wet Etching, Si_3N_4 sidewall deposition, and Base Contact

Prior to the base metal evaporation, the emitter layer must be etched in all areas except under the emitter metal. A dry etching process usually creates sharp profiles. However, the base contact must not touch either the emitter layer or the emitter contact. In a self aligned HBT, the base contact is defined by the emitter edge. Therefore, an emitter undercut created by a wet etching process is desirable. In the early stages of the fabrication process, the emitter metal was used as a natural mask of the wet etching process. However, this choice created a number of problems. The presence of a large metal surface can accelerate significantly the etching rate of the solution. A reaction-rate

limited etching depends on the available electrons for the oxidation process. When different materials and metals appear in the same solution, an electrochemical potential will be established, supplying more electrons. Therefore, the etching rate can vary widely across the device. This is a galvanic effect that can create severe undercuts, trenches, and non-uniform etched surface [84, 85, 86, 87, 88]. If the undercut is large, the adhesion of the emitter contact on the emitter cap becomes difficult and the stress of the metal surface can create complete emitter contact detachment. This can be easily seen in Fig. 3-17 where an emitter bow is formed at the end of wet etching process. We resolved this problem by covering all the emitter metal surface by photoresist with a 1 μm rim. (Fig. 3-14(b)). The only metal surface that was not covered by photoresist was a 2 μm$\times$ 35 μm of the active emitter area and the emitter micro-airbridge. Ideally, we would like to cover this metal stripe with photoresist. This is not feasible though due to the requirement for self-alignment ($S_{BE} \approx 0$) and also due to the limited alignment capabilities. We should keep in mind that the etching rate along the emitter stripe is affected mostly by the galvanic effect caused by the large exposed metal surface of the ground plane. After this photolithographic step, we noticed that the etching rate was repeatable and the undercut was acceptable.

The use of $In_xGa_{1-x}As$ as an emitter cap is ideal for a low emitter contact resistance. However, some etchants utilized for $Al_xGa_{1-x}As/GaAs$ cannot be used for an $In_xGa_{1-x}As$ layer. This makes the fabrication slightly more complicated. A common approach is to etch the $In_xGa_{1-x}As$ layer with a non-selective etchant and the emitter layer with an anisotropic etchant. There exists a variety of wet etchants for the materials of our device [89, 90]. We used the solution 30 ml H_3PO_4 : 10 ml H_2O_2 : 500 ml H_2O for the $In_xGa_{1-x}As$ layer with an etching rate of approximately 1000 Å/min [91]. Although this proved to work in most case, it was found that the etching becomes problematic in high In concentrations. It can create deep etch pits that can propagate in subsequent etching steps. This is a serious problem given the small thickness of both the emitter and base layer. We used the solution 3 ml H_2SO_4 : 3 ml H_2O_2 : 450 ml H_2O with an etching rate of approximately 500 Å/min [92]. The yield of this etchant is high. We noticed that if we move the basket that carries the device piece in the etching solution, we can initiate surface roughness and etch pits. Therefore, it is essential that the piece be well centered in the beaker and stationary.

After the $In_xGa_{1-x}As$ etching, we etch the emitter layer with the solution 10 ml NH_4OH : 4 ml H_2O_2 : 500 ml H_2O with an etching rate of about 1500 Å/min. Although the etching rate is relatively high for a good control of the etched depth, the etchant creates an inward slope if the emitter stripe is in the [0 1 1] direction of the GaAs wafer as shown in Fig. 3-18(b). This feature is favorable because it minimizes the probability of contacting the emitter layer during the base metal evaporation step. On the contrary, the slope is outward when the emitter stripe is in the [0 1 $\bar{1}$] direction as shown in Fig. 3-18(a). The etching continues up to the base layer or 100-200 Å above the base layer. A SEM picture of the emitter stripe after the two etching steps is shown in Fig. 3-19(a).

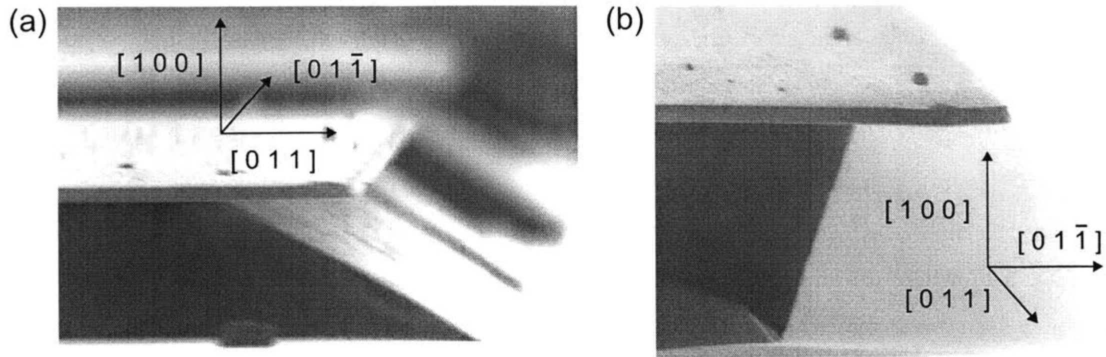

Figure 3-18: SEM pictures showing the different GaAs slopes after a wet etching process in a 10 ml NH_4OH : 4 ml H_2O_2 : 500 ml H_2O solution. In (a), the metal stripe is the [0 1 $\bar{1}$] direction and the slope is outward. In (b), the metal stripe is in the [0 1 1] direction and the slope is inward. This is the direction of the emitter contact, emitter micro-airbridge, base contact, and base micro-airbridge because it facilitates the separation of the base contact and the emitter mesa, and the device isolation.

We can clearly see the emitter cap layer that cannot be etched by the second anisotropic etch. The first etchant creates an outward slope as expected from a non-selective etchant, whereas the second etchant forms an inward slope on the $Al_xGa_{1-x}As$ emitter. It should be emphasized that the etched depth control throughout the HBT process is achieved by profilometer measurements. The mask has incorporated small size photoresist pads across the device area suitable for the profilometer. Furthermore, we perform reverse breakdown voltage measurements on the semiconductor surface using two BeCu probes and a curve tracer. The reverse breakdown voltage is a figure of merit which is sensitive to the doping level [93]. Therefore, the abrupt changes of the doping level at the emitter/base and collector/subcollector interfaces can be easily traced. The device profile and the micro-airbridge profiles are illustrated in Fig. 3-15(b) and Fig. 3-16(b), respectively.

We deposit isotropically 2000 Å of Si_3N_4 using a chemical vapor deposition system that utilizes the electron cyclotron resonance (ECR-CVD). Next, we apply a directional reactive ion etching (RIE) of the Si_3N_4 film (Fig. 3-14(c)). The result of these two steps is the formation of a sidewall Si_3N_4 layer shown in Fig. 3-19(a). This offers several advantages for the subsequent fabrication steps and the device operation. When we blow-dry the processed piece, strong forces of the nitrogen flow are applied on the emitter metal from the undercut. In the early stages of the fabrication, we noticed that this can lead to a complete emitter metal detachment. The Si_3N_4 layer provides mechanical stability because it fills the emitter material that was etched away under the emitter metal. In addition, it shields the emitter mesa from subsequent wet or dry etchants. Finally, it provides passivation to the exposed surface area minimizing the base recombination current. However, the quality of the deposited film is not ideal for a good passivation. The index of refraction of the deposited Si_3N_4 film was measured with an ellipsometer to be about 2.3 instead of the expected

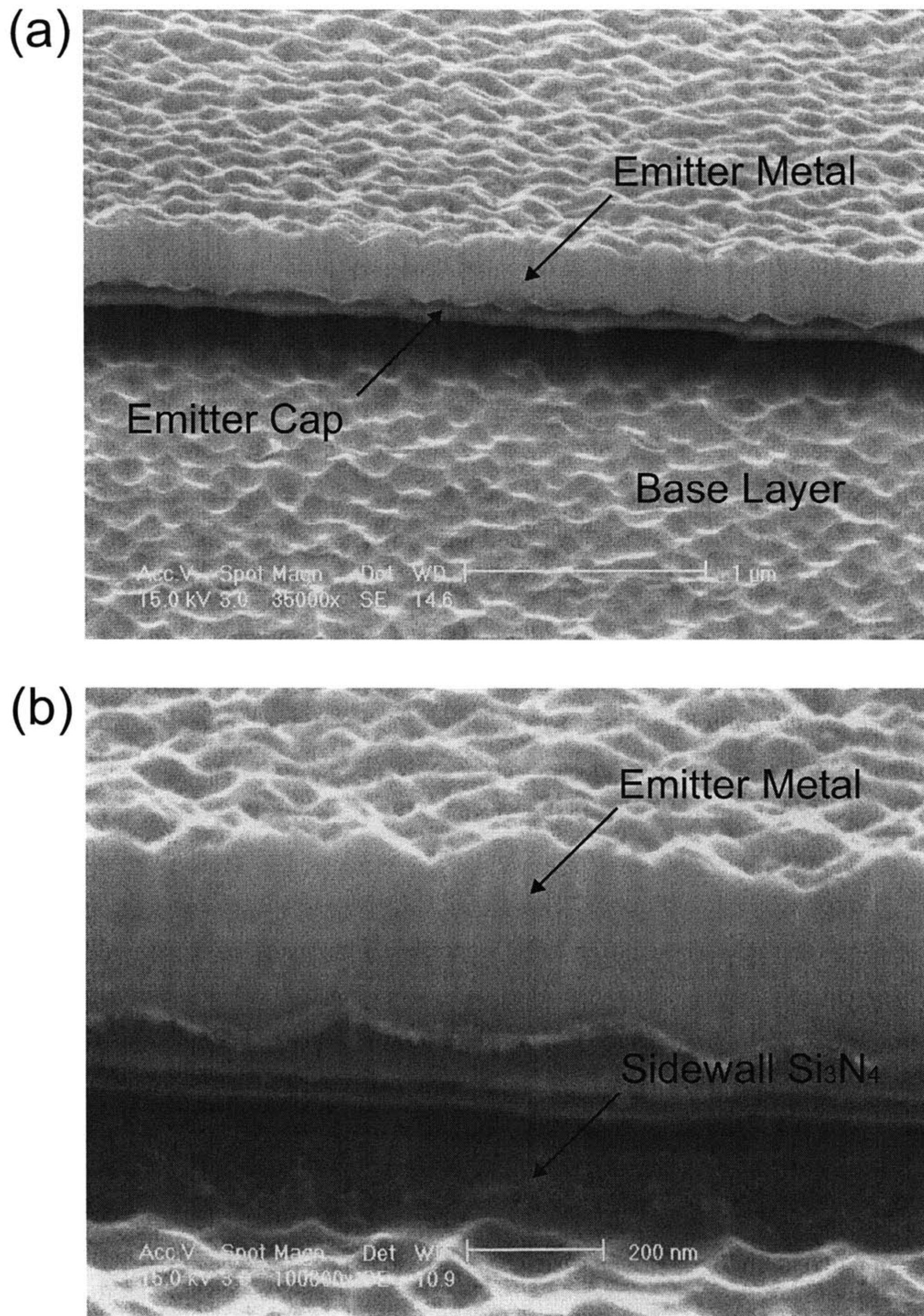

Figure 3-19: SEM pictures of the emitter after the first wet etching of the emitter cap and the emitter. The emitter area is shown in (a) and (b), prior and after the Si_3N_4 sidewall deposition respectively. The wet etching process consists of a first non-selective etchant for the emitter cap removal and a second anisotropic etchant. The Si_3N_4 sidewall deposition takes place by an isotropic Si_3N_4 deposition and a directive RIE etching of the Si_3N_4 layer.

value of 2.0. This is clearly a Si-rich and not a stoichiometric Si_3N_4 film. Moreover, the maximum temperature of the ECR-CVD chuck is about 80 °C. This should be contrasted with the ideal temperature condition of about 300 °C for a good quality Si_3N_4 layer. The device profile and the micro-airbridge profiles are shown in Fig. 3-15(c) and Fig. 3-16(c), respectively.

After the completion of the RIE process, the extrinsic base area is damaged by the etchant species (CF_4, O_2, He) [94]. The directional flow of these species under the applied RF bias introduces recombination centers that can raise the base current. In addition, there exist hydrogenation effects during the Si_3N_4 deposition [95, 96]. The hydrogen released in the ECR-CVD chamber can neutralize the emitter and base dopants. We solve these problems by performing a shallow wet etching (800-1000 Å) of the extrinsic base prior to the base metal evaporation. Another benefit of this wet etching is that we increase the separation between the exposed base surface and the emitter contact. In this way, we minimize the chance of an emitter-base short. The disadvantage of this step is that the base sheet resistance increases. We use the non-selective 3 ml H_2SO_4 : 3 ml H_2O_2 : 450 ml H_2O solution. Again, we have to cover most of the emitter metal surface with photoresist in order to minimize the galvanic effect during wet etching. This is shown in Fig. 3-14(d), and the important profiles are illustrated in Fig. 3-15(d) and Fig. 3-16(d).

For the base contact, we use the same thin photoresist that was applied for the emitter. The great challenge of this photolithographic step is the base-emitter alignment as was illustrated in Fig. 3-3(a) and Fig. 3-4. Sometimes, we had to repeat the same step until the desired alignment was achieved. This is a time consuming and laborious process. However, it is essential for a self-aligned HBT geometry. Next, we evaporate Pt/Zn/Au. We adopt the steps of the emitter liftoff for the base liftoff. However, the handling and cleaning of the processed piece must be done with extra care due to the presence of the emitter metal undercut. The layout is illustrated in Fig. 3-14(e) and the important profiles are depicted in Fig. 3-15(e) and Fig. 3-16(e). We perform rapid thermal annealing for the alloyed ohmic contact. We could have deferred this step until the subcollector thermal treatment. However, Zn forms an alloy with Au at relatively low temperatures ($\sim$ 150 °C) that we usually reach in a photolithigraphic process. Therefore, we chose an early base contact alloying step.

3.8.4 Base and Collector Etching, Subcollector Contact, and Device Isolation

A low $C_{j,Cx}$ calls for the removal of the base and collector material in all areas except those protected by the emitter and base contact. The first approach that was adopted in the early stages of the fabrication was a wet etching process with the emitter and base contact as masks. The base and collector are etched away and the subcollector area is exposed. This fabrication step is simple and subcollector surface is smooth with no RIE by-products. However, the yield of this step was very low.

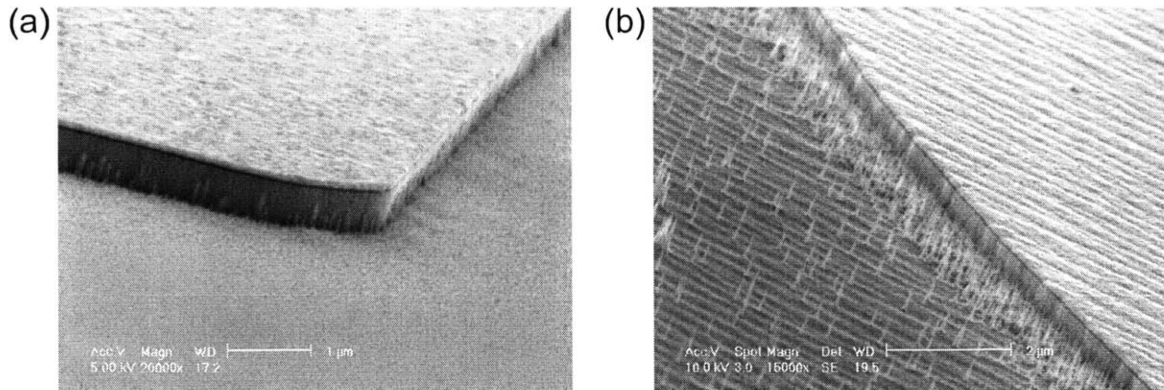

Figure 3-20: Etching profiles of a (a) GaAs layer and an (b) $Al_xGa_{1-x}As$ layer using the $CH_4/H_2/He$ recipe with a metal surface as a mask. Prolonged etching causes degradation of the metal surface. The Al etch products appear as spikes on the etched surface.

The collector is relatively thick and more than 1 μm of material must be removed. The undercut of both the emitter and the base is severe and the contacts easily detouch from the device area. The wet etching process is more suitable for an HBT of large base and emitter contact areas.

We utilize dry etching to reach the subcollector area. In this way, we avoid the undesirable undercuts and we establish a self-aligned HBT structure. In the beginning, we tried dry etching utilizing a $CH_4/H_2/He$ recipe [97, 98]. The etching rate of GaAs is very slow, about 100 Å/min. Therefore, the etching process is long and the metal surface of the emitter and base contact deteriorate. Furthermore, a polymer film is formed on the device area that has to be etched away by an O_2 plasma. An etching profile of GaAs using a metal surface as a mask is shown in Fig. 3-20(a). The etching of $Al_xGa_{1-x}As$ in the base is even slower and more problematic as the Al etch products are not volatile and form pointy structures shown in Fig. 3-20(b). Next, we applied a BCl_3/He recipe [99, 100, 101, 102]. The etching rate is approximately 2000 Å/min. The etching profiles are almost vertical as shown in Fig. 3-21. The important device profiles are illustrated in Fig. 3-15(f) and Fig. 3-16(f). The metal degradation for 1 μm of $Al_xGa_{1-x}As/GaAs$ etching is mild. This is contrary to most Cl_2-based etching recipes.

The surface of the subocollector is damaged after the dry etching step. This can be easily verified by the higher breakdown voltage of the exposed surface. Therefore, it is necessary to remove a 2000-3000 Å layer of the subcollector by wet etching prior to the subcollector contact evaporation. The subcollector is thick enough for a low subcollector sheet resistance even with this shallow wet etching step. The device area is protected by photoresist and a window is opened from the side of the subcollector (Fig. 3-14(f)). In this way, the galvanic effect is suppressed and the undesirable undercuts of the device are avoided. We use the wet etching solution 10 ml NH_4OH : 4 ml H_2O_2 : 500 ml H_2O. The device profile is shown in Fig. 3-15(g).

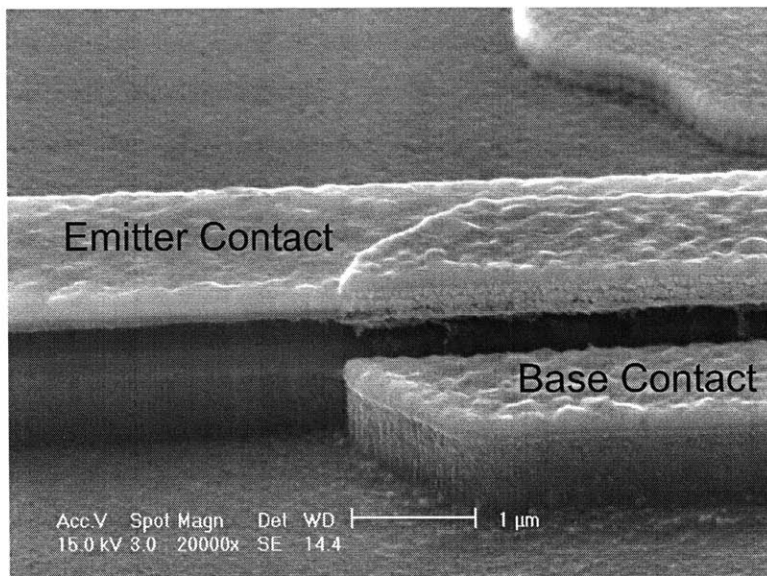

Figure 3-21: Almost vertical etching profiles of the intrinsic part (under the emiter contact) and the extrinsic part (under the base contact) of the HBT using the BCl_3/He recipe.

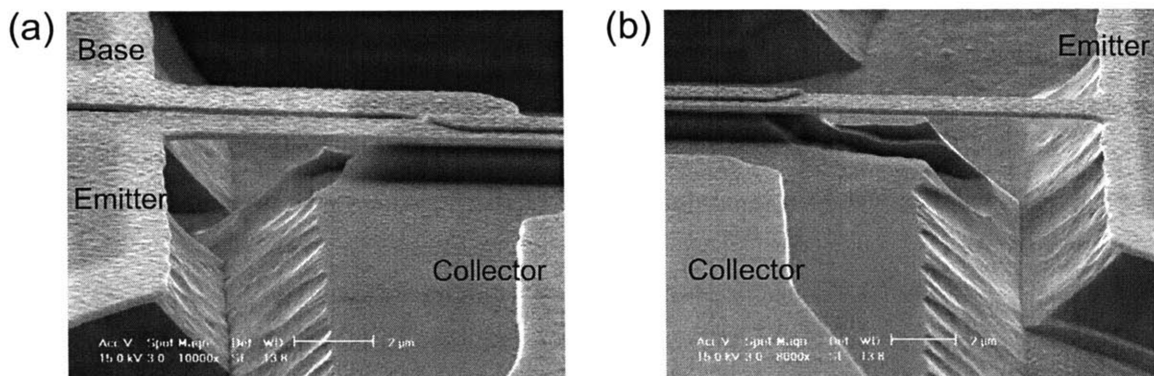

Figure 3-22: SEM pictures of the emitter and base micro-airbridges. From one side of the HBT, (a) the emitter micro-airbridge is in parallel to the base micro-airbridge, and from the other side, (b) there is only the emitter micro-airbridge. The undercut from the deep wet-etching process is more pronounced along the micro-airbridges due to the galvanic effect.

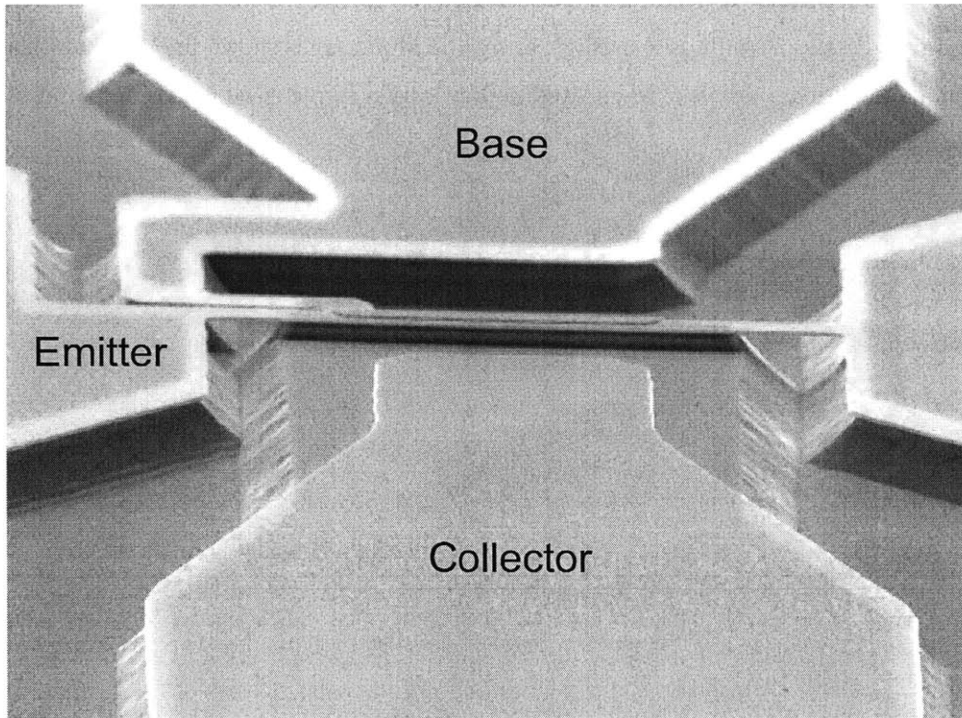

Figure 3-23: SEM picture of the complete HBT device. The emitter and base micro-airbridges are revealed afer the final step of deep wet etching.

The subcollector contact photolithography follows. The device mesa is more than 1 μm high and a photoresist of 1.4 μm thickness is used. Next, we evaporate Ni/Au/Ge/Au/Ni/Au. The device layout is illustrated in Fig. 3-14(g) and the device profile is shown in Fig. 3-15(h). The thermal annealing process of the subcollector follows. The extrinsic base resistance is expected to degrade to some degree after this step. This is attributed to the reduction of the base layer due to the increased metal diffusion. The thinner the base layer is, the higher the base sheet resistance becomes. In addition, the specific contact resistance becomes worse. A thin, highly doped layer of $Al_xGa_{1-x}As$ has been initially created by the diffusion of Zn during the base rapid thermal annealing. The diffusion of Au into this layer suppresses the benefits of the first alloying step. The device isolation takes place by covering the HBT and the coplanar waveguide by photoresist (Fig. 3-14(h)) and performing a deep wet etching with 10 ml NH_4OH : 4 ml H_2O_2 : 500 ml H_2O. In the early stages of the fabrication process, only the HBT was covered. The galvanic effect was severe and large undercuts were created across the waveguide structures. The deep wet etching step removes about 1.5-2 μm of semiconductor to achieve the device isolation. It should be noted that the photoresist mask should account for the undercut of the wet etching. Due to the galvanic effect of the uncovered metal surface, the undercut is expected to be larger along the emitter and base micro-airbridge. This can be easily seen in the SEM pictures of the emitter and base micro-airbridges

in Fig. 3-22. The resultant device layout is illustrated in Fig. 3-14(i), the profile of the emitter and base micro-airbidges is shown in Fig. 3-16(g), and an SEM picture is shown in Fig. 3-23. The emitter and base micro-airbridges are very fragile and no fabrication step can be performed after the device isolation.

Chapter 4

Experimental Results

4.1 Measurements of the Specific Contact Resistance

The specific contact resistance of the emitter, the base, and the subcollector was determined by transmission line measurements (TLM)[103, 104]. As shown in Fig. 4-1, the TLM structure consists of a rectangular mesa of height X. N ohmic contact pads with dimensions $W \times L$ are evaporated along the mesa and are separated by increasing spacings S_1, S_2,...,S_{N-1}. When two probes are placed on the adjacent ohmic contact pads i and $i+1$, we measure a resistance

$$R_{i,i+1} = \frac{\sqrt{\rho_c R_s}}{L} \coth\left(W\sqrt{R_s/\rho_c}\right) + \frac{R_s}{L} S_i, \tag{4.1}$$

where R_s is the sheet resistance of the contacting layer, ρ_c is the specific contact resistance of the ohmic contact used, and $\sqrt{\rho_c/R_s}$ is defined as the transfer length of the ohmic contact. Here, we assume that the probe resistance has been subtracted from the measurements. This expression can be directly derived if we use the same arguments that led to the base and collector extrinsic resistances of Eqs. 2.43-2.44. For the most common cases where $W \gg \sqrt{\rho_c/R_s}$, Eq. 4.1 can be simplified:

$$R_{i,i+1} \approx \frac{\sqrt{\rho_c R_s}}{L} + \frac{R_s}{L} S_i. \tag{4.2}$$

Therefore, R_s and ρ_c can be extracted from the slope and the interpolated resistance value for zero spacing. The current flow is limited by the geometry of the mesa. If no mesa was defined, Eqs. 4.1 would not hold since the current flow could no longer be assumed uniform. Concentric transmission line structures do not require the use of a mesa and make the TLM fabrication easier [105]. Unfortunately, the measured resistance has a logarithmic dependence with the spacing. We used concentric TLM structures in the early stages of the fabrication process and we found that the parameter extraction can be severely affected by the measurement errors. We should point out that the simple expression of Eq. 4.1 has to be modified for alloyed ohmic contacts to account for

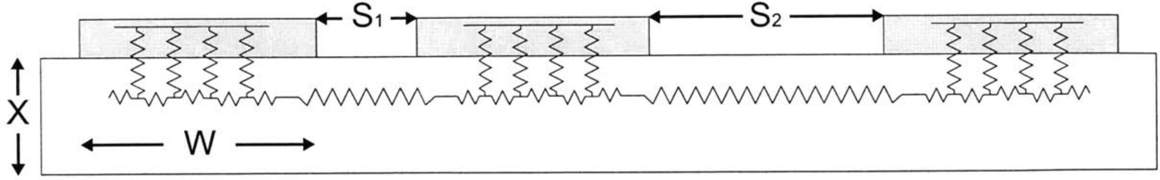

Figure 4-1: Cross section of a structure used for transmission line measurements. The length of every ohmic contact pad, not shown in the figure, is L. The separation distances of N ohmic contact pads are S_1, S_2,...,S_{N-1} and $S_1 < S_2 < ... < S_{N-1}$.

the alloying depth [104]. However, the allowed ohmic contacts that we utilize for the base and the subcollector, incorporate a diffusion barrier. Therefore, we expect that the alloying depth is a small fraction of the layer thickness and Eq. 4.1 remains a satisfactory approximation. Since the pad spacing S_i is critical in extracting ohmic contact parameters, the knowledge of the photolithigraphic tolerances is important. It is common during the development of HBT ohmic contacts to obtain accurate information of S_i with SEM pictures. For simplicity, we did not verify the exact S_i dimensions, but we could safely assume a 0.2-0.5 μm tolerance. We should note that the targeted metal thickness of an ohmic contact differs from the measured total thickness. This is most likely due to the uncertainty of the tooling factor needed during the metal deposition. The tooling factor is a parameter related to the distances between the crucible, the crystal detector, and the device piece. We conducted metal thickness measurements with a profilometer.

The TLM measurements of the emitter cap ohmic contact are shown in Fig. 4-2(a). The evaporated metal layers are Ti(500 Å)/Pt(300 Å)/Au(2200 Å) and no alloying was followed. The extracted specific contact resistance $\rho_{cap,c}$ is approximately 2×10^{-8} Ω cm^2 which is among the best reported for n-type InGaAs ohmic contacts [51, 52, 53]. Here, we have made the assumption that the sheet resistance is uniform. This is a satisfactory approximation for the InGaAs layers 1 and 2 of the emitter cap in Table 3.1 where the doping level is the same. The GaAs layer 3 has a lower doping level but we could assume that most of the transverse current in the TLM structure flows in layers 1 and 2. Although we operated the e-beam evaporator for a metal thickness of 3000 Å, it was measured to be in the range of 2000-2300 Å.

The TLM measurements of the subcollector ohmic contacts are presented in Fig. 4-2(b). We evaporated Ni(50 Å)/Au(100 Å)/Ge(500 Å)/Au(900 Å)/Ni(300 Å)/Au(1200 Å) and performed rapid thermal annealing at 380 °C for 30 s. The specific contact resistance of the subcollector ohmic contact is measured to be 2×10^{-6} Ω cm^2 and the sheet resistance is approximately 18 Ω/sq. Au/Ge-based ohmic contacts on heavily doped n-type GaAs usually yield ohmic contacts with specific contact resistance in the vicinity of 5×10^{-7} Ω cm^2. The discrepancy could be attributed to the presence of the first Ni layer that acts as a diffusion barrier, and possibly to a lower subcollector doping level.

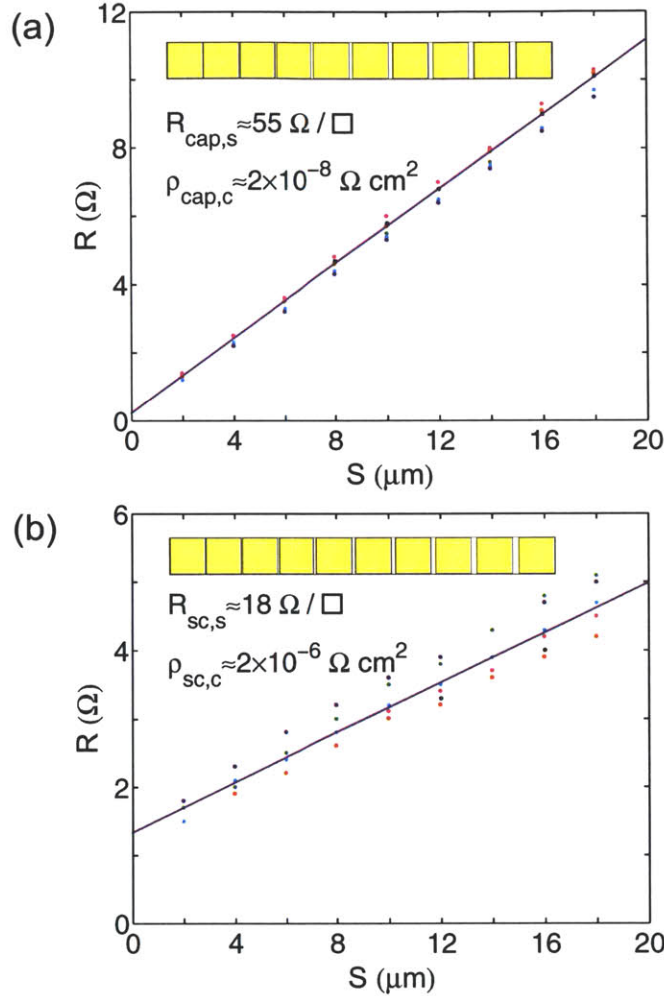

Figure 4-2: (a) Transmission line measurements of the emitter cap ohmic contacts (100 μm × 100 μm). The mesa includes the emitter cap and the emitter layers. The exposed surface away from the mesa is within the base layer. The evaporated metal layers are Ti(500 Å)/Pt(300 Å)/Au(2200 Å). The ohmic contact is non-alloyed. (b) Transmission line measurements of the subcollector ohmic contacts (100 μm × 100 μm). The mesa includes the subcollector layer. The exposed surface away from the mesa is within the semi-insulating GaAs wafer. The evaporated metal layers are Ni(50 Å)/Au (100 Å)/Ge(500 Å)/Au(900 Å)/Ni(300 Å)/Au(1200 Å). The ohmic contact is alloyed. For both (a) and (b), the measurements were taken for TLM structures of the same device piece. The measurement points with the same color represent a particular TLM structure.

In addition, the sheet resistance is higher than expected. A sheet resistance of 9 Ω/sq has been reported in [35] for the same thickness and doping level. Therefore, the actual doping level of the subcollector may be in the vicinity of 2×10^{18} cm^{-3} than the targeted 5×10^{18} cm^{-3}. However, even these moderate values are not prohibitive for transit-time oscillations. We should note that the total subcollector ohmic contact thickness was measured to be in the range of 2300-2500 Å instead of the targeted 3050 Å.

The TLM measurements of the base ohmic contact are shown in Fig. 4-3. For a device wafer with N_B=5 $\times$ 10^{19} cm^{-3}, we evaporated Pt(65 Å)/Ti(300 Å)/Pt(300 Å)/Au(900 Å) and no annealing was followed. As shown in Fig. 4-3(a), the extracted specific contact resistance is favorably low, approximately 2×10^{-7} Ω cm^2. This is close to the reported value of 4×10^{-7} Ω cm^2 in [57]. The base sheet resistance is close to the expected value. From $R_{b,s}$, we can readily derive the base resistivity and the product $N_B \times \mu_p$, where μ_p is the majority carrier mobility in the p-type base. Based on the data of Fig. 4-3(a), $N_B \times \mu_p \approx 2.2 \times 10^{21}$ cm^{-1} V^{-1} s^{-1}. Therefore, for N_B=5 $\times$ 10^{19} cm^{-3}, $\mu_p \approx 44$ cm^2 V^{-1} s^{-1}. Based on [53], the extracted value of μ_p from TLM measurements is in the vicinity of 60 cm^2 V^{-1} s^{-1} Therefore, either μ_p or N_B is slightly lower than expected. Due to unsatisfactory DC characteristics that will be presented and discussed in the following section, we lowered the doping level of the base layer to the value of 2×10^{19} cm^{-3}. Initially, we attempted the same Pt/Ti/Pt/Au ohmic contact. Although a specific contact resistance in the vicinity of 8×10^{-7} Ω cm^2 has been reported for this doping level [106], the measured value was significantly higher. According to the data of Fig. 4-3(b), the specific contact resistance is 8×10^{-5} Ω cm^2, two orders of magnitude higher than expected. Subsequent alloying deteriorated this value even further. In addition, the base sheet resistance was unexpectedly high, approximately 745 Ω/sq. From this, we can derive that $N_B \times \mu_p \approx 4.8 \times 10^{20}$ cm^{-1} V^{-1}. Therefore, for N_B=2 $\times$ 10^{19} cm^{-3}, $\mu_\mathrm{p} \approx 24$ cm^2 V^{-1}. However, this value is at least three times lower than expected. Most likely, the base doping level is lower than the targeted value of 2×10^{19} cm^{-3}. This could also explain the low value of the specific contact resistance. For a low N_B, the Schottky barrier is wider and the tunneling becomes more difficult, yielding a higher value of the ohmic contact. Therefore, we were forced to use an alloyed ohmic contact. Based on the availability of metals in the clean room, we chose the Pt(80 Å)/Zn(500 Å)/Au(1000 Å) ohmic contact. Rapid thermal annealing was followed at 360 °C for 40 s. The TLM measurements of this ohmic contact are presented in Fig. 4-3(c). The specific contact resistance was extracted to be 6×10^{-6} Ω cm^2, which is significantly improved. Although the base ohmic contact is not as low as anticipated, it is acceptable for our HBT. For transit-time oscillations, it should be noted that the magnitude of the output resistance is independent of R_{Bx}, as shown in Eq. 2.53. The total base ohmic contact thickness was measured to be in the range of 1000-1200 Å instead of the targeted 1580 Å.

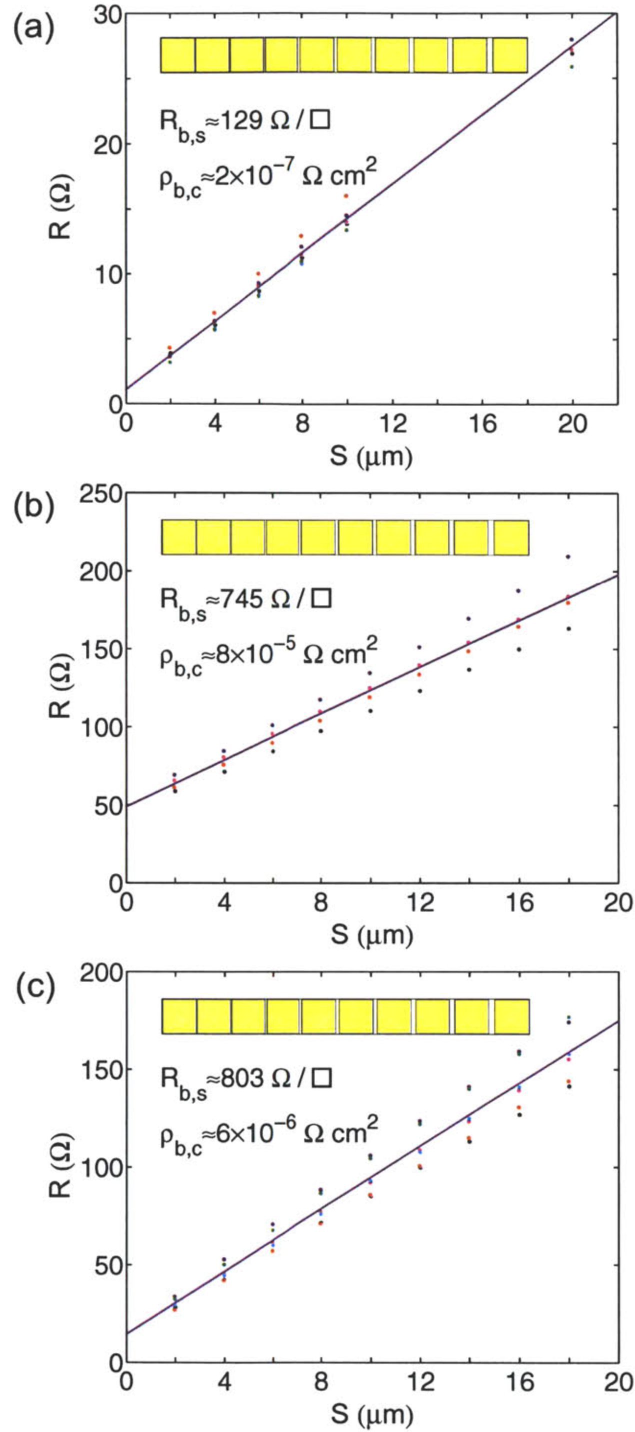

Figure 4-3: Transmission line measurements of the base ohmic contacts (100 μm $\times$ 100 μm). The mesa includes the base and the collector layers. The exposed surface away from the mesa is within the subcollector layer. The thickness of the base layer that has not been etched is approximately 2300 Å for (a) and (c), and 1800 Å for (b). The evaporated metal layers in (a) and (b) are Pt(65 Å)/Ti(300 Å)/Pt(300 Å)/Au(900 Å) (non-alloyed ohmic contact), and in (c), Pt(80 Å)/Zn(500 Å)/Au(1000 Å) (alloyed ohmic contact). In (a), N_B=5 $\times$ 10^{19} cm^{-3}, whereas in (b) and (c), N_B=2 $\times$ 10^{19} cm^{-3}. For (a), (b), and (c), the measurements were taken for TLM structures of the same device piece. The measurement points with the same color represent a particular TLM structure.

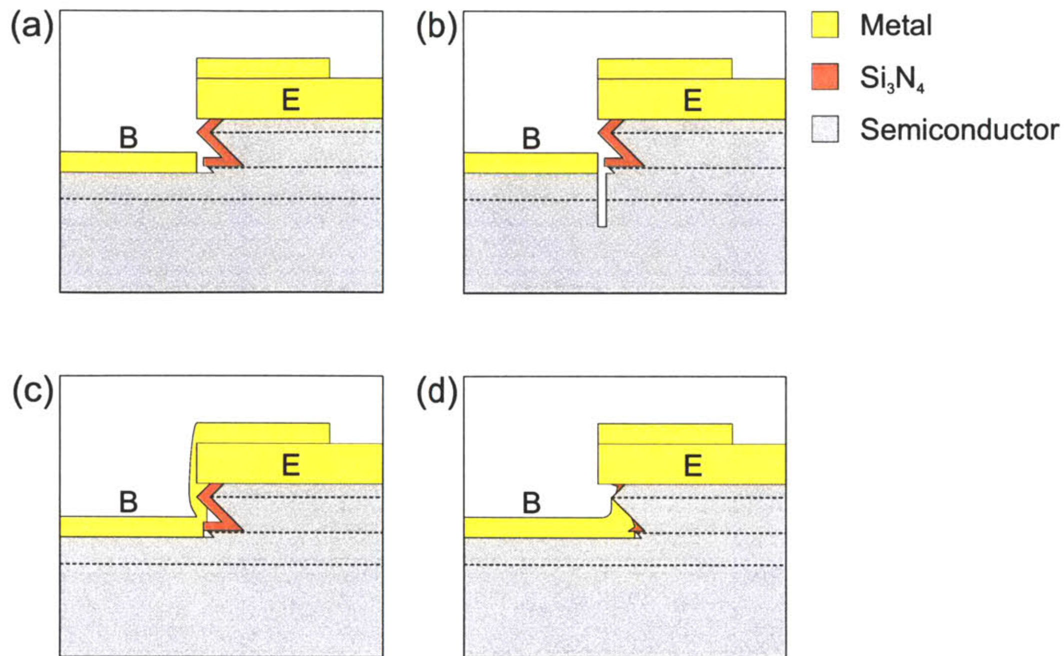

Figure 4-4: Various device profiles of the self-aligned HBTs at the end of the fabrication process. The dashed lines are the interfaces of the emitter cap, the emitter, the base, and the subcollector. The metal, the semiconductor, and the sidewall passivation are respresented by the yellow, grey, and red areas, respectively. The ideal HBT device is illustrated in (a). In (b), BCl_3 etched away part of the exposed base and the intrinsic base cannot be contacted. In (c), the base metal created an electric short between the emitter and base contact. In (d), the RIE process of the Si_3N_4 layer etched away part of the sidewall passivation and the base metal contacts both the emitter and the base layer.

4.2 Device Profile and Failure Modes

We discussed in 3.8 that the fabrication steps prior to the base metal evaporation are time consuming and laborious. They include some important safeguards for the device yield, namely protection against the galvanic effect, suitable inward slope for the emitter mesa, and sidewall deposition of Si_3N_4. The ideal device profile is illustrated in Fig. 4-4(a). The different slopes of the emitter mesa were created by the use of the isotropic and anisotropic wet etching processes. However, the HBT fabrication produces also a number of devices with profiles that do not yield the desired HBT operation. These failure modes emanate from the HBT self-alignment. The emitter contact and the emitter mesa are in very close proximity to the base contact and the exposed base. Despite the various safeguards, there exist cases where either the exposed base is etched away or an electric short is created between the emitter and the base.

In Fig. 4-4(b), the dry etching process proved to be fatal for the device operation. The BCl_3 plasma crept in the unprotected semiconductor area and etched away part of the exposed base. Therefore, the intrinsic base becomes isolated and the device is not functional. We noticed this

failure mode during the dry etching process of the base and the collector. We performed I-V plots of the emitter-base diode with a curve tracer during the etching process. Some devices, although functional during the RIE process, became open circuits at the end of the RIE process. This is a clear indication of Fig. 4-4(b). We anticipated the emergence of this problem and we included an additional photolothigraphic step in our set of masks. Specifically, if the unprotected area of the semiconductor along the emitter-base junction is covered by photoresist, the dry etching step becomes safer. After the BCl_3 etching, the burned photoresist can be easily removed in O_2 plasma. However, this photoresist stripe has to be at most 1.5-2.0 μm wide, covering partially the emitter and base stripes. In addition, the alignment is very critical. Unfortunately, the limitations of our mask aligner do not allow the incorporation of this process step prior to BCl_3 etching.

In Fig. 4-4(c), the base metal is deposited on the sidewalls and an electric short is created between the emitter contact and the base contact. This failure mode can be detected after the liftoff of the base metal. We performed measurements of the emitter-base resistance with an multimeter. An ideal device yields a very high resistance between the emitter and the base since the emitter-base diode is off. On the contrary, a device with the Fig. 4-4(c) profile can be easily detected as an electric short. It should be noted that this failure mode was more often encountered when the photoresist used during the base photolithography was thin (0.6 μm). A thicker photoresist (1.4 μm) resulted in higher yield. We could deduce that the high photoresist sidewalls direct the evaporated metal better in the vertical direction.

In Fig. 4-4(d), the RIE etching of the Si_3N_4 was not perfectly vertical and part of the emitter mesa is no longer passivated. Therefore, the base metal can contact the emitter layer. This failure mode can be detected during the base and collector dry etching. The I-V plots were suggesting an emitter-base resistor rather than an emitter-base diode. This failure mode can be possibly avoided if the plasma for etching Si_3N_4 becomes less dense by decreasing the ECR power. However, we have to increase the RF power significantly causing more roughness and traps on the exposed semiconductor.

4.3 DC Measurements

We will present DC measurements from three different MBE designs. The device piece was placed on a probe station which was connected to an HP Parameter Analyzer. The HBTs were operating in the common-emitter configuration. For convenience, a name convention will be adopted for the HBT devices under test. We characterized the DC performance of the SM6000, SM7000, SM9000, LG7000, LG9000, and LG7000U HBT devices. The first two letters signify whether it is a small, self-aligned device (SM) or a large device with no self-alignment (LG). The number that follows represents the targeted thickness of the collector in Å. Finally, the letter U signifies that the base is uniform (no stepwise alloy-grading). The SM6000, SM7000, and SM9000 have almost the same

Table 4.1: Differences in the layout and MBE design of the HBT devices under test.

Device	SM6000	SM7000	SM9000	LG7000	LG9000	LG7000U
W_E (μm)	2	2	2	100	100	100
W_B (μm)	1.5	1.5	1.5	100	100	100
S_{BE} (μm)	0	0	0	4	4	4
L_E (μm)	15	15	15	100	100	100
N_B (cm^{-3})	5×10^{19}	2×10^{19}	2×10^{19}	2×10^{19}	2×10^{19}	2×10^{19}
N_C (cm^{-3})	3×10^{16}	2×10^{16}	2×10^{16}	2×10^{16}	2×10^{16}	2×10^{16}
N	5	5	5	5	5	1
X_{step} (Å)	600	600	600	600	600	3000
X_C (Å)	6000	7420	9540	7420	9540	7420
X_S (Å)	0	100	100	100	100	100
$T_{sub,E}$(°C)	450	600	600	600	600	600
$T_{sub,B}$(°C)	450	550	550	550	550	550

layout. The SM6000 predate all the other devices so a few non-critical layout modifications were added in the SM7000 and SM9000 designs. Furthermore, the LG7000, LG9000, and LG7000U have the same layout. The SM7000 and LG7000 have been fabricated on pieces of the same MBE wafer. The same holds for the SM9000 and LG9000 devices. For convenience, we name the device wafers as MBE6000, MBE7000, MBE9000, and MBE7000U. The layout and MBE design differences are summarized in Table 4.1. The same name conventions of the layout and MBE design parameters hold. In addition, $T_{sub,E}$ and $T_{sub,B}$ is the substrate temperature during the emitter and base growth, respectively, and X_S is the thickness of the undoped spacer located between the emitter and the base. Unless specified, the MBE design parameters of Table 3.1 are assumed.

From Table 4.1, it becomes evident that MBE7000 and MBE9000 are the same with the exception of the collector thickness. In addition, MBE7000 and MBE7000U are the same with the exception of the base. The former has 5 base steps whereas the latter has a uniform GaAs base. It should be noted that the collector thickness of MBE7000, MBE9000, and MBE7000U is about 6% larger than the targeted value due to a flux calibration error prior to the device wafer epitaxial growth. MBE6000 differs from the other wafers in the base (N_B), collector (X_C and N_C), and spacer (X_S), and most importantly in the substrate temperature during the emitter and base growth. Therefore, we expect that the DC performance of SM6000 will be distinctly different from that of SM7000 and SM9000.

We will first discuss the origin of the collector and base current ideality factors in order to establish a better perspective for the analysis of the measured I-V characteristics. An extensive analysis of the HBT DC operation can be found in [35, 34]. It is common in the interpretation of the measured I_C-V_{BE} and I_B-V_{BE} characteristics to apply curve-fitting derived from the expression

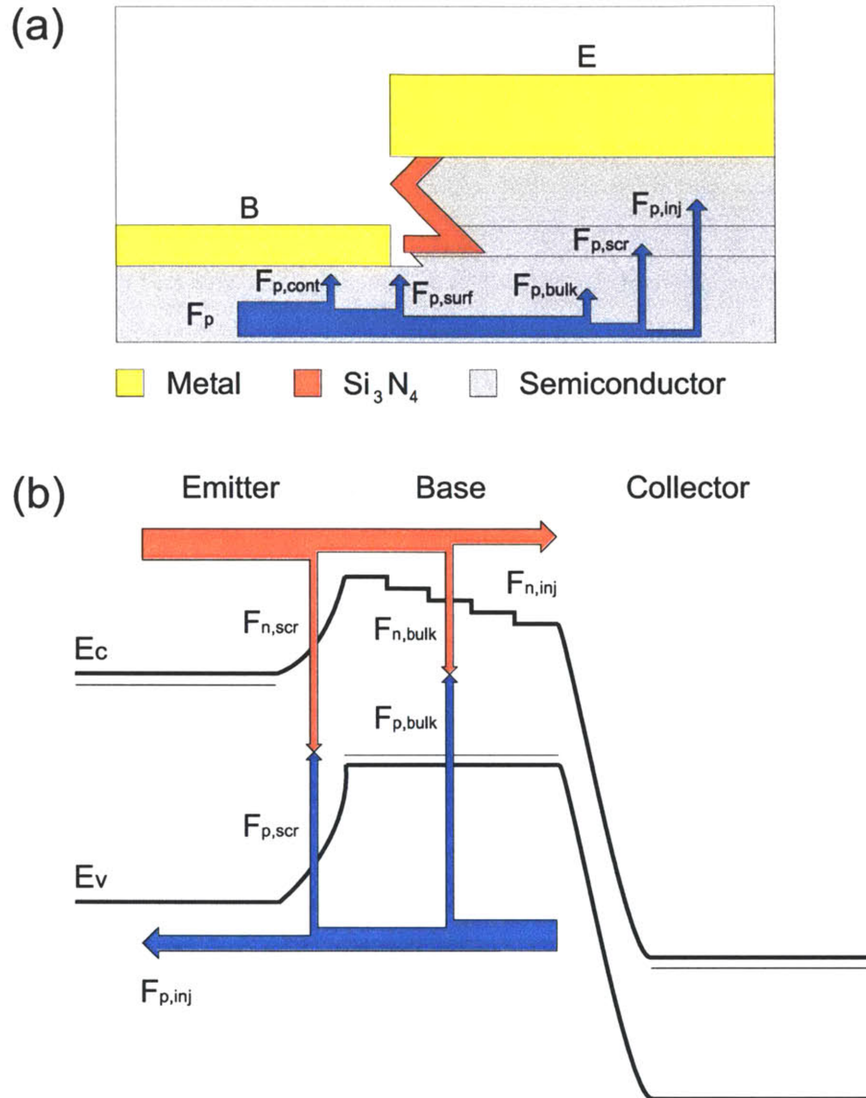

Figure 4-5: (a) Schematic illustrating a cross-section of the HBT and the various components constituting the flow of holes F_p in the base. The area between the dashed lines is the emitter-base space charge region. $F_{p,cont}$, $F_{p,surf}$, $F_{p,bulk}$, and $F_{p,scr}$ represent the recombination on the base contact, on the exposed base, in the bulk of the base, and in the emmitter-base space charge region, respectively. $F_{p,inj}$ represents the injected flow of holes from the base to the emitter. (b) Band diagram of the device along with the components of the electron and hole flow. The carrier flow components associated with the recombination in the extrinsic part of the device (base contact and exposed base) are not shown.

$I_{fit} \equiv I_s \exp[qV_{BE}/(\eta k_B T)]$, where η is the ideality factor and T=300 K. We will refer to the ideality factor of the collector and base current as η_C and η_B, respectively. The ideality factor of the collector current is affected only by the E-B junction. For a smoothly alloy-graded E-B junction, the electrons are injected from the emitter to the base by thermionic emission and the collector ideality factor is approximately 1 since $n' \propto \exp[qV_{BE}/(k_B T)]$, where n' is the excess minority carrier concentration at the beginning of the base. For an abrupt E-B junction where a conduction band spike appear, the injection mechanisms are thermionic emission and field emission (tunneling). By a thermionic-field emission analysis, it can be shown that the collector ideality factor is in this case slightly larger than 1.

The flow of holes F_p consists of the following components, illustrated in Fig. 4-5(a): (a) injected holes from the base to the emitter $F_{p,inj}$, (b) recombined holes in the space charge region of the E-B junction $F_{p,scr}$, (c) recombined holes in the bulk of the base $F_{p,bulk}$, (d) recombined holes on the exposed base surface $F_{p,surf}$, and (e) recombined holes on the surface of the base contact $F_{p,cont}$. The carrier flow components associated with the intrinsic part of the device are also shown in the HBT band diagram of Fig. 4-5(b). The most important base current components are $I_{p,bulk}$, $I_{p,scr}$, and $I_{p,inj}$. A good surface passivation can reduce $I_{p,surf}$. For a non-zero S_{BE}, the minority carrier concentration is small close to the base contact and the recombination is expected to be low, yielding a small $I_{p,cont}$. The ideality factor of $I_{p,inj}$ is approximately 1 from the Maxwell distribution of excess holes at the beginning of the E-B space charge region, $p' \propto \exp[qV_{BE}/(k_B T)]$. The ideality factor of $I_{p,bulk}$ is approximatelly 1. This can be explained from the fact that the recombination rate U in the bulk of the quasi-neutral base is proportional to the excess minority carrier concentration and $n' \propto \exp[qV_{BE}/(k_B T)]$. The ideality factor of the $I_{p,scr}$ is approximately 2. In this case, the argument that $U \propto n'$ does not apply since it holds only for a quasi-neutral region. Instead, the full expression of the recombination rate has to be used, and $U \propto (np - n_i^2)$. In order to avoid any mathematical complexity, we refer to the intuitive explanation suggested in [107]. The space charge region recombination requires that the carriers acquire on average energy sufficient for half of the barrier height (Fig. 4-5(b)). This should be contrasted with the injected current $I_{p,inj}$ where it is necessary that the carriers cross the whole barrier. Therefore, the former has a $\exp[qV_{BE}/(2k_B T)]$ dependence, whereas the latter has a $\exp[qV_{BE}/(k_B T)]$ dependence as discussed earlier. The ideality factor of $I_{p,surf}$ cannot be easily derived from simple arguments and the reader is referred in [108] for a detailed discussion. The key result of this analysis is that $n_{surf} \propto \sqrt{np}$, where n_{surf} is the concentration of surface states. Consequently, $I_{p,surf} \propto \exp[qV_{BE}/(2k_B T)]$. It is also shown in [108] that at high current densities $n_{surf} \propto n$, and therefore $I_{p,surf} \propto \exp[qV_{BE}/(k_B T)]$. Similar arguments can be applied for $I_{p,cont}$ since both $I_{p,cont}$ and $I_{p,surf}$ originate from surfaces of high recombination velocities. The total base current $I_B = I_{p,cont} + I_{p,surf} + I_{p,bulk} + I_{p,scr} + I_{p,inj}$ is expected to have an ideality factor in the range between 1 and 2, depending on the dominant base

current component for a given bias point.

4.3.1 DC Characteristics of SM6000

The DC measurements of SM6000 are presented in Fig. 4-6. The I_C-V_{BE} and I_B-V_{BE} characteristics for a given V_{CB} are shown in Fig. 4-6(a) in semi-logarithmic scale. We selected V_{CB}=7 V for full collector depletion. The inset includes the extracted β-V_{BE} plot along with the I_C-V_{BE} and I_B-V_{BE} characteristics in linear scale. The dash-dotted lines are curve fits of the measured I_C and I_B. It can bee seen in Fig. 4-6(a) that there exist V_{BE} regions where $\eta_C \approx 3.0$ and $\eta_B \approx 4.5$. Both η_C and η_B are much higher than expected. This can be an indication that there exists an abundance of impurity mid-gap states. In the design of MBE6000, we set a design goal which was hard to achieve. The base doping was chosen to be very high, N_B=5 $\times$ 10^{19} cm^{-3}, and the substrate temperature during the base growth was low, $T_{sub,B}$=450 °C, to assist the incorporation of Be as a p-dopant. However, a low temperature growth is more suitable for a GaAs base. As discussed previously in 3.1, a low temperature growth is not recommended for an AlGaAs base because it can lead to significant incorporation of impurities. According to [109], a rapid increase of the trap concentration has been observed when the substrate temperature decreases during the growth of $Al_xGa_{1-x}As$. Furthermore, we kept for convenience the same low substrate temperature during the emitter growth where the Al is even higher (x=0.35) and the crystal quality of the emitter is expected to be even worse. As shown Fig. 4-6, the ideality factors of the collector and base currents are even higher for $V_{BE} > 2$. This can be attributed to the ohmic losses. At high current levels, the voltage across the the E-B junction, $V_{BE,j}$, differs from the applied voltage V_{BE}. Specifically, $V_{BE,j}$=$V_{BE} - I_E R_{Ex} - I_B R_{Bx}$. Therefore, the current increases at a lower rate, $I_C \propto \exp\left[q\left(V_{BE} - I_E R_{Ex} - I_B R_{Bx}\right)/(k_B T)\right]$. The maximum current gain is unexpectedly very low, β_{max}=1.6 for V_{CB}=6 V (complete collector depletion).

The I_C-V_{CE} characteristics of SM6000 for a family of I_B values are shown in Fig. 4-6(b). For increasing V_{CE}, the I_C curves bend downwards which is an indication of current gain degradation. This is typical in many HBT designs. High V_{CE} leads to self heating. At room temperature, the energy barrier ΔE_g, if high enough, is sufficient to suppress the injection of holes from the base to the emitter and $I_{p,inj}$ is small. However, as the device temperature increases, the holes acquire more energgy and the energy barrier is less effective in blocking back-injection. According to the simple approach of 2.1, if we neglect the recombination components of the base current, it follows that $\beta \propto \exp\left[\Delta E_g/(k_B T)\right]$. Thus, high temperature leads to a lower current gain. On the contrary, the current gain increases as temperature increases in BJTs [35]. In the BJT design, $N_E \gg N_B$. Although the E-B junction is a homojunction, the high doping level of the emitter causes bandgap narrowing. The wider bandgap material is the base, contrary to the HBT design. Consequently, the reverse trend is to be expected. In Fig. 4-6(b), the values of I_B are fixed by the external current source. Consequently, the lowering of β manifests by the decreasing values of I_C.

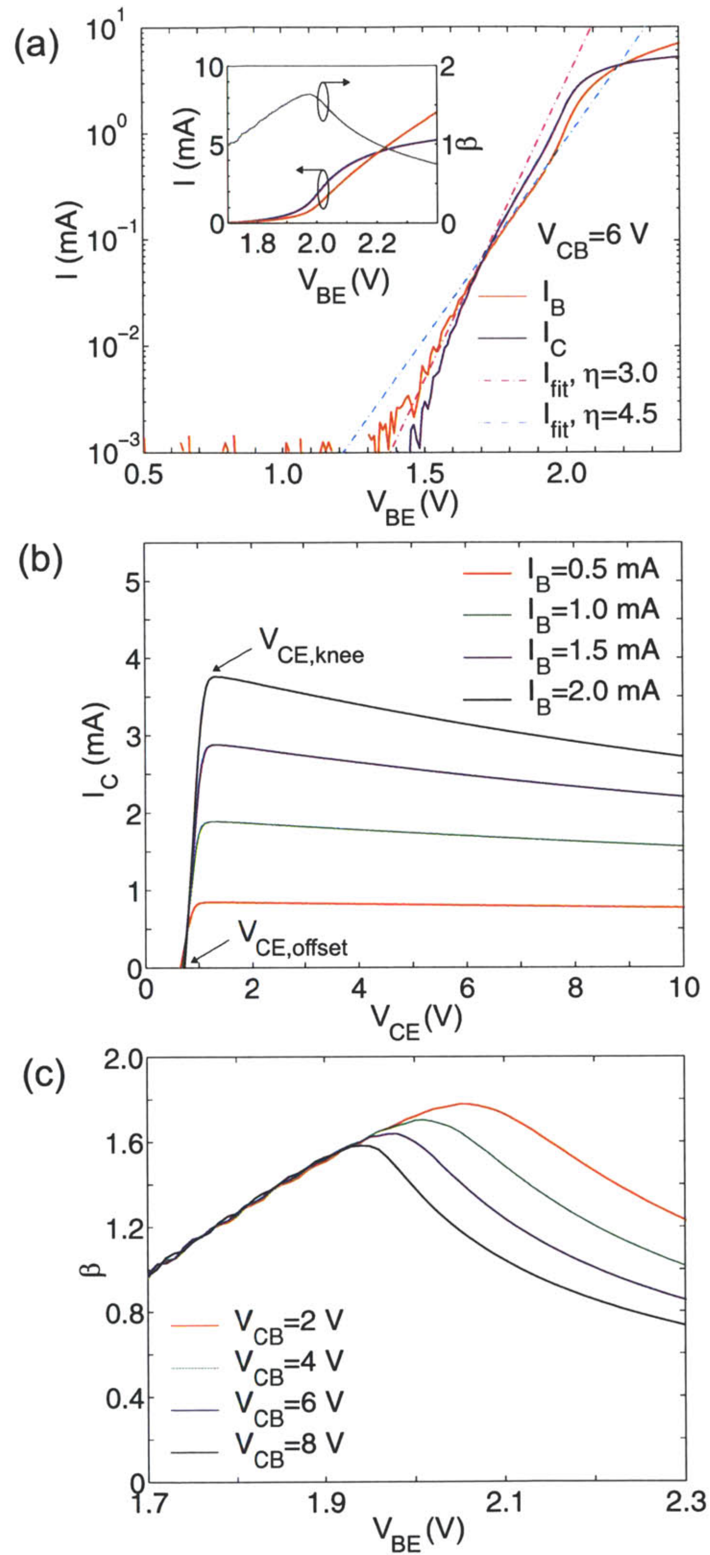

Figure 4-6: Measured DC characteristics of SM6000. In (a), I_C and I_B are plotted vs V_{BE} for a given V_{CB}. The dash-dotted lines originate from I_C and I_B curve fitting using suitable ideality factors. The inset illustrates I_C, I_B, and β vs V_{BE} in linear scale. In (b), I_C is plotted vs V_{CE} for a family of I_B values. In (c), β is plotted vs V_{BE} for a family of V_{CB} values.

The offset voltage is defined as the value $V_{CE,offset}$ where the collector current vanishes. For $V_{CE} < V_{CE,offset}$, the collector current changes direction and assumes negative values. The knee voltage is defined as the value $V_{CE,knee}$ where the collector current attains its maximum value. It is worth investigating the origin of the offset voltage. In the forward-active regime, the base-emitter junction is forward biased ($V_{BE} > 0$) and the base-collector junction is reverse biased ($V_{CB} > 0$). For low values of V_{CE}, it is possible to have $V_{CE} > 0$, $V_{BE} > 0$, and $V_{CB} < 0$ ($V_{CE} = V_{CB} + V_{BE}$). This is the saturation mode of the HBT and it occurs for $V_{CE,offset} \leq V_{CE} \leq V_{CE,knee}$. The roles of the emitter and collector are swapped for $V_{CE} < V_{CE,offset}$. The non-zero value of $V_{CE,offset}$ reflects the difference between the base-emitter junction and the base-collector junction. If these junctions were identical, the device would be summetrical and $V_{CE,offset} = 0$. In a HBT, the junctions are not identical. In a typical HBT design, the built-in potential of the emitter-base heterojunction $\varphi_{bi,BE}$ is higher than the built-in potential of the base-collector homojunction $\varphi_{bi,BC}$. Therefore, $V_{CE,offset}$ shifts to positive values. The values of the built-in potential at the base-emitter and base-collector junction be easily calculated from the difference of the Fermi levels at the two sides of the junction before thermal equilibrium. In general, the offset voltage of a HBT increases the power consumption and reduces the active region of operation. Double HBTs (DHBTs) have been introduced to decrease $V_{CE,offset}$. Due to symmetrical nature of the emitter-base and base-collector junction in a DHBT, $V_{CE,offset}$ can be a few mV. In the design of SM6000, $\varphi_{bi,BE} \approx 1.7$ V and $\varphi_{bi,BC} \approx 1.4$ V and we anticipated $V_{CE,offset} \approx 0.3$ V. Instead, the measured value of $V_{CE,offset}$ is 0.7 V, which is much higher than expected. This observation supports further the argument of the poor crystal growth.

The β-V_{BE} characteristics of SM6000 for a family of V_{CB} values are shown in Fig. 4-6(c). The current gain increases monotonically, establishes a maximum value, and then monotonically decreases. In addition, as V_{CB} increases, the value of β_{max} decreases and occurs at lower V_{BE}. These observations can be explained from the previous discussion regarding Fig. 4-6(a)-(b). The current gain of the HBT can be expressed as $\beta \equiv I_C/I_B \propto \exp\left\{[qV_{BE}/(k_BT)]\left(\eta_C^{-1} - \eta_B^{-1}\right)\right\}$. Consequently, β increases in the range of V_{BE} where $\eta_C < \eta_B$, the maximum value is attained when $\eta_C = \eta_B$, and β decreases in the range of V_{BE} where $\eta_C > \eta_B$. For an ideal HBT, $\eta_C \approx 1$. In addition, $\eta_B \approx 2$ in the range of V_{BE} where the space charge recombination current $I_{p,scr}$ is the dominant component of I_B, and $\eta_B \approx 1$ for a V_{BE} bias where a component other than $I_{p,scr}$, like $I_{p,bulk}$, dominates I_B. Therefore, we expect β to increase when $I_B \approx I_{p,scr}$, and remain relatively flat when $I_B \approx I_{p,bulk}$. The range of decreasing β can be attributed to the non-ideality of our device. The difference in the Al concentration between the emitter and the base is $\Delta x_{E-B} = 0.17$ whereas typical AlGaAs/GaAs HBT designs employ $\Delta x_{E-B} \approx 0.30$. The AlGaAs/GaAs HBTs that utilize linear alloy grading in the base have an optimum DC gain when $max(x_B) \approx 0.1$ [110]. For SM6000, $max(x_B) \approx 0.18$, and the injection of holes is not negligible. As V_{BE} increases, the device temperature increases, the

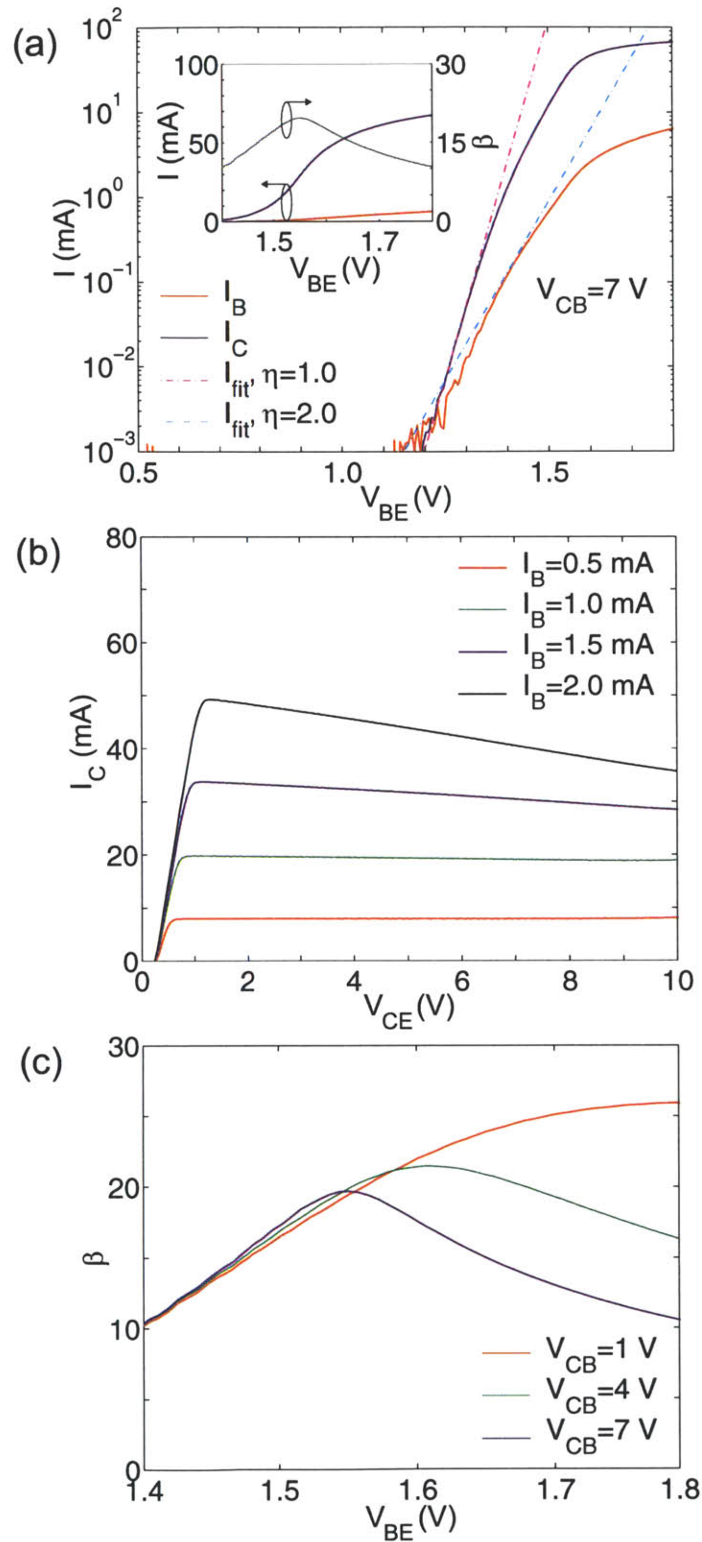

Figure 4-7: Measured DC characteristics of LG7000. In (a), I_C and I_B are plotted vs V_{BE} for a given V_{CB}. The dash-dotted lines originate from I_C and I_B curve fitting using suitable ideality factors. The inset illustrates I_C, I_B, and β vs V_{BE} in linear scale. In (b), I_C is plotted vs V_{CE} for a family of I_B values. In (c), β is plotted vs V_{BE} for a family of V_{CB} values.

holes overcome the energy barrier ΔE_g, and β declines. At a first glance, V_{CB} should not affect β. However, high V_{CB} leads to power dissipation and elevated device temperature. Hence, the peak of β moves to lower values of V_{BE}.

4.3.2 DC Characteristics of LG7000, LG9000, and LG7000U

The high ideality factors of SM6000 led us to modifications in the MBE design. We opted for better crystal quality and we increased the substrate temperature during the growth of MBE7000, MBE9000, and MBE7000U wafers. As discussed in 3.1, we chose $T_{sub,E}$=600 °C and $T_{sub,B}$=550 °C for good quality of the emitter and base layers, respectively. At the same time, we decreased N_B to avoid Be outdiffusion that takes place at elevated $T_{sub,B}$, and we inserted a spacer between the emitter and base layers to mitigate the effects of a potential Be outdiffusion. The fabrication process of the self-aligned HBT as described in 3.8 is laborious and time consuming. The time needed for the fabrication of the large HBTs is about 2-3 weeks. On the other hand, self-aligned HBTs require 6-7 weeks of intense fabrication, provided that no mishap occurs. Our strategy was to fabricate large HBTs with no self-alignement for the purpose of testing the quality of the new wafers. If the performance of the large HBTs was satisfactory, we would subsequently proceed towards the fabrication of self-aligned HBTs. Otherwise, we would have to prepare and submit new MBE designs to our MBE collaborator.

The DC characteristics of LG7000, LG9000, and LG7000U are presented in Figs. 4-7, 4-8, 4-9, respectively. We will analyze them simultaneously since they share similar features and trends. Following the steps of the SM6000 characterization, we performed I_C-V_{BE} and I_B-V_{BE} measurements for a value of V_{CB} that fully depletes the collector (Figs. 4-7(a), 4-8(a), 4-9(a)), I_C-V_{CE} plots for a family of I_B values (Figs. 4-7(b), 4-8(b), 4-9(b)), and we extracted β-V_{BE} characteristics for a family of V_{CB} values (Figs. 4-7(c), 4-8(c), 4-9(c), We can easily detect Figs. 4-7(a), 4-8(a), 4-9(a), a major improvement in the ideality factors of I_C and I_B. Specifically, $\eta_C \approx 1$ for a portion of V_{BE} and then η_C degrades as the ohmic losses become significant. On the other hand, $\eta_B \approx 2$ for low values of V_{BE}, and η_B increases in the region of high ohmic losses. From the value of η_B, we could deduce that the major component of I_B is $I_{p,scr}$. Furthermore, there is a significant improvement in the current gain. This can be attributed to both the improved crystal quality and the lower doping level in the base. We measured $\beta_{max} \approx 20$ at V_{CB}=7 V for LG7000, $\beta_{max} \approx 19$ at V_{CB}=10 V for LG9000, and $\beta_{max} \approx 23$ at V_{CB}=7 V for LG7000U.

We noticed that there is practically no difference in the current gain between LG7000 and LG7000U, or between LG9000 and LG7000U. We will try to justify this observation. When the dominant component of I_B is $I_{p,bulk}$, then we can make some straightforward calculations. As we discussed previously, the bulk recombination in the quasi-neutral base can be approximated by $U_{bulk} \approx n'/\tau_n$, where n' is the excess minority carrier concentration in the base, and τ_n is the electron

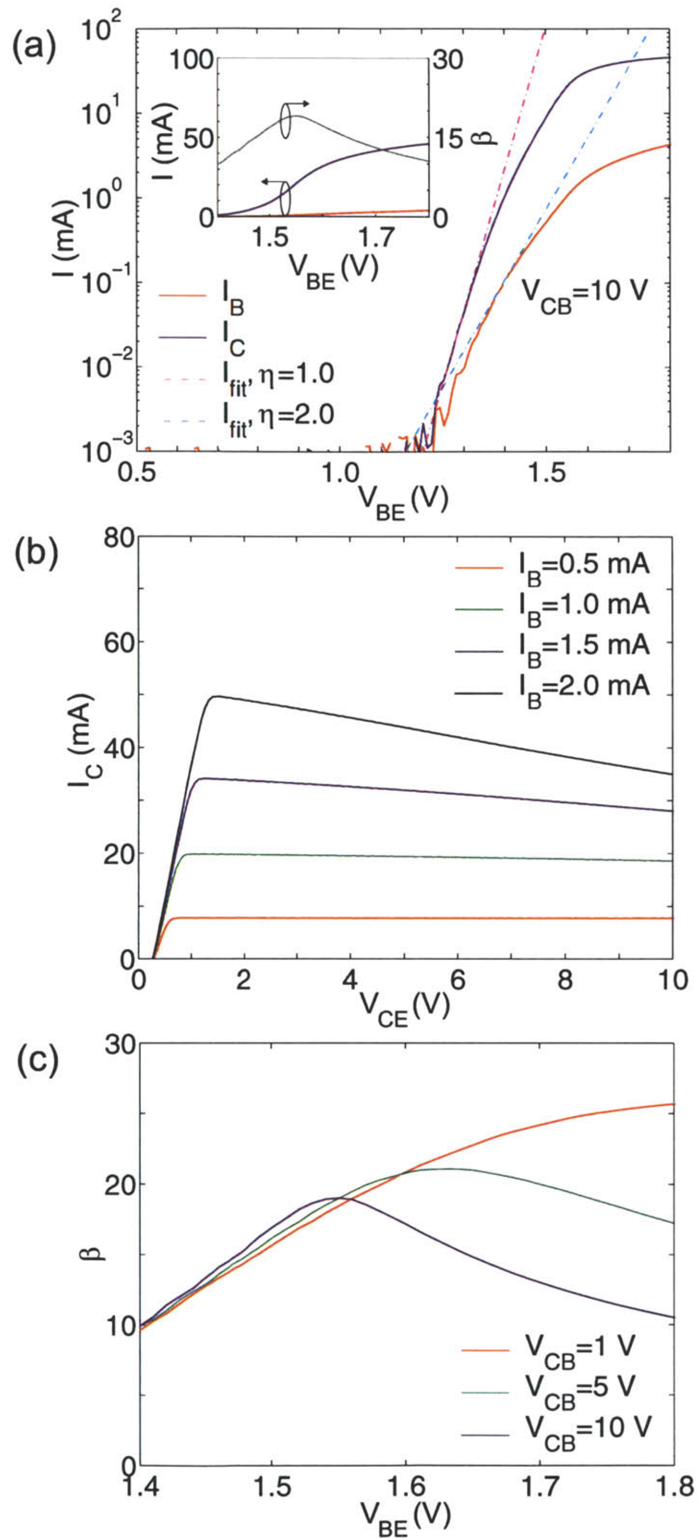

Figure 4-8: Measured DC characteristics of LG9000. In (a), I_C and I_B are plotted vs V_{BE} for a given V_{CB}. The dash-dotted lines originate from I_C and I_B curve fitting using suitable ideality factors. The inset illustrates I_C, I_B, and β vs V_{BE} in linear scale. In (b), I_C is plotted vs V_{CE} for a family of I_B values. In (c), β is plotted vs V_{BE} for a family of V_{CB} values.

recombination lifetime due to SRH, Auger, and radiative recombination. Therefore,

$$I_{p,bulk} = (qA_E/\tau_n) \int_0^{X_B} n' dz. \tag{4.3}$$

The base transit-time can be easily estimated as $\tau_B = Q_B/I_C$, where Q_B is the total charge of minority carriers in the base. Consequently,

$$\tau_B = (qA_E/I_C) \int_0^{X_B} n' dz. \tag{4.4}$$

Combining Eqs. 4.3-4.4, we arrive at the conclusion that $I_{p,bulk} = I_C\,(\tau_B/\tau_n)$ and $\beta = \tau_n/\tau_B$. Hence, $I_{p,bulk}$ scales with τ_B^{-1} for a given I_C, or equivalently β scales with τ_B^{-1}. One of the differences between LG7000U and LG7000, or between LG7000U and LG9000, is the reduction of base-transit time by the stepwise alloy grading. However, this is not reflected in the measurements of the DC current gain. The main reason is that the major component of I_B is $I_{p,scr}$, as we concluded from the value of η_B. $I_{p,scr}$ is practically unaffected by the introduction of base steps and overshadows the reduction of $I_{p,bulk}$. A similar trend has been observed between HBTs of uniform base and HBTs of linearly graded base where $I_{p,scr}$ is the dominant component of I_B [111].

From Figs. 4-7(b), 4-8(b), 4-9(b) we observe a significant reduction of $V_{CE,offset}$. Specifically, $V_{CE,offset} \approx 0.25$ V for both LG7000 and LG9000, and $V_{CE,offset} \approx 0.05$ V for LG7000U. For both LG7000 and LG9000, $\phi_{bi,BE} \approx 1.6$ V and $\phi_{bi,BC} \approx 1.37$ V. Therefore, $\phi_{bi,BE} - \phi_{bi,BC} \approx 0.23$ V, which is close to the measured $V_{CE,offset}$. For LG7000U, $\phi_{bi,BE} \approx 1.38$ V and $\phi_{bi,BC} \approx 1.37$ V. Hence, $\phi_{bi,BE} - \phi_{bi,BC} \approx 0.01$ V, which is close to the measured $V_{CE,offset}$. Similar to SM6000, the effect of self-heating is evident in both LG7000 and LG9000, as I_C decreases for increasing values of V_{CE}. However, the trend is different for LG7000U. We notice in 4-9(b) that I_C remains almost constant for a wide V_{CE}. We could conclude that self-heating is less important for LG7000U. The energy barrier in the valence band at the emitter-base interface is more effective in blocking the injection of holes because Δx_{EB}=0.30 for LG7000U, whereas Δx_{EB}=0.17 for LG7000 and LG9000. It is worth noticing in 4-9(b) that for high values of V_{CE}, I_C increases. This is the onset of avalanche breakdown [35]. The electrons are swept by the strong electric field in the depleted collector and acquire high kinetic energy. They collide with the lattice atoms and generate electron-hole pairs. This process continues in a chain-reaction fashion. From the direction of electrons and holes, it follows that I_C increases, I_B decreases, and the resultant β increases. This feature of avalanche breakdown does not manifest in LG7000 and LG9000. We could attribute this to higher self-heating. The electrons cannot gain enough kinetic energy for avalanche breakdown due to enhanced lattice scattering at elevated temperatures [112]. This is reflected in the avalanche multiplication factor M that decreases when the temperature increases.

The trends of the extracted β-V_{BE} plots for both LG7000 and LG9000 are similar to the ones discussed for SM6000. The distinct difference is that the values of β are much higher for LG7000

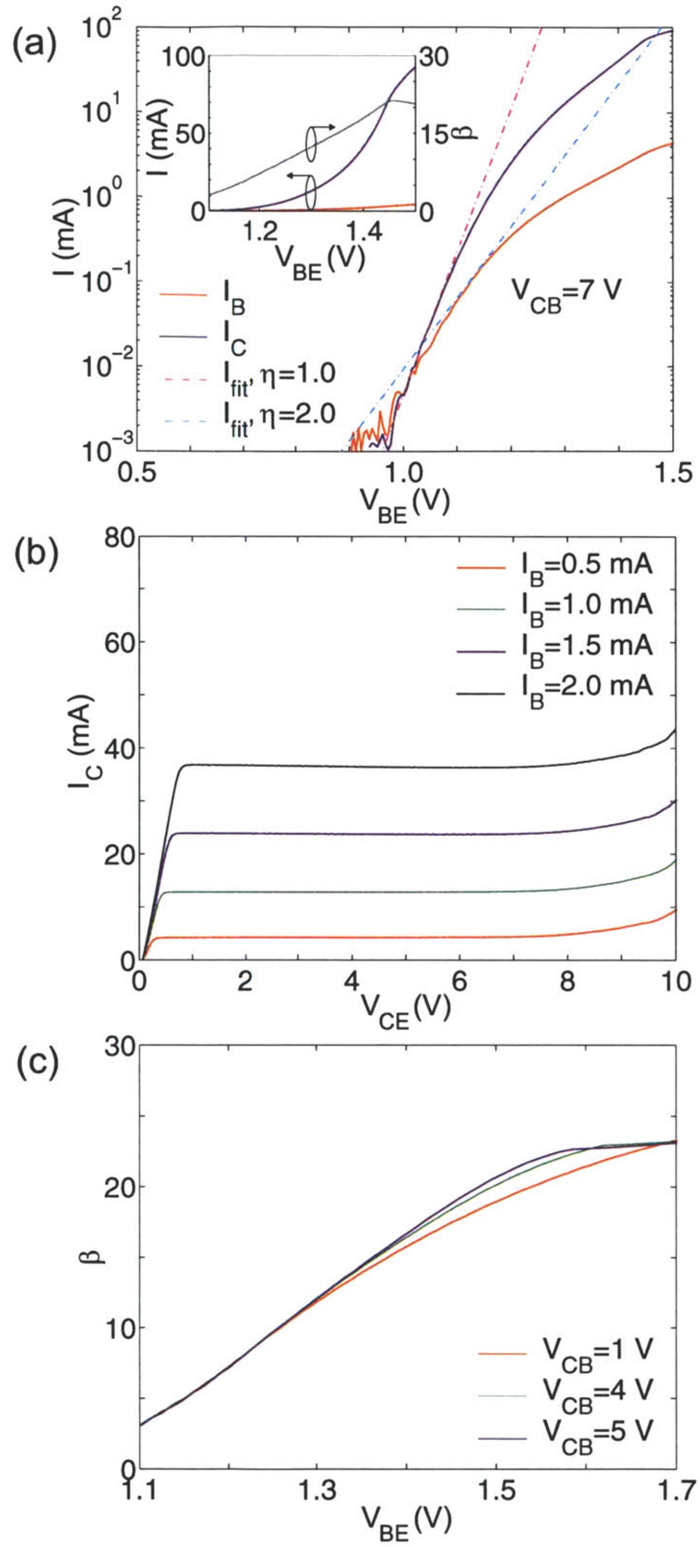

Figure 4-9: Measured DC characteristics of LG7000U. In (a), I_C and I_B are plotted vs V_{BE} for a given V_{CB}. The dash-dotted lines originate from I_C and I_B curve fitting using suitable ideality factors. The inset illustrates I_C, I_B, and β vs V_{BE} in linear scale. In (b), I_C is plotted vs V_{CE} for a family of I_B values. In (c), β is plotted vs V_{BE} for a family of V_{CB} values.

and LG9000. The characteristics of β-V_{BE} are different for LG7000U. As presented in Fig. 4-9(c), the changes of β with V_{CB} are slight and β saturates for high values of V_{BE}. This is an additional evidence of the fact that self-heating is less important for LG7000U.

4.3.3 DC Characteristics of SM7000 and SM9000

The DC features of LG7000 and LG9000 gave us a positive feedback about the quality of the MBE grown wafers and we proceeded towards the fabrication of SM7000 and SM9000. The yield of the fabrication process was not high and many of the device profiles illustrated in Fig. 4-4(b),(c),(d) were produced. Unfortunately, all the devices with the desired profile shown in Fig. 4-4(a) experienced an unexpected failure mode during the normal DC operation.

As we discussed earlier in 4.1, the high values of the specific contact resistance of the base contact consisting of Pt/Ti/Pt/Au, led us to the use of Pt/Zn/Au. This base contact was succesfully used in the fabrication of LG7000, LG9000, and LG7000U. The large HBTs with no self-alignment do not utilize micro-airbridges. The heat generated during the HBT operation is directed towards the subststrate. On the other hand, small self-aligned HBTs employ micro-airbridges. These are relatively small (2 μm $\times$ 6 μm) and their electric resistance is high. In addition, they are suspended and heat-conduction is carried out insufficiently by the surrounding air. The micro-airbridges of SM6000 were relatively robust in term of their mechanical and thermal properties. The only problem that we noticed was that high voltage biases for extended time can burn the base micro-airbridge. For SM7000 and SM9000, the mechanical strength of the base micro-airbridges was poor. Even a slow flow of N_2 could detach them, contary to the micro-airbridges of SM6000. More importantly, low DC biases proved to be catastrophic for the base micro-airbridges of both SM7000 and SM9000. This is reflected in the SEM pictures of Fig. 4-10. The base micro-airbridge, which is shown intact in Fig. 4-10(a) before the application of DC bias, became deformed and finally broke after the application of DC bias (Fig. 4-10(b)). We could provide an explanation based on the sequence of metal layers used for the base contact. The melting points of Pt, Ti, and Au are relatively high ($T_{\mathrm{melt,Pt}}$=1772 °C, $T_{\mathrm{melt,Ti}}$=1660 °C, $T_{\mathrm{melt,Au}}$=1664 °C) and the micro-airbridges of SM6000 are expected to withstand a moderate heat dissipation. On the other hand, the melting point of Zn is low ($T_{\mathrm{melt,Zn}}$=419 °C). In addition, Zn occupies a large part of the base metal thickness (about 1/3). As we mentioned in 4.1, the total thickness of the base metal was measured to be less than the targeted thickness (1000-1200 Å instead of 1500 Å), increasing the electric resistance and the heat dissipation accordingly. We noticed the physial property of low $T_{\mathrm{melt,Zn}}$ during the evaporation of the base contact. The generated electron beam requires 15-17 % of the maximum power of our metal evaporator to melt Ti, Pt, and Au. This is typical for most of the commonly used metals. On the contrary, only 11 % of the maximum power of the e-beam machine was needed to melt Zn. This caused a practical problem since at this low power level, Zn does not glow and the electron beam

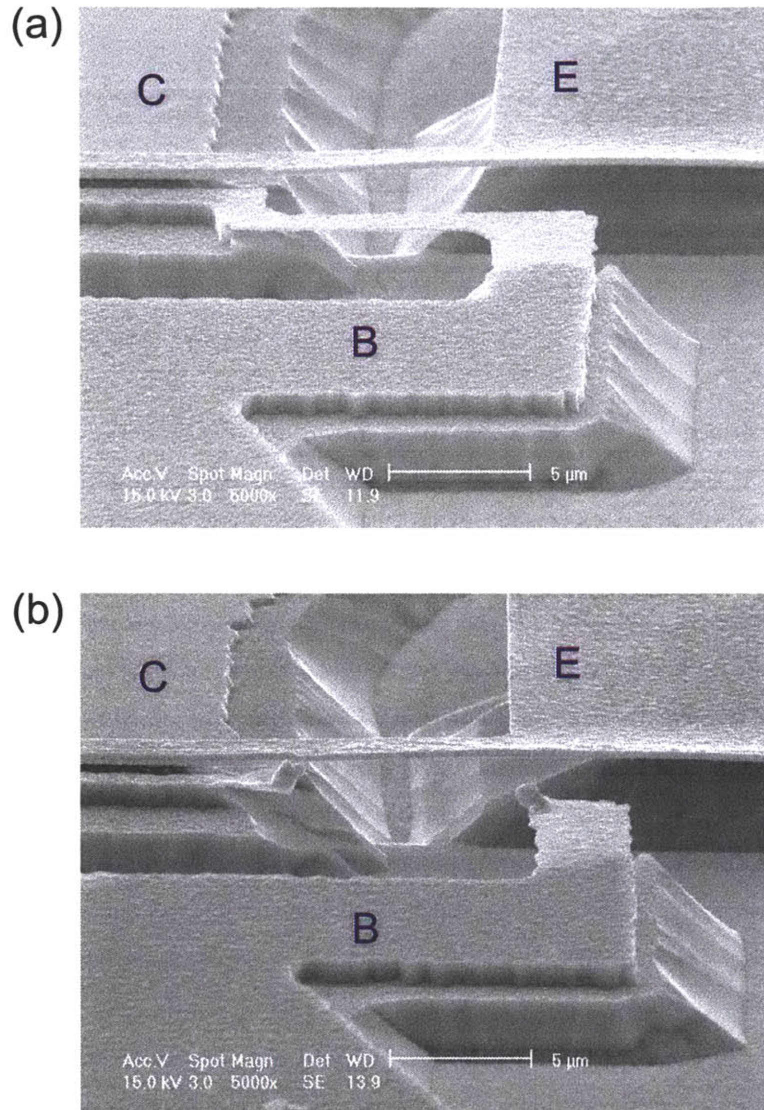

Figure 4-10: SEM pictures of the HBT focusing on the emitter and base micro-airbridges. In (a), no DC bias had been applied at the device terminals and the micro-airbridges remain intact. In (b), DC bias had been applied at the device terminals. The elevated temperature of the base micro-airbridge caused metal deformation and eventually, the base micro-airbridge broke.

cannot be easily centered on the crucible. We have to point out that the emitter micro-airbridges for all the self-aligned HBTs, SM6000, SM7000, and SM9000, had excellent mechanical and thermal properties. This can be attributed to the high melting point of Ti, Pt, and Au and to the thickness of the emitter contact metal (2300-2500 Å). Since the emitter metal is the top layer of the device, there is no restriction on the evaporated metal thickness.

We were able to take DC measurements of SM7000 and SM9000 in a low-bias range. After just one low-voltage sweep, the base micro-airbridge could not withstand the heat dissipation and finally broke. The DC characteristics of SM7000 and SM9000 are shown in Figs. 4-11,4-12. For the I_C-V_{BE} plots depicted in Figs. 4-11(a),4-12(a), we had to lower the applied V_{CB} so that we could at least sweep V_{BE} in a low range. Otherwise, the base micro-bridge would burn at even lower V_{BE}. Therefore, the collector is not fully depleted. The extracted ideality factors are $\eta_C \approx 1$ and $\eta_B \approx 1.8$ for a small V_{BE} range. These values were anticipated after the DC characterization of LG7000 and LG9000. For V_{CB}=4 V, β_{max}=3.7 for SM7000, and β_{max}=4.2 for SM9000. However, these are the values extracted for a low V_{BE} sweep while β_{max} was monotonically increasing. From the voltage range we were able to sweep, we could conclude that even if the micro-airbridge had been intact, the high values of β_{max} measured for LG7000 and LG9000 would not have been attained. The fact that $\eta_B < 2$ signifies that surface recombination becomes an important component. This is to be expected since a small HBT has a small emitter area that scales the space charge recombination but not the surface recombination which is proportional to the length of the device. The I_C-V_{CE} characteristics for a family of I_B values are shown in Figs. 4-11(b),4-12(b). The allowed values of I_B are very small. Similarly, the allowed range of V_{CE} is low. For such low current and voltage biases, the overall heat dissipation of the device is low and the negative slope of I_C for increasing V_{CE} does not emerge.

It is unfortunate that we cannot bias our devices safely at high V_{BE}. According to the simulations we carried out with our device solver, a current level in the range of 5-10 mA is required in order to detect a transit-time oscillation. Otherwise, the emergence of negative resistance is completely washed out by the device parasitics. Any further DC measurements could not be continued and the desired microwave/millimeter-wave characterization could not be conducted due to the requirement of higher bias point.

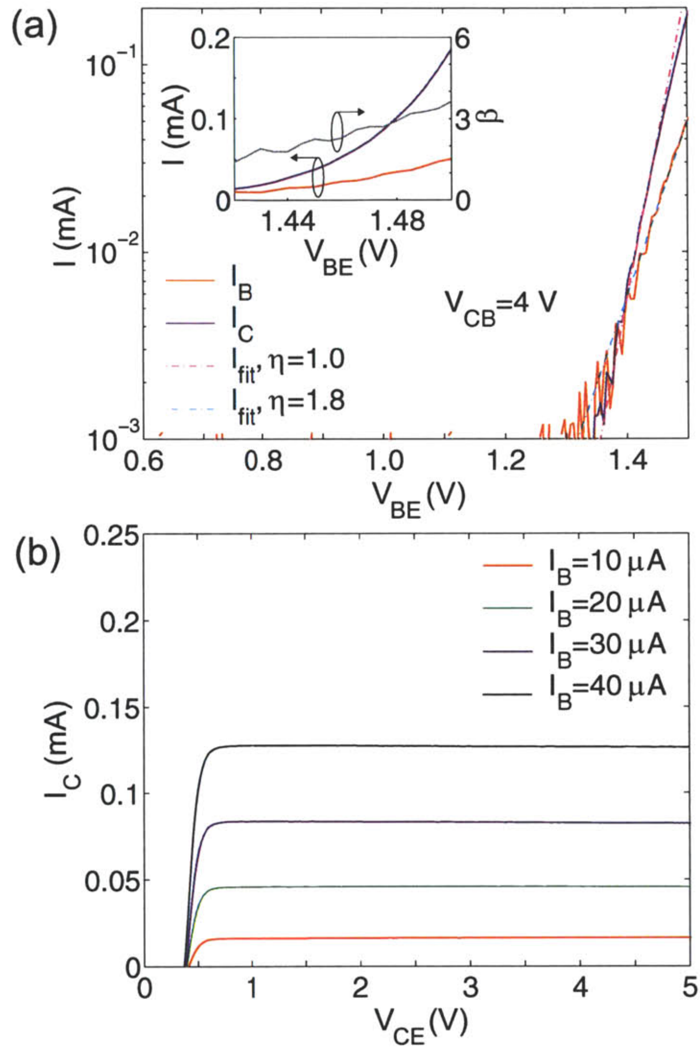

Figure 4-11: Measured DC characteristics of SM7000. In (a), I_C and I_B are plotted vs V_{BE} for a given V_{CB}. The dash-dotted lines originate from I_C and I_B curve fitting using suitable ideality factors. The inset illustrates I_C, I_B, and β vs V_{BE} in linear scale. In (b), I_C is plotted vs V_{CE} for a family of I_B values.

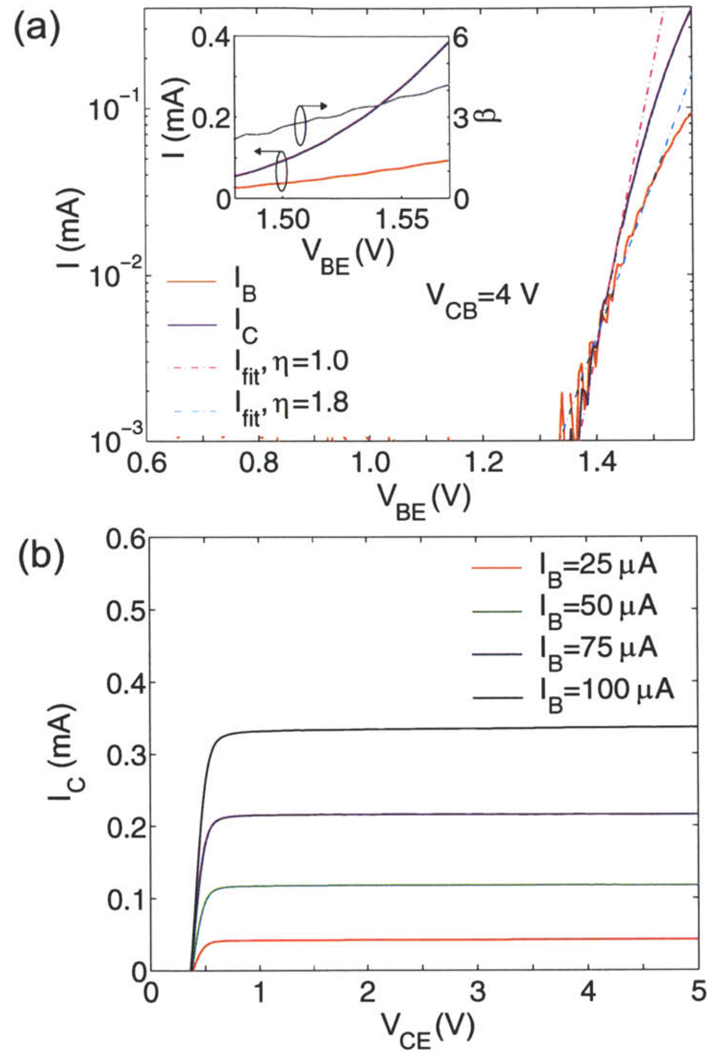

Figure 4-12: Measured DC characteristics of SM9000. In (a), I_C and I_B are plotted vs V_{BE} for a given V_{CB}. The dash-dotted lines originate from I_C and I_B curve fitting using suitable ideality factors. The inset illustrates I_C, I_B, and β vs V_{BE} in linear scale. In (b), I_C is plotted vs V_{CE} for a family of I_B values.

Chapter 5

Conlusions

This work was based on the ideas of Luryi *et al* in [24]. Our research explored various aspects of a novel HBT with stepwise alloy-graded base. We realized that the intuitive theoretical approach in [24] did not incorporate in detail the complexity of carrier transport and the performance of the device could not be predicted with a high degree of accuracy. We developed a device simulator that solved iteratively the Boltzmann transport equation in the base of the HBT for arbritrary frequencies. We considered the impurity and the LO phonon scattering as the dominant carrier scattering mechanisms. The intrinsic and extrinsic elements of the device were taken into account to implement a small-signal equivalent circuit. The S-parameters were extracted and the theoretical high-frequency performance of the HBT was evaluated.

We initially examined the HBT as an amplifier. The simulation results suggested that for a given base thickness X_B, the introduction of base steps enhances both the current gain and the unilateral power gain. In addition, for a given base step thickness X_{step}, the increase of the number of base steps resulted in a tradeoff between the unilateral power gain and the current gain. However, from both of these perpectives (constant X_B or constant X_{step}), the stepwise alloy-grading in the base did not offer a dramatic improvement in the microwave/millimeter-wave performance of the HBT. We noticed that the base transport factor α_T of the device experiences intermediate phase delay and magnitude attenuation. If this is combined with a large collector transit-time delay, the applied voltage and the output current can differ in phase by 180°. The output resistance of a common-emitter configuration becomes negative for a frequency band and a microwave/millimeter-wave oscillator can be implemented.

The emergence of negative resistance was the main motivation of this thesis and the HBT design reflected this goal. We designed a MBE growth sheet after we conducted a number of simulations using our developed solver. Various ohmic contacts were studied, fabricated, and tested to meet our design goals. We examined a number of self-aligned HBT layouts and our final set of masks reflects

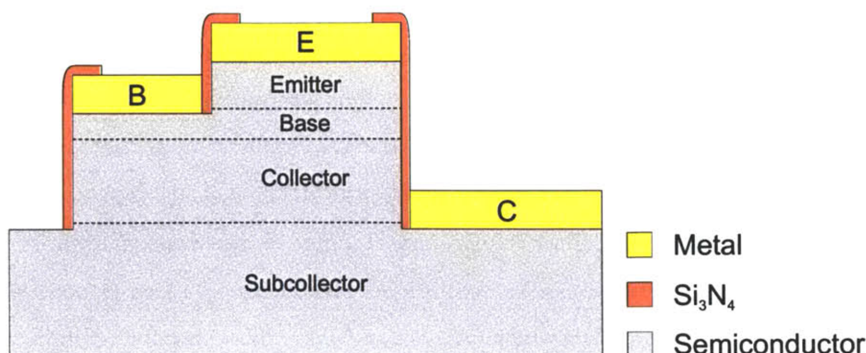

Figure 5-1: Profile of a HBT that allows the evaporation of a thick base ohmic contact. This is expected to increase the tolerance against self-heating without increasing the risk of an electric short between the emitter and the base. The emitter mesa is formed by dry etching and a Si_3N_4 layer is deposited on the mesa sidewalls.

a compromise between the ideal device geometry and the practical limitations of our clean room. The active device was incorporated in a properly designed coplanar waveguide in order to unveil the high-frequency operation with a network analyzer. We investigated a number of different device isolation schemes, and we decided to use micro-airbridges. This design choice affected significantly the layout, the sequence of fabrication steps, and the yield of our devices. The HBT fabrication we experimented on, was a try-and-error, laborious, and time consuming process.

We performed DC measurements for all fabricated HBTs. The first batch of self-aligned HBTs was characterized by unfavorably high ideality factors for the base and collector current, very low current gain, and high offset voltage. We attributed these unexpected results to the MBE growth and we selected slightly different MBE design parameters and MBE growth conditions. We initially fabricated large HBTs with no self-alignment. Significant improvements were detected for the base and collector ideality factors, the current gain, and the offset voltage. We proceeded with the fabrication of small self-aligned HBTs. As expected, the DC operation was noticeably improved. However, the devices suffered from the very short lifetime of the base micro-airbridges. The new MBE design called for alloyed base ohmic contacts that proved to be very sensitive to the device self-heating. The base micro-airbridges were deformed and broke at moderate current levels. Therefore, it was not possible to conduct high frequency measurements since we could not establish a high enough bias voltage V_{BE}. We had verified earlier the on-wafer calibration standards and measured the attenuation loss and the effective permittivity of the coplanar waveguide. Deviations from the ideal values were detected. These were attributed to the coplanar waveguide geometry and the doping profile of the MBE grown layers.

The high sensitivity of the base micro-airbridges to the device self-heating can be dealt with various approaches. One way is to improve the MBE growth conditions so that a high doping level

can be achieved in the base without compromising the crystal quality. Thus, a non-alloyed base ohmic contact could be used with better thermal and mechanical properties. A different approach involves modifications in the HBT fabrication process. This alternative results in high-yield devices. However, our current clean room limitations do not allow us to apply critical photolithographic steps. It is instructive though to gain a different perspective of the HBT fabrication process. As illustrated in Fig. 5-1, the emitter is formed completely by dry etching. A passivation layer is deposited on the sidewalls and a thick base metal can be evaporated without creating an electric short between the emitter and the base. The fine separation S_{BE} can be set by a stepper. Similar steps can be followed for the evaporation of the subcollector contact. A thick base ohmic contact is characterized by less heat dissipation and improved tolerance against self-heating. In addition, the Zn thickness can be probably decreased without sacrificing the quality of the base ohmic contact. Other alloyed ohmic contacts with better thermal properties can be tested. Zn can be substituted with Mn and the heat-tolerance is expected to improve ($T_{\mathrm{melt,Zn}}$=419 °C, $T_{\mathrm{melt,Mn}}$=1245 °C).

Unfortunately, high frequency measurements were not taken to prove our predictions for transit-time oscillations in the microwave/millimeter-wave regime. However, we built the foundation for a future success from a different worker. We developed the framework for the analysis, design, fabrication, and testing of our devices. Modifications in the fabrication process will lead to robust HBTs whose potential can be further explored.

Appendix A

Process Flow

A. Wafer Cleaving

1. Cleave the device wafer in 6 cm × 6 cm pieces.
2. Mark lightly the direction of the major flat on the back of the device pieces with the wafer scriber and indicate the wafer flat convention on the label of the piece carriers (US or EJ).

B. Cleaning

1. Blow N_2 to the pieces to remove the GaAs dust created during the device wafer cleaving.
2. Put the pieces in a polypropylene basket and dip it into (1) acetone (2 min), (2) methanol (2 min), and (3) isopropanol (2 min). Rinse in running DI water for 30 s. Blow dry the pieces with N_2.

C. Emitter Photolithography

1. Place the device pieces in clean aluminum weighing dishes. Put the aluminum dishes in the HMDS oven as soon as possible. Extended air exposure creates a thin layer of H_2O over the device surface that deteriorates photoresist adhesion. Leave the device pieces in the HMDS oven without running any HMDS recipe. The 150 °C temperature of the HMDS oven is ideal for drying the pieces well. After 10 min of drying, choose program 4 (30 s exposure to HMDS), and run the HMDS recipe.
2. Prepare the coater. Lay a piece of aluminum foil around the coater chuck to prevent an accidental drop of the piece in the photoresist drain. Activate only the spin cycle and set the time for 40 s and the speed for 4k rpm. Test the vacuum and the settings with a dummy piece. Pour 1 ml of the AZ 5206 photoresist in a small clean pyrex beaker. Remove the pieces from the HMDS oven. If the humidity in the clean room is unusually high, take out one piece at a time while leaving the rest in the HMDS oven. Place the device piece on the chuck, and activate the vacuum. Pour one drop of the photoresist on the piece using a

thin glass eyedropper. Immediately turn on the spin cycle to prevent the photoresist from going on the back side of the piece. At the end of the spin cycle, inspect whether there is any photoresist on the back side of the piece, and if so, remove it carefully with a fine wipe dipped in acetone. Dispose of the eyedropper.

3. Put the pieces in the aluminum dishes and place them in the prebake oven (90 °C, 30 min).
4. Put a thin neoprene film on the chuck of the mask aligner to minimize the effect of the mask aligner wedge error. The neoprene film has small holes that correspond to the vacuum holes of the chuck. Insert the mask in the mask holder and place the device piece on top of the neoprene film. Check the vacumm. Choose the settings: hard contact, exposure time 25 s, intensity 6 mW/cm^2. Check if Newton rings are formed during contact. Observe carefully the neoprene - device piece - mask profile while in contact. If the wedge error is still large, push lightly the side of the chuck that touches first the device piece while raising it for contact. Use the EMIT submask. Align the edge of the piece with the mask and expose the photoresist. Remove the mask from the mask aligner.
5. Put a Si wafer on top of the 120 °C hotplate. Bake the piece for 20 s on top of the Si wafer and carefully remove it from the hotplate. The Si wafer is helpful for fast and safe transfer as we slide the piece with a pair of tweezers.
6. Flood expose the piece for 120 s.
7. Put the device piece in a polypropylene basket and immerse it in (a) a beaker with AZ 422 MIF developer for 50-60 s, and in (b) a beaker with DI water. Blow dry the piece with N_2.
8. Inspect the photolithography under a microscope. If the photolithography is not satisfactory, follow the steps of process B and dip the pieces in the AZ 422 MIF developer for 1 min to remove any remaining HMDS. Rinse with DI water, blow dry with N_2, and repeat the steps of process C. Check if the relative humidity in the clean room is within the acceptable range 32-42 %.

D. Emitter Metal Evaporation and Liftoff

1. Clean the e-beam chamber and place the Ti, Pt, Au crucibles. Make sure the crucibles have a clean surface. If the surface is not clean, wipe it with a fab wipe and blow N_2 to the crucible.
2. Remove the native oxide layer of the pieces with a BOE dip for 15 s. Rinse the pieces with DI water and blow dry with N_2.
3. Place the pieces in the e-beam holder for small pieces as soon as possible in order to avoid a subsequent native oxide formation. Pump the e-beam chamber. Start depositing Ti (500 Å) / Pt (200 Å) / Au (2300 Å) at a 2 Å/s evaporation rate when the vacuum level is lower than 2×10^{-6} mTorr. For a lower vacuum level (2×10^{-7} mTorr), pump the e-beam chamber overnight.
4. Remove the pieces from the e-beam. Put the pieces in a shallow beaker with acetone. Agitate

gently. Liftoff with ultrasonic vibrations may result in peeling off large metal surfaces due to the weak metal adhesion on InGaAs. Check the total metal thickness with the profilometer.

5. If the liftoff is stubborn, the step prior to agitation in acetone should be the opening of holes in areas surrounding the device. This is a time consuming step but it guarantees easy liftoff. The holes can be made at a probe station using probes of about 50 μm diameter.

E. Device Protection from the Galvanic Effect and Emitter Wet Etching

Follow the general guidelines described in process C. In addition,

1. Use Shipley 1813 photoresist and choose the settings: 30 s time and 4k rpm speed for the spin cycle.
2. Prebake the pieces for 30 min in the 90 °C convection oven.
3. Expose the pieces for 140 s at hard contact. Use the PR1 submask.
4. Develop in MIF 319 for 30-40 s.
5. Postbake the pieces for 30 min in the 90 °C convection oven.
6. Prepare a 3 ml H_2SO_4 : 3 ml H_2O_2 : 450 ml H_2O solution. Dip the piece in the solution using a polypropylene basket. The etching rate is approximately 400 Å/min. Etch the InGaAs layers. Make sure the beaker containing the etching solution is leveled and the basket remains stationary during the etching. A slight movement can introduce surface roughness. Check the etched depth with a profilometer.
7. Prepare a 10 ml NH_4OH : 4 ml H_2O_2 : 500 ml H_2O solution. The etching rate is approximately 1500 Å/min. Etch the emitter and stop 300 Å before the emitter-base junction.
8. Remove the photoresist following the steps of process B. Dip the pieces in MIF 319 for 30 s to remove any remaining HMDS, and rinse with DI water.

F. Sidewall Deposition of Si_3N_4

1. Deposit isotropically 2000 Å of Si_3N_4. PECVD-ECR conditions: 10 sccm of N_2, 113 sccm of SiH_4, 60 mTorr pressure, 200 W ECR power, 80 °C chuck temperature. The deposition rate is approximately 350 Å/min.
2. Etch anisotropically the Si_3N_4. RIE-ECR conditions: 2 sccm O_2, 15 sccm CF_4, 15 sccm He, 20 mTorr pressure, 300 W ECR power, 15 W RF power, 20 °C chuck temperature. The etching rate is approximately 1000 Å/min. The Si_3N_4 remains around the metal undercut for emitter passivation. Inspect the metal layer under a microscope and compare the metal brightness with that of a piece with no Si_3N_4 to make sure that the dielectric has been completely etched.

G. Device Protection from the Galvanic Effect and Emitter Wet Etching

Follow the steps of process E. Etch 500 Å.

H. Base Photolithography

Follow the steps of process C. Use the BASE submask.

I. Base Metal Evaporation and Liftoff

Follow the steps of process D. Evaporate Pt (80 Å) / Zn (500 Å) / Au (1000 Å).

Use the rapid thermal annealer. Anneal at 360 °C for 40 s.

J. Dry Etching Towards the Subcollector

Etch anisotropically the base and the collector. RIE-ECR conditions: 10 sccm He, 15 sccm BCl_3, 5 mTorr pressure, 300 W ECR power, 15 W RF power, 20 °C chuck temperature. The etching rate is approximately 2000 Å/min.

K. Shallow Wet Etching of the Subcollector

Follow the steps of process E. Use the PR2 submask. The photoresist openings are defined in the subcollector area. Etch 4000 Å.

L. Subcollector Photolithography, Metal Evaporation, and Liftoff

Follow the steps of process C and process D. The only changes are the following:

1. Use the AZ 5214 photoresist. Expose for 20 s, use the COL submask, postbake the pieces on the 120° C hotplate for 1 min, flood expose for 240 s, and develop in AZ 422 MIF for 1 min 45 s.
2. Evaporate Ni (50 Å) / Au (100 Å) / Ge(500 Å) / Au(900 Å) / Ni(300 Å) / Au(1200 Å).
3. Use the rapid thermal annealer. Anneal at 380 °C for 30 s.

M. Active Device Isolation

1. Follow the steps of process E. Use the ISO submask. Prepare the solution 10 ml NH_4OH : 4 ml H_2O_2 : 500 ml H_2O. Etch about 2 μm.
2. Dip the device pieces in acetone, methanol, and isopropanol. Let the pieces air-dry. The use of N_2 blow can be catastrophic for the base micro-airbridges.

Bibliography

[1] M. J. W. Rodwell, M. Urteaga, T. Mathew, D. Scott, D. Mesa, Q. Lee, J. Guthrie, Y. Betser, S. C. Martin, R. P. Smith, S. Jaganathan, S. Krishnan, S. I. Long, R. Pullela, B. Agarwal, U. Bhattacharya, L. Samoska, and M. Dahlstrom. "Submicron Scaling of HBTs". *IEEE Trans. Electron Devices*, 48:2606–2624, 2001.

[2] K. Runge, P. J. Zampardi, R. L. Pierson, P. B. Thomas, S. M. Beccue, R. Yu, and K. C. Wang. "High Speed HBT Circuits for up to 40 Gb/s Optical Communication". In *GaAs IC Symp. Dig.*, pages 211–214. IEEE, 1997.

[3] G. Freeman, M. Meghelli, Y. Kwark, S. Zier, A. Rylyakov, M. A. Sorna, T. Tanji, O. M. Schreiber, K. Walter, J. S. Rieh, B. Jagannathan, A. Joseph, and S. Subbanna. "40-Gb/s Circuits Built from a 120-GHz f_T SiGe Technology". *IEEE J. Solid-State Circuits*, 37:1106–1114, 2002.

[4] K. Ishii, H. Nosaka, M. Ida, K. Kurishima, S. Yamahata, T. Enoki, T. Shibata, and E. Sano. "4-Bit Multiplexer/Demultiplexer Chip Set for 40-Gbit/s Optical Communication Systems". *IEEE Trans. Microwave Theory Tech.*, 51:2181–2187, 2003.

[5] W. Skones, P. Cheng, D. Ching, M. Inerfield, S. Nelson, and C. Wong. "High Dynamic Range InP HBT Delta-Sigma Analog-to-Digital Converters". In *GaAs IC Symp.*, pages 279–282. IEEE, 2002.

[6] J. F. Jensen, G. Raghavan, A. E. Cosand, and R. H. Walden. "A 3.2-GHz Second-Order Delta-Sigma Modulator Implemented in InP HBT Technology". *IEEE J. Solid-State Circuits*, 30:1119–1127, 1995.

[7] G. Van Andrews, J. B. Delaney, M. A. Vernon, M. P. Harris, C. T. M. Chang, T. C. Eiland, C. E. Hastings, V. L. Diperna, M. C. Brown, W. A. White, and L. J. Kushner. "Recent Progress in Wideband Monolithic Direct Digital Synthesizers". In *1996 Microwave Theory and Techniques Int. Microwave Symp. Dig.*, pages 1347–1350. IEEE, 1996.

[8] A. L. Gutierrez-Aitken, E. N. Kaneshiro, J. H. Matsui, D. J. Sawdai, J. K. Notthof, P. T. Chin, and A. K. Oki. "Cantilevered Base InP DHBT for High Speed Digital Applications". *Int. J. High-Speed Electron. Syst.*, 11:245–256, 2001.

[9] S. E. Rosenbaum, B. K. Kormanyos, L. M. Jelloian, M. Matloubian, A. S. Brown, L. E. Larson, L. D. Nguyen, M. A. Thompson, L. P. B. Katehi, and G. M. Rebeiz. "155- and 213-GHz AlInAs/GaInAs/InP HEMT MMIC Oscillators". *IEEE Trans. Microwave Theory Tech.*, 43:927–932, 1995.

[10] G. I. Ng and D. Pavlidis. "Low-Frequency Noise Characteristics of Latice-Matched (x=0.53) and Strained (x>0.53) $In_{0.52}Al_{0.48}As/In_xGa_{1-x}As$ HEMT's". *IEEE Trans. Electron Devices*, 39:523–532, 1992.

[11] D. Costa and J. S. Harris. "Low-Frequency Noise Properties of N-p-n AlGaAs/GaAs Heterojunction Bipolar Transistors". *IEEE Trans. Electron Devices*, 39:2389–2394, 1992.

[12] K. Uchida, H. Matsuura, T. Yakihara, S. Kobayashi, S. Oka, T. Fujita, and A. Miura. "A Series of InGaP/InGaAs HBT Oscillators up to D-Band". *IEEE Trans. Microwave Theory Tech.*, 49:858–865, 2001.

[13] Y. Baeyens, C. Dorschky, N. Weimann, Q. Lee, R. Kopf, G. Georgiou, J. P. Mattia, R. Hamm, and Y. K. Chen. "Compact InP-Based HBT VCOs with a Wide Tuning Range at W- and D-Band". *IEEE Trans. Microwave Theory Tech.*, 48:2403–2408, 2000.

[14] Y. Baeyens and Y. K. Chen. "A Monolithic Integrated 150 GHz SiGe HBT Push-Push VCO with Simultaneous Differential V-Band Output". In *2003 Microwave Theory and Techniques Int. Microwave Symp. Dig.*, pages 877–880. IEEE, 2003.

[15] K. W. Kobayashi, A. K. Oki, L. T. Tran, J. C. Cowles, A. Guitierrez-Aitken, F. Yamada, T. R. Block, and D. C. Streit. "A 108-GHz InP-HBT Monolithic Push-Push VCO with Low Phase Noise and Wide Tuning Bandwidth". *IEEE J. Solid-State Circuits*, 34:1225–1232, 1999.

[16] K. Uchida, H. Matsuura, T. Yakihara, S. Kobayashi, S. Oka, T. Fujita, and A. Miura. "A 100-GHz-Band Quadruple Power Combined Monolithic HBT Oscillator". *Electron. Comm. Jpn. 2*, 86:13–22, 2003.

[17] S. A. Maas, B. L. Nelson, and D. L. Tait. "Intermodulation in Heterojunction Bipolar Transistors". *IEEE Trans. Microwave Theory Tech.*, 40:442–448, 1992.

[18] A. Samelis and D. Pavlidis. "Mechanisms Determining Third Order Intermodulation Distortion in AlGaAs/GaAs Heterojunction Bipolar Transistors". *IEEE Trans. Microwave Theory Tech.*, 40:2374–2380, 1992.

[19] D. Pavlidis. "HBT vs PHEMT vs MESFET: What's Best and Why". In *Dig. of the Int. Conf. Compound Semiconduct. Manufact. Tech.* GaAs MANTECH, 1999.

[20] M. C. Ho, R. A. Johnson, W. J. Ho, M. F. Chang, and P. M. Asbeck. "High-Performance Low-Base-Collector Capacitance AlGaAs/GaAs Heterojunction Bipolar Transistors Fabricated by Deep Ion Implantation". *IEEE Electron Device Lett.*, 16:512–514, 1995.

[21] W. Liu, D. Hill, H. F. Chau, J. Sweder, T. Nagle, and J. Delaney. "Laterally Etched Undercut (LEU) Technique to Reduce Base-Collector Capacitances in Heterojunction Bipolar Transistors". In *GaAs IC Symp. Dig.*, pages 167–170. IEEE, 1995.

[22] D. M. Kim and S. H. Song. "Improved Collector Transit Time with Ballistic *pipi*-Structure in the Npn-AlGaAs/GaAs HBT". In *Proc. of the 1995 Bipolar/BiCMOS Circuits and Technology Meeting*, pages 39–42. IEEE, 1995.

[23] R. Katoh, M. Kurata, and J. Yoshida. "Self-Consistent Particle Simulation for AlGaAs/GaAs HBTs with Improved Base-Collector Structures". *IEEE Trans. Electron Devices*, 36:846–853, 1989.

[24] S. Luryi, A. A. Grinberg, and V. B. Gorfinkel. "Heterostructure Bipolar Transistor with Enhanced Forward Diffusion of Minority Carriers". *Appl. Phys. Lett.*, 63:1537–1539, 1993.

[25] G. I. Haddad and R. J. Trew. "Microwave Solid-State Active Devices". *IEEE Trans. Microwave Theory Tech.*, 50:760–779, 2002.

[26] H. Kroemer. "Heterostructure Bipolar Transistors and Integrated Circuits". *Proc. IEEE*, 70:13–25, 1982.

[27] A. A. Grinberg and S. Luryi. "Diffusion in a Short Base". *Solid-State Electron.*, 35:1299–1309, 1992.

[28] A. A. Grinberg and S. Luryi. "Ballistic Versus Diffusive Base Transport in the High-Frequency Characteristics of Bipolar Transistors". *Appl. Phys. Lett.*, 60:2770–2772, 1992.

[29] M. M. Dignam and A. A. Grinberg. "Solution of the Boltzmann Transport Equation in an Arbitrary One-Dimensional-Potential Profile". *Phys. Rev. B*, 50:4345–4354, 1994.

[30] A. R. St. Denis and D. L. Pulfrey. "Quasiballistic Transport in GaAs-Based Heterojunction and Homojunction Bipolar Transistors". *J. Appl. Phys.*, 84:4959–4965, 1998.

[31] M. Vaidyanathan and D. L. Pulfrey. "Effects of Quasi-Ballistic Base Transport on the High-Frequency Characteristics of Bipolar Transistors". *IEEE Trans. Electron Devices*, 44:618–626, 1997.

[32] K. Konistis and Q. Hu. "Numerical Study of a GaAs-Based Heterojunction Bipolar Transistor with Stepwise Alloy-Graded Base". *J. Appl. Phys.*, 91:5400–5410, 2002.

[33] S. Tiwari and S. L. Wright. "Material Properties of p-type GaAs at Large Dopings". *Appl. Phys. Lett.*, 56:563–565, 1990.

[34] S. Tiwari. *Compound Semiconductor Device Physics.* Wiley and Sons, New York, NY, 1998.

[35] W. Liu. *Handbook of III-V Heterojunction Bipolar Transistors.* Academic, San Diego, CA, 1992.

[36] A. A. Grinberg and S. Luryi. "Coherent Transistor". *IEEE Trans. Electron Devices*, 40:1512–1522, 1993.

[37] S. J. Mason. "Power Gain in Feedback Amplifier". *IRE Trans. Circuit Theory*, 1:20–25, 1954.

[38] S. Prasad, W. Lee, and C. G. Fonstad. "Unilateral Gain of Heterojunction Bipolar Transistors at Microwave Frequencies". *IEEE Trans. Electron Devices*, 35:2288–2294, 1988.

[39] J. R. Hayes, F. Capasso, R. J. Malik, A. C. Gossard, and W. Wiegmann. "Optimum Emitter Grading for Heterojunction Bipolar Transistors". *Appl. Phys. Lett.*, 43:949–951, 1983.

[40] S. Tiwari and D. J. Frank. "Barrier and Recombination Effects in the Base-Emitter Junction of Heterostructure Bipolar Transistors". *Appl. Phys. Lett.*, 52:993–995, 1988.

[41] T. Nozu, K. Tsuda, M. Asaka, and M. Obara. "Reliability Characteristics of Mesa-Etched Isolated Emitter Structure AlGaAs/GaAs HBTs with Be-Doped Base". In *GaAs IC Symp. Dig.*, pages 157–160. IEEE, 1992.

[42] N. Iizuka, K. Tsuda, T. Nozu, T. Sugiyama, Y. Kuriyama, and M. Obara. "Molecular Beam Epitaxy Growth for a Heavily-Doped Thin Base Layer of Heterojunction Bipolar Transistors Used for High-Speed Integrated Circuits". *J. Cryst. Growth*, 150:1297–1301, 1995.

[43] W. E. Hoke, P. J. Lemonias, D. G. Weir, S. K. Brierley, H. T. Hendriks, M. G. Adlerstein, and M. P. Zaitlin. "Molecular-Beam Epitaxial Growth of Heavily Acceptor Doped GaAs Layers for GaAlAs/GaAs Heterojunction Bipolar Transistors". *J. Vac. Sci. Technol. B*, 10:856–858, 1992.

[44] D. C. Streit, A. K. Oki, D. K. Umemoto, J. R. Velebir, K. S. Stolt, F. M. Yamada, Y. Saito, M. E. Fafizi, S. Bui, and L. T. Tran. "High-Reliability GaAs-AlGaAs HBTs by MBE with Be Base Doping and InGaAs Emitter Contacts". *IEEE Electron Device Lett.*, 12:471–473, 1991.

[45] H. Ito, T. Ishibashi, and T. Sugeta. "Extremely Low Resistance Ohmic Contacts to n-GaAs for AlGaAs/GaAs Heterojunction Bipolar Transistors". *Jpn. J. Appl. Phys.*, 23:L635–L637, 1984.

[46] F. Rana. Private Communication, 2002.

[47] M. P. Patkar, T. P. Chin, J. M. Woodall, M. S. Lundstrom, and M. R. Melloch. "Very Low Resistance Non-Alloyed Ohmic Contacts Using Low-Temperature Molecular Beam Epitaxy of GaAs". *Appl. Phys. Lett.*, 66:1412–1414, 1995.

[48] H. J. Ueng, V. R. Kolagunta, D. B. Janes, K. J. Webb, D. T. McInturf, and M. R. Melloch. "Annealing Stability and Device Application of Non-Alloyed Ohmic Contacts Using a Low Temperature Grown GaAs Cap on Thin n^+ GaAs Layers". *Appl. Phys. Lett.*, 71:2496–2498, 1997.

[49] D. B. Slater, P. M. Enquist, J. A. Hutchby, A. S. Morris, and R. J. Trew. "Low Emitter Resistance GaAs Based HBTs without InGaAs Caps". *IEEE Electron Device Lett.*, 15:154–156, 1994.

[50] S. L. Wright, R. F. Marks, S. Tiwari, T. N. Jackson, and H. Baratte. "In Situ Contacts to GaAs Based on InAs". *Appl. Phys. Lett.*, 49:1545–1547, 1986.

[51] T. Nittono, H. Ito, O. Nakajima, and T. Ishibashi. "Extremely Low Resistance Non-Alloyed Ohmic Contacts to n-GaAs Using Compositionally Graded $In_xGa_{1-x}As$ Layers". *Jpn. J. Appl. Phys.*, 25:L865–L867, 1986.

[52] T. Nittono, H. Ito, O. Nakajima, and T. Ishibashi. "Non-Alloyed Ohmic Contacts to n-GaAs Using Compositionally Graded $In_xGa_{1-x}As$ Layers". *Jpn. J. Appl. Phys.*, 27:1718–1722, 1988.

[53] K. Nagata, O. Nakajima, Y. Yamauchi, T. Nittono, H. Ito, and T. Ishibashi. "Self-Aligned AlGaAs/GaAs HBT with Low Emitter Resistance Utilizing InGaAs Cap Layer". *IEEE Trans. Electron Devices*, 35:2–7, 1988.

[54] http://www.ioffe.rssi.ru/SVA/NSM/Semicond/. Physical Properties of Semiconductors, Ioffe Physico-Technical Institute.

[55] S. H. Park, M. P. Park, T. W. Lee, K. M. Song, K. E. Pyun, and H. M. Park. "Comparison of AuGe/Ni/Au, AuGe/Pd/Au, Ti/Pt/Au, and WSi/Ti/Pt/Au Ohmic Contacts to n-type InGaAs". In *Proc. of the 1995 Int. Symp. Compound Semiconductors*, pages 295–300. Inst. Phys. Conf. Ser., Vol. 145, 1995.

[56] Y. T. Lyu, K. L. Jaw, C. T. Lee, C. D. Tsai, Y. J. Lin, and Y. T. Cherng. "Ohmic Performance Comparison for Ti/Ni/Au and Ti/Pt/Au on InGaAs/Graded InGaAs/GaAs Layers". *Mater. Chem. Phys.*, 63:122–126, 2000.

[57] T. Sugiyama, Y. Kuriyama, M. Asaka, N. Iizuka, T. Kobayashi, and M. Obara. "Ultra-Low Resistance Base Ohmic Contact with Pt/Ti/Pt/Au for High-f_{max} AlGaAs/GaAs Heterojunction Bipolar Transistors". *Jpn. J. Appl. Phys.*, 33:786–789, 1994.

[58] Y. Kuriyama, J. Akagi, T. Sugiyama, S. Hongo, K. Tsuda, N. Iizuka, and M. Obara. "DC to 40-GHz Broad-Band Amplifiers Using AlGaAs/GaAs HBTs". *IEEE J. Solid-State Circuits*, 30:1051–1054, 1995.

[59] T. Nogami and K. Morizuka. "Low-Resistive Ohmic Contact to *p*-type GaAs Using an Alloyed Pt/Zn/Au Layer". In *Proc. of the 1989 Int. Symp. GaAs and Related Compounds*, volume 29, pages 593–598. Inst. Phys. Conf. Ser. No 106, 1989.

[60] M. C. F. Chang, P. M. Asbeck, K. C. Wang, G. J. Sullivan, N. H. Sheng, J. A. Higgins, and D. L. Miller. "AlGaAs/GaAs Heterojunction Bipolar Transistors Fabricated Using a Self-Aligned Dual-Lift-Off Process". *IEEE Electron Device Lett.*, 8:303–305, 1987.

[61] K. Eda, M. Inada, Y. Ota, A. Nakagawa, T. Hirose, and M. Yanagihara. "Emitter-Base-Collector Self-Aligned Heterojunction Bipolar Transistors Using Wet Etching Process". *IEEE Electron Device Lett.*, 7:694–696, 1986.

[62] N. Hayama, A. Okamoto, M. Madihian, and K. Honjo. "Submicrometer Fully Self-Aligned AlGaAs/GaAs Heterojunction Bipolar Transistor". *IEEE Electron Device Lett.*, 8:246–248, 1987.

[63] K. Morizuka, M. Asaka, N. Iizuka, K. Tsuda, and M. Obara. "AlGaAs/GaAs HBTs Fabricated by a Self-Alignment Technology Using Polyimide for Electrode Separation". *IEEE Electron Device Lett.*, 9:598–600, 1988.

[64] K. Nagata, O. Nakajima, T. Nittono, Y. Yamauchi, and T. Ishibashi. "A New Self-Alignment Technology Using Bridged Base Electrode for Small-Scaled AlGaAs/GaAs HBTs". *IEEE Trans. Electron Devices*, 39:1786–1792, 1992.

[65] M. Inada, Y. Ota, A. Nakagawa, M. Yanagihara, T. Hirose, and K. Eda. "AlGaAs/GaAs Heterojunction Bipolar Transistors with Small Size Fabricated by a Multiple Self-Alignment Process Using One Mask". *IEEE Trans. Electron Devices*, 34:2405–2411, 1987.

[66] T. C. Edwards and M. B. Steer. *Foundations of Interconnect and Microstrip Design.* John Wiley and Sons, New York, NY, 2000.

[67] B. C. Wadell. *Transmission Line Design Handbook.* Artech House, Boston, MA, 1991.

[68] M. Riaziat, I. J. Feng, R. Majidi-Ahy, and B. A. Auld. "Single-Mode Operation of Coplanar Waveguides". *Electron. Lett.*, 23:1281–1283, 1987.

[69] M. Riaziat, R. Majidi-Ahy, and I. J. Feng. "Propagation Modes and Dispersion Characteristics of Coplanar Waveguides". *IEEE Trans. Microwave Theory Tech.*, 38:245–251, 1990.

[70] *Applying Error Correction Network Analyzer Measurements.* Application Note AN 1287-3, Agilent Technologies, 2002.

[71] G. F. Engen and C. A. Hoer. "Thru-Reflect-Line: An Improved Technique for Calibrating the Dual Six-Port Automatic Network Analyzer". *IEEE Trans. Microwave Theory Tech.*, 27:987–993, 1979.

[72] R. A. Soares, P. Gouzien, P. Legaud, and G. Follot. "Unified Mathematical Approach to Two-Port Calibration Techniques and Some Applications". *IEEE Trans. Microwave Theory Tech.*, 37:1669–1674, 1989.

[73] *Agilent Network Analysis Applying the 8510 TRL Calibration for Non-Coaxial Measurements.* Product Note 8510-8A, Agilent Technologies, 2000.

[74] R. B. Marks. "A Multiline Method of Network Analyzer Calibration". *IEEE Trans. Microwave Theory Tech.*, 39:1205–1215, 1991.

[75] TX-Line. Transmission line calculator, Applied Wave Research, 2003.

[76] S. Tadayon, G. Metze, A. Cornfeld, K. Pande, H. Huang, and B. Tadayon. "Application of Micro-Airbridge Isolation in High Speed HBT Fabrication". *Electron. Lett.*, 29:26–27, 1993.

[77] S. J. Pearton, F. Ren, J. R. Lothian, T. R. Fullowan, A. Katz, and P. W. Wisk. "Use of MeV O^+ Ion Implantation for Isolation of GaAs/AlGaAs Heterojunction Bipolar Transistors". *J. Appl. Phys.*, 71:4949–4854, 1992.

[78] S. J. Pearton. "Ion Implantation in III-V Semiconductor Technology". *Int. J. Mod. Phys. B*, 7:4687–4761, 1993.

[79] R. S. Virk, M. Y. Chen, C. Nguyen, T. Liu, M. Matloubian, and D. B. Rensch. "High-Performance AlInAs/InGaAs/InP DHBT K-Band Power Cell". *IEEE Microwave Guided Wave Lett.*, 7:323–325, 1997.

[80] U. Auer, S. O. Kim, P. Velling, W. Prost, and F. J. Tegude. "Fast Fabrication of InP-Based HBT Using a Novel Coplanar Design". *Electron. Lett.*, 34:1885–1886, 1998.

[81] S. O. Kim, P. Velling, U. Auer, M. Agethen, W. Prost, and F. J. Tegude. "High f_T, High Current Gain InP/InGaAs: C HBT Grown by LP-MOVPE with Non-Gaseous Sources". In *Proc. of the 2000 Int. Conf. on InP and Related Materials*, pages 470–472. IEEE, 2000.

[82] B. P. Yan, H. Wang, Y. Pan, and G. I. Ng. "Influence of Different Isolation Processes on the Performance of AlGaAs/GaAs Heterojunction Bipolar Transistors for Power Applications". *Solid-State Electron.*, 44:1989–1995, 2000.

[83] M. W. Dvorak, N. Matine, C. R. Bolognesi, X. G. Xu, and S. P. Watkins. "Design and Performance of InP/GaAsSb/InP Double Heterojunction Bipolar Transistors". *J. Vac. Sci. Technol. A*, 18:761–764, 2000.

[84] J. R. LaRoche, F. Ren, J. R. Lothian, J. Hong S. J. Pearton, and E. Lambers. "Use of Amorphous SiO and SiO_2 to Passivate AuGe-Based Contact for GaAs Integrated Circuits". *Electrochem. Solid. St.*, 395:395–397, 1999.

[85] D. Xu, T. Enoki, and Y. Ishii. "Impact of Recess-Etching-Assisting Resist-Openings on the Shapes of Gate Grooves for Short Gate Length InAlAs/InGaAs Heterojunction FETs". *IEEE Trans. Electron Devices*, pages 833–839, 1999.

[86] Y. Zhao, Y. Tkachenko, and D. Bartle. "Suppression of Electrochemical Etching Effects in GaAs PHEMTs". In *GaAs IC Symp. Dig.*, pages 163–166. IEEE, 1999.

[87] G. M. Metze, S. McPhilmy, and P. Laux. "Effects of Electrochemically-Induced Etching Non-Uniformities on Microwave Field Effect Transistors". *IEEE Electron Device Lett.*, 16:23–25, 1995.

[88] I. Hallakoun, T. Boterashvili, G. Bunin, and Y. Shapira. "Electrochemical Etching Impact on GaAs Process, Mask Design and Device Performance". In *Dig. of the Int. Conf. Compound Semiconduct. Manufact. Tech.*, pages 25–27. GaAs MANTECH, 2000.

[89] M. J. Howes and D. V. Morgan. *Gallium Arsenide: Materials, Devices, and Circuits*, chapter 4, pages 119–160. John Wiley and Sons, New York, NY, 1985.

[90] D. W. Shaw. "Localized GaAs Etching with Acidic Hydrogen Peroxide Solutions". *J. Electrochem. Soc.*, 128:874–880, 1981.

[91] Y. Mori and N. Watanabe. "New Etching Solution System, H_3PO_4-H_2O_2-H_2O, for GaAs and its Kinetics ". *J. Electrochem. Soc.*, 125:1510–1514, 1978.

[92] R. J. Roedel, W. West, T. S. Lee, D. Davito, and R. Adams. "Fabrication of $Ga_{1-x}Al_xAs$-GaAs Heterojunction Bipolar Transistors for Rapid Material Analysis ". *IEEE Trans. Semiconduct. Manufact.*, 8:79–83, 1995.

[93] S. M. Sze. *High-Speed Semiconductor Devices*, chapter 4. John Wiley and Sons, New York, NY, 1990.

[94] F. Ren, T. R. Fullowan, S. J. Pearton, J. R. Lothian, R. Esagui, and C. R. Abernathy. "Damage Introduction in GaAs/AlGaAs and InGaAs/InP Heterojunction Bipolar Transistor Structures during Electron Cyclotron Resonance Plasma Processing". *J. Vac. Sci. Technol. A*, 11:1768–1771, 1993.

[95] B. Luo, K. Ip, F. Ren, K. P. Lee, C. R. Abernathy, S. J. Pearton, and K. D. Mackenzie. "Hydrogenation Effects on AlGaAs/GaAs Heterojunction Bipolar Transistors". *Solid-State Electron.*, 45:1733–1741, 2001.

[96] J. W. Lee, K. D. Mackenzie, D. Johnson, R. J. Shul, S. J. Pearton, C. R. Abernathy, and F. Ren. "Device Degradation during Low Temperature ECR-CVD. Part II: GaAs/AlGaAs HBTs". *Solid-State Electron.*, 42:1021–1025, 1998.

[97] S. J. Pearton, U. K. Chakrabarti, A. P. Perley, W. S. Hobson, and M. Geva. "Dry Etching of GaAs, AlGaAs, and GaSb Using Electron Cyclotron Resonance and Radio Frequency $CH_4/H_2/Ar$ or $C_2H_6/H_2/Ar$ Discharges". *J. Electrochem. Soc.*, 138:1432–1439, 1991.

[98] J. G. Van Hassel, C. M. Van Es, P. A. M. Nouwens, J. H. Maahury, and L. M. F. Haufmann. "$CH_4/H_2/Ar$ Electron Resonance Plasma Etching for GaAs-Based Field Effect Transistors". *J. Electrochem. Soc.*, 142:2849–2852, 1995.

[99] S. W. Pang and K. K. Ko. "Comparison between Etching in Cl_2 and BCl_3 for Compound Semiconductors using a Multipolar Electron Cyclotron Resonance Source". *J. Vac. Sci. Technol. B*, 10:2703–2707, 1992.

[100] G. Franz. "Robust Reactive Ion Etching Processes for GaAs/AlGaAs/AlAs by Application of Statistical Concepts". *J. Electrochem. Soc.*, 140:1147–1151, 1993.

[101] J. W. Lee, J. Hong, E. S. Lambers, C. R. Abernathy, S. J. Pearton, W. S. Hobson, and F. Ren. "Plasma Etching of III-V Semiconductors in BCl_3 Chemistries. I. GaAs and Related Compounds". *Plasma Chem. Plasma P.*, 17:155–167, 1997.

[102] E. Aperathitis, D. Cengher, M. Kayambaki, M. Androulidaki, G. Deligeorgis, K. Tsagaraki, Z. Hatzopoulos, and A. Georgakilas. "Evaluation of Reactive Ion Etching Processes for Fabrication of Integrated GaAs/AlGaAs Optoelectronic Devices". *Mater. Sci. Eng. B-Solid*, 80:77–80, 2001.

[103] G. K. Reeves and H. B. Harrison. "Obtaining the Specific Contact Resistance from Transmission Line Model Measurements". *IEEE Electron Device Lett.*, 25:111–113, 1982.

[104] P. Rabinzohn, M. Kobayashi, S. Goto, M. Kawata, and T. Usagawa. "On the Determination of the Specific Contact Resistance of Alloyed Contacts to n-GaAs". *Jpn. J. Appl. Phys.*, 29:1896–1899, 1990.

[105] G. S. Marlow and M. B. Das. "The Effects of Contact Size and Non-Zero Metal Resistance on the Determination of Specific Contact Resistance". *Solid-State Electron.*, 3:91–94, 1982.

[106] H. Okada, S. Shikata, and H. Hayashi. "Electrical Characteristics and Reliability of Pt/Ti/Pt/Au Ohmic Contacts to *p*-type GaAs". *Jpn. J. Appl. Phys.*, 30:558–560, 1991.

[107] S. Tiwari and D. J. Frank. "Analysis of the Operation of GaAlAs/GaAs HBTs". *IEEE Trans. Electron Devices*, 36:2105–2121, 1989.

[108] S. Tiwari, D. J. Frank, and S. L. Wright. "Surface Recombination in GaAlAs/GaAs Heterostructure Bipolar Transistors". *J. Appl. Phys.*, 64:5009–5012, 1988.

[109] K. Yamanaka, S. Naritsuka, K. Kanamoto, M. Mihara, and M. Ishii. "Electron Traps in AlGaAs Grown by Molecular-Beam Epitaxy". *J. Appl. Phys.*, 61:5062–5069, 1987.

[110] S. C. M. Ho and D. L. Pulfrey. "The Effect of Base Grading on the Gain and High-Frequency Performance of AlGaAs/GaAs Heterojunction Bipolar Transistors". *IEEE Trans. Electron Devices*, 36:2173–2182, 1989.

[111] W. Liu. "Ideality Factor of Extrinsic Base Surface Recombination Current in AlGaAs/GaAs Heterojunction Bipolar Transistors". *Electr. Lett.*, 28:379–380, 1992.

[112] J. J. Liou, A. Ortiz-Conde, L. L. Liou, and C. I. Huang. "Thermal-Avalanche Interacting Behaviour of AlGaAs/GaAs Multi-Emitter Finger Heterojunction Bipolar Transistors". *Solid-State Electron.*, 38:1645–1648, 1995.

2545 · 39